COMPUTATIONAL EVALUATION OF FLOW AND HEAT TRANSFER IN THE SLIP FLOW REGIME

by

Jennifer A. van Rij

A dissertation submitted to the faculty of
The University of Utah
in partial fulfillment of the requirements for the degree of

Doctor of Philosophy

Department of Mechanical Engineering

The University of Utah

May 2009

ABSTRACT

Microfluidics is a rapidly emerging field with numerous applications. However, microscale flow and heat transfer characteristics are often not well understood, reliable microfluidic design data are limited, and the parameters and computational methods used to model microsystems are not well established. Utilizing MPM-ICE, an existing, continuum based, fluid-structure-interaction (FSI) algorithm, several studies are conducted to address some of these issues.

MPM-ICE is modified to include a number of common microfluidic effects, namely, first- and second-order accurate slip velocity, temperature jump, and creep flow boundary conditions, and viscous dissipation terms. For single fluid internal flow problems, slip velocity and temperature jump boundary conditions are applied at the computational boundaries of ICE. With this approach, rectangular microchannel Poiseuille and Nusselt numbers, with either isoflux or isothermal boundary conditions, are evaluated subject to the effects of channel aspect ratio, various slip boundary condition models, creep flow, viscous dissipation, pressure and shear work, axial conduction, and thermally/ hydrodynamically developing flow. The numerical modifications for internal flow are verified with comparisons to original analytic solutions for the Poiseuille and Nusselt numbers. For FSI problems, the momentum and thermal energy exchange models utilized by MPM-ICE are modified, such that slip velocity and temperature jump are achieved at deformable fluid-solid surfaces. The modified FSI models are verified with comparisons to original analytic solutions for the material displacements and temperature distributions.

The rectangular microchannel Poiseuille and Nusselt numbers are found to be significantly affected (up to an order of magnitude) by channel aspect ratio, rarefaction, slip model parameters, creep flow, viscous dissipation, pressure and shear work, axial conduction, and thermally/hydrodynamically developing flow. The single fluid internal flow evaluations indicate that ICE, run implicitly, with slip boundary conditions, is capable of accurately and efficiently assessing microscale effects, but for limited geometries. Slip flow FSI verifications indicate that MPM-ICE, with the modified momentum and energy exchange models, is the first FSI algorithm capable of modeling steady and unsteady FSI within the slip flow regime with accuracy approximately equivalent to the first-order slip velocity and temperature jump boundary conditions. MPM-ICE is, however, explicit with time and consequently requires significant computational resources.

TABLE OF CONTENTS

Chapter

LIST OF TABLES

Table Page

LIST OF FIGURES

ACKNOWLEDGMENTS

Partial support of this work by National Science Foundation grant number DGE9987616, of the Integrative Graduate Education and Research Traineeship Program, and US Department of Energy grant number W-7405-ENG-48, through the Center for the Simulation of Accidental Fires and Explosions, is gratefully acknowledged.

Chapter 3 was published in International Journal of Thermal Sciences, 46, J. van Rij, T. Harman, T. Ameel, The effect of creep flow on two-dimensional isoflux microchannels, 1095-1105, Copyright Elsevier (2007).

Chapter 4 was published in International Journal of Thermal Sciences, 48, J. van Rij, T. Ameel, T. Harman, The effect of viscous dissipation and rarefaction on rectangular microchannel convective heat transfer, 271-281, Copyright Elsevier (2009).

Chapter 5 was reprinted from International Journal of Heat and Mass Transfer, 52, J. van Rij, T. Ameel, T. Harman, An evaluation of secondary effects on microchannel frictional and convective heat transfer characteristics, 2792-2801, Copyright Elsevier (2009).

CHAPTER 1

INTRODUCTION

Advances in microfabrication techniques have made micro-electro-mechanical systems (MEMS) a reality [1-4]. However, before the full potential of these systems may be realized for applications in electronics, instrumentation, bioengineering, and advance energy systems, their behaviors must be completely understood, and the ability to reliably model them must exist. Currently, the ability to accurately and reliably predict the flow and heat transfer characteristics of microfluidic systems is a great challenge. Experimentally, microfluidic systems are difficult to study due to measurement and accuracy limitations. Analytical studies are limited to very simple configurations and necessitate many simplifying assumptions. For these reasons, accurate numerical solutions and methods are particularly important in the process of understanding and designing microfluidic systems. This research is intended to numerically substantiate and add to previous analytical, experimental, and numerical results and methods for predicting the flow and heat transfer characteristics of a few common microfluidic configurations.

1.1. Rarefaction effects

Several factors cause microscale fluid systems to behave differently than standard macroscale fluid systems. For microsystems with gaseous flows, rarefaction effects may be considerable. Rarefaction takes place as either the size or pressure of a fluid system decreases, resulting in a mean free path of the fluid molecules that is comparable to the characteristic length of the system itself. When this occurs, discontinuities between the fluid and the solid surface, as well as other noncontinuum behaviors begin to develop. Typically, the Knudsen number, Kn, is used to represent the degree of rarefaction, or noncontinuum effects present. The Knudsen number is defined as the ratio of the fluid's molecular mean free path to the characteristic length of the flow. Empirically, the Knudsen number has been used to classify flows into four different regimes [1]. While in the continuum flow regime ($Kn \leq 0.01$), conventional continuum conservation of momentum and energy methods, such as the Navier-Stokes equations, may be used. For the free molecular flow regime ($Kn \geq 10$), free molecular models such as the Boltzmann equation must be solved. In the transition flow regime ($0.1 \leq Kn \leq 10$), either numerical solutions of the Boltzmann equation or direct-simulation-Monte-Carlo (DSMC) methods are commonly used. For the slip flow regime ($0.01 \leq Kn \leq 0.1$), it has been determined experimentally [5-16] that the deviation of molecular motion from the continuum distribution is small enough that models based on the continuum equations may be used, but with 'slip velocity' and 'temperature jump' boundary conditions that take into account the incomplete momentum and energy exchange between the fluid molecules and the solid surface.

The original slip velocity boundary condition, given in Eq. (1.1), and temperature jump boundary condition, given in Eq. (1.2), were derived by Maxwell [16] and Smoluchowski [17], respectively.

$$u\big|_{y=0} - u_w = \left[\left(\frac{2-\sigma_v}{\sigma_v}\right)\frac{\lambda}{\mu}\tau + \frac{3}{4}\frac{\mu R}{P}\frac{\partial T}{\partial x}\right]_{y=0} \tag{1.1}$$

$$T\big|_{y=0} - T_w = \left[\left(\frac{2-\sigma_t}{\sigma_t}\right)\left(\frac{2\gamma}{1+\gamma}\right)\frac{\lambda}{Pr}\frac{\partial T}{\partial y}\right]_{y=0} \tag{1.2}$$

Equations (1.1) and (1.2), as well as subsequent equations, are presented in a format assuming a Cartesian coordinate system, a wall normal direction (y), and a streamwise direction (x). The first term in Eq. (1.1) is the slip velocity due to the shear stress at the wall, and the second term is the thermal creep velocity, u_c, due to a temperature gradient tangential to the wall. Values for the momentum accommodation coefficient, σ_v, and the thermal accommodation coefficient, σ_t, range from zero to one, where $\sigma_v = 0$ represents completely specular reflection, $\sigma_v = 1$ represents completely diffuse reflection, and $\sigma_t = 1$ corresponds to a perfect energy exchange.

Equations (1.1) and (1.2) are a result of a first-order expansion, in Kn, of the Boltzmann equation, and understood to be applicable only in the slip flow regime [18]. However, in an effort to extend the range of applicability of the slip flow boundary conditions to higher Knudsen number flows, specifically the transition regime, many 'second-order' modifications and methods have been proposed [1, 19-34]. The boundary conditions derived by Deissler [20], given in Eqs. (1.3) and (1.4), and the boundary conditions suggested by Karniadakis and Beskok [1], given in Eqs. (1.5) and (1.6), are two of the more commonly applied second-order slip boundary condition models. Often, second-order boundary conditions models are compared for two-dimensional, planar, constant property flow. For this configuration, each of the slip boundary condition models presented in Eqs. (1.1) - (1.6) may be written in the format shown in Eqs. (1.7) and (1.8), where β_{v1} and β_{t1}, as defined in the Nomenclature, are the same for each model, and β_{v2} and β_{t2}, as given in Table 1.1, differ depending on the model.

$$u\big|_{y=0} - u_w = \left[\left(\frac{2-\sigma_v}{\sigma_v}\right)\lambda\frac{\partial u}{\partial y} - \frac{9}{16}\lambda^2\left(2\frac{\partial^2 u}{\partial y^2} + \frac{\partial^2 u}{\partial x^2} + \frac{\partial^2 u}{\partial z^2}\right)\right]_{y=0} \tag{1.3}$$

$$T\big|_{y=0} - T_w = \left[\left(\frac{2-\sigma_t}{\sigma_t}\right)\left(\frac{2\gamma}{1+\gamma}\right)\frac{\lambda}{Pr}\frac{\partial T}{\partial y} - \frac{9\lambda^2}{256}\left(\frac{177\gamma-145}{\gamma+1}\right)\left(2\frac{\partial^2 T}{\partial y^2} + \frac{\partial^2 T}{\partial x^2} + \frac{\partial^2 T}{\partial z^2}\right)\right]_{y=0} \tag{1.4}$$

$$u\big|_{y=0} - u_w = \left(\frac{2-\sigma_v}{\sigma_v}\right)\left[\lambda\frac{\partial u}{\partial y} + \frac{\lambda^2}{2}\frac{\partial^2 u}{\partial y^2}\right]_{y=0} \tag{1.5}$$

$$T\big|_{y=0} - T_w = \left(\frac{2-\sigma_t}{\sigma_t}\right)\left(\frac{2\gamma}{1+\gamma}\right)\frac{1}{Pr}\left[\lambda\frac{\partial T}{\partial y} + \frac{\lambda^2}{2}\frac{\partial^2 T}{\partial y^2}\right]_{y=0} \tag{1.6}$$

$$u\big|_{y=0} - u_w = \left[\beta_{v1}\lambda\frac{\partial u}{\partial y} - \beta_{v2}\lambda^2\frac{\partial^2 u}{\partial y^2}\right]_{y=0} \tag{1.7}$$

$$T\big|_{y=0} - T_w = \left[\beta_{t1}\lambda\frac{\partial T}{\partial y} - \beta_{t2}\lambda^2\frac{\partial^2 T}{\partial y^2}\right]_{y=0} \tag{1.8}$$

Although previous studies have demonstrated the usefulness of second-order slip velocity boundary conditions with respect to evaluating experimentally determined mass flow rates and/or pressure distributions [28, 30] and numerically determined DSMC or Boltzmann equation velocity profiles and/or mass flow rates [1, 22-24, 29, 32-34], there is currently no consensus on which velocity slip/temperature jump boundary condition model is most accurate and widely applicable.

Table 1.1. Second-order boundary condition coefficients

	Maxwell-Smoluchowski [16, 17], Eqs. (1.1) and (1.2)	Deissler [20], Eqs. (1.3) and (1.4)	Karniadakis and Beskok [1], Eqs. (1.5) and (1.6)
β_{v2}	0	$\frac{9}{8}$	$-\frac{\beta_{v1}}{2}$
β_{t2}	0	$\left(\frac{9}{128}\right)\left(\frac{177\gamma-145}{\gamma+1}\right)$	$-\frac{\beta_{t1}}{2}$

A conclusion regarding the usefulness of any particular second-order boundary condition model with respect to evaluating convective heat transfer rates within the slip flow and transition flow regimes requires comparison of analytical and numerical data produced using these models to experimental data. Currently, however, experimental measurements of local convective heat transfer rates within the slip flow regime do not exist, and analytical and numerical convective heat transfer solutions based on second-order slip boundary conditions models are limited [1, 20, 35-39].

1.2. Scaling and fabrication effects

In addition to rarefaction effects, which are generally only significant for gaseous microflows, there are other effects that are a result of scaling and microfabrication techniques [2]. Scaling effects are not unique to microflows, but whereas in a macrosystem they are typically negligible, in a microsystem they become more prominent and may even dominate the flow characteristics. Many of the scaling effects in microfluidic systems are a consequence of the increased surface area to volume ratio. This results in increased surface forces, which may produce large pressure drops, compressibility effects, and viscous dissipation; decreased inertial forces, which allows diffusion and conduction processes to become relatively more significant; and increased heat transfer, which may lead to variable fluid properties and creep flow. Furthermore, microfluidic systems are often manufactured by conventional microfabrication methods, i.e., lithography, bulk micromachining, surface micromachining, etc. These methods produce structures made of materials such as Si, SiO_2, Si_3N_4, Pyrex glass, etc., which have properties, surface characteristics, and fluid-surface interactions that are not common in macroscale systems, and consequently are not accounted for in conventional correlations. Many microfabrication methods also produce large aspect ratio, planar, rectangular, and trapezoidal geometries that are not common in conventional systems. These geometries alter the typical flow characteristics, and may also intentionally or unintentionally result in components that deflect with the pressure of the fluid, thereby producing fluid-structure-interaction (FSI) effects. Any of these scaling or manufacturing effects could be either beneficial or detrimental to a microfluidic system, depending on its function, but in either case must be accounted for to accurately model the system.

1.3. Research objectives

Although there are many potential applications for microfluidic systems, and it is known that microflows are subject to rarefaction, scaling, and manufacturing effects, the significance of these effects on the system function is often unknown, and design data for microfluidic systems which include these effects are limited or nonexistent. Because microfluidic effects have proven difficult to isolate and study experimentally, and are often too complex to study analytically, the objective of this research is to contribute to the advancement of numerical modeling capabilities and methodologies for microfluidic systems, and numerically obtain design data for several common microsystem configurations and effects. The following studies have been selected based on the unique numerical capabilities available, as well as the expected contribution to the advancement of these capabilities; the fundamental nature and general applicability of the results to be obtained; and the absence of these data in previous studies.

1. The convective heat transfer rates and frictional losses of rarified, steady state, laminar, constant wall temperature and constant wall heat flux internal rectangular microchannel flows are investigated. Effects of aspect ratio, rarefaction, creep flow, viscous dissipation, axial conduction, and thermally/hydrodynamically developing flow are considered. These effects on frictional losses and convective heat transfer rates are given through the Poiseuille number, Po, and Nusselt number, Nu, respectively.
2. The momentum and thermal energy exchange models of the fluid-structure-interaction algorithm utilized for these studies are modified, such that the equivalent of first-order slip velocity and temperature jump boundary conditions are achieved at fluid-solid surfaces which may move and deform with time. The resulting modified algorithm is then verified for 1) velocity profiles of a rarified gas between parallel plates; 2) temperature profiles of a rarified gas between parallel plates; 3) drag coefficients, C_D, and Nusselt numbers, Nu, for low Reynolds number rarified flow around a two-dimensional cylinder; and, 4) the transient, thermal and structural response of a damped-oscillatory three-dimensional finite cylinder subject to an impulsively started uniform rarified flow.

1.4. Chapter arrangement

- Chapter 2 briefly describes the numerical algorithm, discusses the modifications required to accurately describe microfluidic systems, and presents results for several simple cases to support the algorithm's use in the subsequent microscale studies.
- Chapter 3 presents results and discussion for two-dimensional *Po*, and constant wall heat flux *Nu*, as functions of second-order slip boundary conditions, creep flow, viscous dissipation, and thermally/ hydrodynamically developing flow. These results have also been published in [40] and [41].
- Chapter 4 contains results and discussion for rectangular channel, constant wall heat flux and constant wall temperature *Nu*, as a function of second-order slip boundary conditions, viscous dissipation, and thermally/hydrodynamically developing flow. These results have also been published in [42], and in part in [43-45].
- Chapter 5 gives results and discussion for rectangular channel, constant wall heat flux and constant wall temperature *Po* and *Nu*, as functions of second-order slip boundary conditions, creep flow, viscous dissipation, and axial conduction, for thermally/hydrodynamically fully developed flow. These results have also been published in [46], and in part in [44, 45].
- Chapter 6 presents the development, implementation, and verification of slip flow momentum and energy exchange models, such that the equivalent of first-order slip velocity and temperature jump boundary conditions are achieved at the fluid-solid surface of fluid-structure-interaction problems.
- Chapter 7 is a summary and discussion of conclusions and recommendations for the results presented in Chapters 1-6.

1.5. Nomenclature

C_D	drag coefficient
c_p	specific heat at constant pressure
c_v	specific heat at constant volume
D_h	hydraulic diameter
f	friction factor, $8\tau_{w,m}/\rho u_m^2$
k	thermal conductivity
Kn	Knudsen number, λ/D_h
Nu	Nusselt number, $q''_{w,m}D_h/(k(T_w - T_m))$
P	pressure
Po	Poiseuille number, $f\ Re$
Pr	Prandtl number, $c_p\mu/k$
q''	heat flux
R	gas constant
Re	Reynolds number, $\rho u_m D_h/\mu$
T	temperature
u	streamwise velocity
u_c	creep velocity, $(3/4)(\mu R/P)\partial T/\partial x\|_{y=0}$
x, y, z	Cartesian coordinates

1.5.1. Greek symbols

β_{t1}	first-order temperature jump coefficient, $((2-\sigma_t)/\sigma_t)(2\gamma/(1+\gamma))(1/Pr)$
β_{t2}	second-order temperature jump coefficient

β_{v1}	first-order velocity slip coefficient, $(2-\sigma_v)/\sigma_v$
β_{v2}	second-order velocity slip coefficient
γ	ratio of specific heats, c_p/c_v
λ	molecular mean free path, $\mu/\rho\sqrt{2RT_w/\pi}$
μ	dynamic viscosity
ρ	density
σ_t	thermal accommodation coefficient
σ_v	momentum accommodation coefficient
τ	shear stress

1.5.2. Subscripts

m	mean value
w	wall value

1.6. References

[1] G.E. Karniadakis, A. Beskok, Micro Flows: Fundamentals and Simulation, Springer-Verlag, New York, 2002.

[2] M.J. Madou, Fundamentals of Microfabrication: The Science of Miniaturization, CRC Press, Boca Raton, 2002.

[3] J.A. Pelesko, D.H. Bernstein, Modeling MEMS and NEMS, Chapman & Hall/CRC, Boca Raton, 2003.

[4] W.W. Liou, Y. Fang, Microfluid Mechanics: Principles and Modeling, McGraw-Hill, New York, 2006.

[5] E.B. Arkilic, K.S. Breuer, M.A. Schmidt, Gaseous flow in microchannels, in: Proceedings of American Society of Mechanical Engineers, Fluids Engineering Division, Chicago, Illinois, United States, 1994, pp. 57-66.

[6] K.-C. Pong, C.-M. Ho, J. Liu, Y.-C. Tai, Non-linear pressure distribution in uniform microchannels, in: Proceedings of American Society of Mechanical Engineers, Fluids Engineering Division, Chicago, Illinois, United States, 1994, pp. 51-56.

[7] J. Liu, Y.-C. Tai, C.-M. Ho, MEMS for pressure distribution studies of gaseous flows in microchannels, in: Proceedings of the IEEE Micro Electro Mechanical Systems, Amsterdam, Netherlands, 1995, pp. 209-215.

[8] J.C. Shih, C.-M. Ho, J. Liu, Y.-C. Tai, Monatomic and polyatomic gas flow through uniform microchannels, in: Proceedings of American Society of Mechanical Engineers, Dynamic Systems and Control Division, Atlanta, Georgia, United States, 1996, pp. 197-203.

[9] E.B. Arkilic, M.A. Schmidt, K.S. Breuer, Gaseous slip flow in long microchannels, J. Microelectromech. Syst. 6 (2) (1997) 167-178.

[10] E.B. Arkilic, K.S. Breuer, M.A. Schmidt, Mass flow and tangential momentum accommodation in silicon micromachined channels, J. Fluid Mech. 437 (2001) 29-43.

[11] S.Y.K. Lee, M. Wong, Y. Zohar, Gas flow in microchannels with bends, J. Micromech. Microeng. 11 (6) (2001) 635-644.

[12] W.Y. Lee, M. Wong, Y. Zohar, Microchannels in series connected via a contraction/expansion section, J. Fluid Mech. 459 (2002) 187-206.

[13] W.Y. Lee, M. Wong, Y. Zohar, Pressure loss in constriction microchannels, J. Microelectromech Syst. 11 (3) (2002) 236-244.

[14] K.B. Cheng, M. Wong, Y. Zohar, Parallel and series multiple microchannel systems, in: Proceedings of the IEEE Micro Electro Mechanical Systems, Kyoto, Japan, 2003, pp. 291-294.

[15] J. Jang, S.T. Wereley, Pressure distributions of gaseous slip flow in straight and uniform rectangular microchannels, Microfluid. Nanofluid. 1 (1) (2004) 41-51.

[16] J.C. Maxwell, On stresses in rarified gases arising from inequalities of temperature, Phil. Trans. R. Soc. Lond. 170 (1879) 231-256.

[17] M. Smoluchowski, Ueber wärmeleitung in verdünnten gasen, Annal. Phys. Chem. 64 (1898) 101-130.

[18] J.M. Reese, M.A. Gallis, D.A. Lockerby, New directions in fluid dynamics: non-equilibrium aerodynamic and microsystem flows, Phil. Trans. R. Soc. Lond. A 361 (1813) (2003) 2967-2988.

[19] S.H. Maslen, On heat transfer in slip flow, J. Aeronaut. Sci. 25 (1958) 400-401.

[20] R.G. Deissler, An analysis of second-order slip flow and temperature-jump boundary conditions for rarefied gases, Int. J. Heat Mass Transfer 7 (1964) 681-694.

[21] R. Goniak, G. Duffa, Corrective term in wall slip equations for Knudsen layer, J. Thermophys. Heat Transfer 9 (2) (1995) 383-384.

[22] J. Dai, D. Xu, C. Khoo Boo, Y. Lam Khin, Navier–Stokes simulation of gas flow in micro devices, J. Micromech. Microeng. 10 (2000) 372-379.

[23] J.-M. Li, B.-X. Wang, X.-F. Peng, `Wall-adjacent layer' analysis for developed-flow laminar heat transfer of gases in microchannels, Int. J. Heat Mass Transfer 43 (5) (2000) 839-847.

[24] H. Xue, Q. Fan, A new analytic solution of the Navier-Stokes equations for microchannel flows, Microscale Thermophys. Eng. 4 (2) (2000) 125-143.

[25] N.G. Hadjiconstantinou, Dissipation in small scale gaseous flows, J. Heat Transfer 125 (5) (2003) 944-947.

[26] N.G. Hadjiconstantinou, Comment on Cercignani's second-order slip coefficient, Phys. Fluids 15 (8) (2003) 2352-2354.

[27] D.A. Lockerby, J.M. Reese, High-resolution Burnett simulations of micro Couette flow and heat transfer, J. Comput. Phys. 188 (2) (2003) 333-347.

[28] J. Maurer, P. Tabeling, P. Joseph, H. Willaime, Second-order slip laws in microchannels for helium and nitrogen, Phys. Fluids 15 (9) (2003) 2613-2621.

[29] Y.H. Sun, W.K. Chan, N.Y. Liu, A slip model for gas lubrication based on an effective viscosity concept, Proc. IME J. J. Eng. Tribol. 217 (3) (2003) 187-196.

[30] S. Colin, P. Lalonde, R. Caen, Validation of a second-order slip flow model in rectangular microchannels, Heat Transfer Eng. 25 (3) (2004) 23-30.

[31] Y. Sun, W.K. Chan, Analytical modeling of rarefied Poiseuille flow in microchannels, J. Vac. Sci. Tech. A 22 (2) (2004) 383-94.

[32] D.A. Lockerby, J.M. Reese, M.A. Gallis, A wall-function approach to incorporating Knudsen-layer effects in gas micro flow simulations, in: Proceedings of AIP 24th International Symposium on Rarefied Gas Dynamics, Bari, Italy, 2005, pp. 731-736.

[33] M.J. McNenly, M.A. Gallis, I.D. Boyd, Empirical slip and viscosity model performance for microscale gas flow, Int. J. Numer. Meth. Fluid 49 (11) (2005) 1169-1191.

[34] Y. Zheng, J.M. Reese, T.J. Scanlon, D.A. Lockerby, Scaled Navier-Stokes-Fourier equations for gas flow and heat transfer phenomena in micro- and nanosystems, in: Proceedings of the 4th International Conference on Nanochannels, Microchannels and Minichannels ICNMM2006, Limerick, Ireland, 2006, pp. 369-376.

[35] G. An, J.-M. Li, B.-X. Wang, Laminar heat transfer of gas in a parallel-plate microchannel with one wall temperature constant and the other adiabatic, Heat Transfer - Asian Res. 32 (1) (2003) 58-64.

[36] G. Croce, V. Arato, Numerical simulation of gaseous flow and heat transfer in laminar slip flow regime, in: Proceedings of the 3rd International Conference on Microchannels and Minichannels ICMM2005, Toronto, Canada, 2005, pp. 447-452.

[37] C.o.-K. Chen, H.C. Weng, Developing natural convection with thermal creep in a vertical microchannel, J. Phys. D 39 (14) (2006) 3107-3118.

[38] J.N. Chung, J. Yan, Y. Kun, Numerical simulation of wall roughness on gaseous flow and heat transfer in a microchannel, Int. J. Heat Mass Transfer 49 (7-8) (2006) 1329-39.

[39] N. Xiao, J. Elsnab, S. Thomas, T. Ameel, Isothermal microtube heat transfer with second-order slip flow and temperature jump boundary conditions, in: Proceedings of 2006 ASME International Mechanical Engineering Congress and Exposition IMECE2006, Chicago, IL, United States, 2006, p. 9.

[40] J. van Rij, T. Harman, T. Ameel, The effect of creep flow on two-dimensional isoflux microchannels, in: Proceedings of the 4th International Conference on Nanochannels, Microchannels and Minichannels ICNMM2006, Limerick, Ireland, 2006, pp. 467-474.

[41] J. van Rij, T. Harman, T. Ameel, The effect of creep flow on two-dimensional isoflux microchannels, Int. J. Thermal Sci. 46 (11) (2007) 1095-1103.

[42] J. van Rij, T. Ameel, T. Harman, The effect of viscous dissipation and rarefaction on rectangular microchannel convective heat transfer, Int. J. Thermal Sci. 48 (2) (2009) 271-281.

[43] J. van Rij, T. Ameel, T. Harman, The effect of viscous dissipation on two-dimensional microchannel heat transfer, in: Proceedings of 2006 ASME International Mechanical Engineering Congress and Exposition IMECE2006, Chicago, IL, United States, 2006, p. 9.

[44] J. van Rij, T. Ameel, T. Harman, Constant wall temperature Nusselt and Poiseuille numbers in rectangular microchannels, in: Proceedings of 2007 ASME-JSME Thermal Engineering Summer Heat Transfer Conference HT2007, Vancouver, BC, Canada, 2007, pp. 893–900.

[45] J. van Rij, T. Ameel, T. Harman, Effects of creep flow and viscous dissipation in the slip regime for isoflux rectangular microchannels, in: Proceedings of 2007 ASME International Mechanical Engineering Congress and Exposition IMECE2007, Seattle, WA, United States, 2007, pp. 971–978.

[46] J. van Rij, T. Ameel, T. Harman, An evaluation of secondary effects on microchannel frictional and convective heat transfer characteristics, Int. J. Heat Mass Transfer 52 (11-12) (2009) 2792-2801.

CHAPTER 2

ALGORITHM DESCRIPTION AND PRELIMINARY VERIFICATION

MPM-ICE, an existing, continuum based, three-dimensional, unsteady, compressible fluid-structure-interaction algorithm has been selected to complete the studies outlined in Chapter 1. To accurately model microfluidic systems, several modifications to this algorithm, including slip velocity boundary conditions, temperature jump boundary conditions, creep flow boundary conditions, and viscous dissipation terms, are required. Following the implementation of these modifications, several basic configurations are examined to verify the algorithm's use in the subsequent microscale studies.

2.1. Algorithm description

The computational algorithm selected to complete the studies outlined in Chapter 1 is a three-dimensional, unsteady, continuum based Eulerian-Lagrangian methodology in which fluids, modeled using ICE (implicit, continuous fluid, Eulerian) and solid materials, modeled with MPM (the material-point-method), may be modeled either independently or simultaneously. ICE is a finite volume, cell-centered, multimaterial, compressible, computational-fluid-dynamics (CFD) algorithm that originated at Los Alamos National Laboratory [1, 2]. And, MPM is a particle based method for solid mechanics simulations [3, 4]. The development and documentation of the MPM-ICE implementation currently used by the University of Utah group is given in [5-8]. The multimaterial conservation equations utilized by the algorithm, without effects that are not considered in the present research (chemical reactions, turbulence, multiphase Reynolds stress, gravity, etc.), are given in Eqs. (2.1) - (2.3) [8]. Equations (2.1) - (2.3) are the ensemble average, r-material, conservation of mass, momentum, and energy equations respectively, where there are N materials, θ_r is the r-material volume fraction, and $\sum_{s=1}^{N} \boldsymbol{f}_{rs}$ and $\sum_{s=1}^{N} q_{rs}$ are models for the momentum and energy exchange between materials.

$$\frac{\partial \rho_r}{\partial t} + \nabla \cdot (\rho \boldsymbol{u})_r = 0 \tag{2.1}$$

$$\frac{\partial (\rho \boldsymbol{u})_r}{\partial t} + \nabla \cdot (\rho \boldsymbol{u}\boldsymbol{u})_r = -\theta_r \nabla P + \nabla \cdot (\theta \boldsymbol{\tau})_r + \sum_{s=1}^{N} \boldsymbol{f}_{rs} \tag{2.2}$$

$$\frac{\partial (\rho e)_r}{\partial t} + \nabla \cdot (\rho e \boldsymbol{u})_r = -\frac{P\theta_r}{\upsilon_r}\frac{d\upsilon_r}{dt} + (\theta \boldsymbol{\tau})_r : \nabla \boldsymbol{u}_r + \nabla \cdot (\theta_r k_r \nabla T_r) + \sum_{s=1}^{N} q_{rs} \tag{2.3}$$

Equations (2.1) – (2.3), along with material constitutive or equation-of-state models, and models for $\sum_{s=1}^{N} \boldsymbol{f}_{rs}$ and $\sum_{s=1}^{N} q_{rs}$, form a complete system of equations. The detailed numerical solution strategy utilized by the algorithm to solve this system of equations is well documented [2, 5-8], and consequently will not be duplicated here, aside from the context necessary to introduce subsequent modifications.

Advancing the ability to numerically model microfluidic systems with the MPM-ICE algorithm, a continuum approach, rather than a molecular approach, such as the Boltzmann equation or direct-simulation-Monte-Carlo (DSMC), is significant for two reasons. First, the majority of existing microfluidic systems operate in the continuum, slip, or lower transition Knudsen number regimes; all regimes for which continuum approaches have proven effective [9]. And second, with the goal of not only modeling simple configurations, but of eventually numerically designing and optimizing complex, multiscale, multiphysics, microsystems, the continuum based approach is currently the only feasible option. While molecular methods based on the Boltzmann equation or DSMC are accurate for all ranges of Knudsen number, they are generally computationally limited to very small, simple (one- or two-dimensional) configurations, and do not easily integrate with conventional continuum based computational fluid dynamic codes and design methods [10]. Although this research will not use all of the algorithm's described capabilities, its use is merited for several additional reasons. By developing and verifying the algorithm’s ability to model microflows, the algorithm may then potentially be used in future studies for even more complicated microscale systems, which, utilizing the code’s more advanced capabilities, would not be feasible with most commercial algorithms. Also, as a research code it is much more flexible in comparison to commercial codes and relatively easy to make customized changes to, such as slip boundary conditions. And finally, the code is supported by significant computing power and expertise.

2.2. Microscale modifications

To accurately model microflows using the MPM-ICE algorithm, several additional capabilities must be implemented and verified. Slip velocity, temperature jump, and creep flow boundary conditions must be implemented to account for the effects of rarefaction. These boundary conditions are implemented in the algorithm in two separate ways. The first approach, utilized for single fluid, internal flow problems is to apply slip flow boundary conditions at the boundaries of the computational domain within the ICE algorithm. This approach is used for the studies presented in Chapters 3 - 5, where Maxwell-Smoluchowski, Eqs. (1.1) and (1.2), second-order Deissler, Eqs. (1.3) and (1.4), and second-order Karniadakis and Beskok, Eqs. (1.5) and (1.6), slip boundary conditions models have been implemented in the algorithm. The implementation of these boundary conditions is consistent with the existing code in being numerically second-order accurate. In addition to each of the three slip boundary condition models, conventional no-slip boundary conditions may also still be applied, such that the contribution of each boundary condition model may be observed in comparison.

The second approach, applied to fluid-structure-interaction problems, is to implement slip flow boundary conditions at fluid-solid surfaces. This approach is used for the studies presented in Chapter 6. The MPM-ICE algorithm currently employs the scalar momentum and energy exchange models given in Eq. (2.4) and (2.5), respectively, to specify the rate at which momentum and thermal energy is transferred between materials for standard continuum conditions.

$$\sum_{s=1}^{N} \boldsymbol{f}_{rs} = \sum_{s=1}^{N} K_{rs}\theta_r\theta_s\left(\boldsymbol{u}_s - \boldsymbol{u}_r\right) \tag{2.4}$$

$$\sum_{s=1}^{N} q_{rs} = \sum_{s=1}^{N} H_{rs}\theta_r\theta_s\left(T_s - T_r\right) \tag{2.5}$$

Eq. (2.4) models $\boldsymbol{f}_{rs}$, the force per unit volume on material r, due to interaction with material s, as a function of the scalar momentum exchange coefficient, K_{rs}, the material volume fractions, and the relative velocity between the two materials. Similarly, Eq. (2.5) models q_{rs}, the thermal energy exchange rate per unit volume for material r, due to interaction with material s, as a function of the scalar energy exchange coefficient, H_{rs}, the material volume fractions, and the temperature difference between the two materials.

A very large momentum transfer rate between materials *r* and *s*, specified by a large K_{rs}, forces the relative velocity of the two materials to zero, effectively, a no-slip velocity boundary condition. Similarly, a large H_{rs} produces a large thermal energy transfer rate between materials *r* and *s*, resulting in the equivalent of a thermal equilibrium boundary condition. In the current algorithm, K_{rs} and H_{rs} values are typically specified as arbitrarily large, constant, scalar quantities ($\sim 1\times 10^{15}$), which, result in momentum and thermal energy transfer rates that are not directional relative to the fluid-solid surface, but produce the intended effect of conventional no-slip velocity and temperature jump boundary conditions. To achieve the equivalent of first-order slip velocity and temperature jump boundary conditions at the fluid-solid surface, slip flow momentum and energy exchange coefficients are first derived as functions of the local level of rarefaction. Then, the slip flow momentum and thermal energy exchange models, with a directional momentum exchange coefficient, is applied at fluid-solid surfaces. Because the implementation and verification of this interaction is the subject of Chapter 6, further details are reported there.

As stated previously in Chapter 1, viscous dissipation effects are often significant for microflows. Calculation of the viscous dissipation term, $\left(\theta\boldsymbol{\tau}\right)_{\mathrm{r}} : \nabla\boldsymbol{u}_{r}$ in Eq. 2.3, however, is not included in the original ICE algorithm. For a single, compressible, Newtonian fluid system, viscous dissipation, commonly denoted as Φ, is given by Eq. (2.6) [11]. This viscous dissipation term has been added to the energy calculation in the algorithm, that is, the numerical implementation of Eq. 2.3, using central difference approximations for the derivatives. This calculation is numerically second-order accurate, and may be either included or neglected with each simulation, such that its contribution to the numerical result may be observed.

$$\Phi = \mu\left[2\left(\frac{\partial u}{\partial x}\right)^2 + 2\left(\frac{\partial v}{\partial y}\right)^2 + 2\left(\frac{\partial w}{\partial z}\right)^2 + \left(\frac{\partial v}{\partial x}+\frac{\partial u}{\partial y}\right)^2 + \left(\frac{\partial w}{\partial y}+\frac{\partial v}{\partial z}\right)^2 + \left(\frac{\partial u}{\partial z}+\frac{\partial w}{\partial x}\right)^2 - \frac{2}{3}\left(\frac{\partial u}{\partial x}+\frac{\partial v}{\partial y}+\frac{\partial w}{\partial z}\right)^2\right] \tag{2.6}$$

2.3. Preliminary verification

To verify that the modifications discussed above have been implemented correctly and that the resulting algorithm is capable of completing the research outlined in Chapter 1, several preliminary algorithm verifications were completed. For each case, the numerical result is substantiated with comparison to either analytic solutions, fundamental numerical solutions, or experimental solutions. Because these results are presented primarily for the sake of verification, discussion of the meaning of the various parameters and physical effects is reserved for the associated references and later chapters.

2.3.1. Poiseuille flow

To verify the implementation of the first- and second-order velocity slip boundary conditions and the combined effects of rarefaction and compressibility, the two-dimensional, fully developed, steady state, Newtonian, ideal gas, isothermal, pressure driven flow with constant properties and negligible inertial forces, depicted in Fig. 2.1(a), is numerically modeled. The analytic velocity solution is obtained by integrating the momentum equation, $\mu\left(\partial^2 u/\partial y^2\right) = dP/dx$, twice and applying the general slip velocity boundary condition given in Eq. (1.7) at $y = 0$ and h. The resulting analytic velocity profile, given by Eqs. (2.7) and (2.8), and the Boltzmann equation solution, as presented by [12] for comparable conditions (hard sphere molecules, diffuse reflection boundary condition, uniform pressure gradient, negligible inertial forces), are compared to the present numerical velocity solutions in Figs. 2.1(b) and 2.1(c) for the Kn_m, Ma_m, β_{v1} and β_{v2} values specified. The average difference between all numerical and analytical data, of comparable boundary conditions, is 0.14%, and the maximum difference is 0.17%. Compared to the Boltzmann equation solution, the average numerical error is 3.55% for $\beta_{v2} = 0.0$, the Maxwell model [13], 7.50% for $\beta_{v2} = 1.125$, the Deissler model [14], and 2.86% for $\beta_{v2} =-0.5$, the Karniadakis and Beskok model [9]. These results verify that the modified algorithm accurately represents the three slip velocity boundary condition models implemented.

$$\frac{u(y/h)}{u_m} = \frac{6\left(y/h - y^2/h^2 + 2\beta_{v1} Kn + 8\beta_{v2} Kn^2\right)}{1 + 12\beta_{v1} Kn + 48\beta_{v2} Kn^2} \tag{2.7}$$

$$u_m = -\frac{h^2}{12\mu}\frac{dP}{dx}\left(1 + 12\beta_{v1} Kn + 48\beta_{v2} Kn\right) \tag{2.8}$$

The analytic, mean axial pressure distribution is derived by integrating, Eq. (2.8), along the length of the channel, and applying the specified inlet and outlet pressures, P_i and P_o, at $x = 0$ and L, respectively [9]. For the first-order slip velocity boundary condition, $\beta_{v2} = 0.0$, the resulting analytic pressure distribution, given by Eq. (2.9), and experimentally measured pressure distribution data from [15], are compared to the numerical pressure distribution results, also obtained with $\beta_{v2} = 0.0$, in Fig. 2.1(d), for the outlet Knudsen number, Kn_o, and pressure ratios, P_i/P_o, specified.

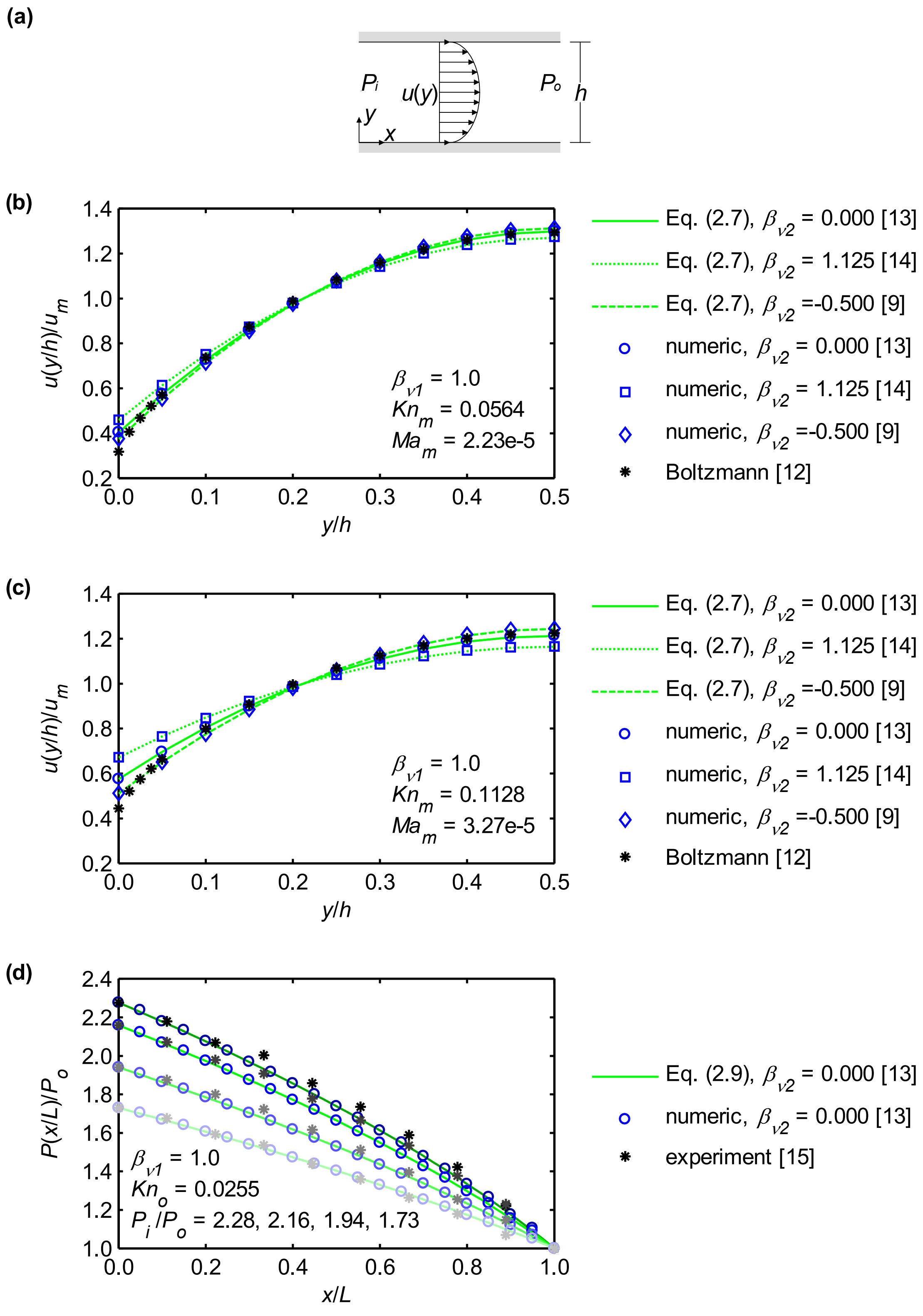

Fig. 2.1. Poiseuille flow: (a) configuration, (b) velocity profile, $Kn_m = 0.0564$, (c) velocity profile, $Kn_m = 0.1128$, (d) pressure distribution, $P_i/P_o = 2.28, 2.16, 1.94, 1.73$.

The average absolute difference between numerical and analytical values is 0.14%, while the maximum difference is 1.3%. Between numerical and experimental values, the average difference is 1.64% and the maximum difference is 4.66%. These results verify, and validate, that the modified algorithm accurately represents the combined effects of rarefaction and compressibility.

$$\frac{P(x/L)}{P_o} = -12\beta_{v1}Kn_o + \sqrt{\left(\frac{P_i}{P_o} + 12\beta_{v1}Kn_o\right)^2 - \left(\frac{x}{L}\right)\left(\frac{P_i}{P_o} - 1\right)\left(1 + \frac{P_i}{P_o} + 24\beta_{v1}Kn_o\right)} \tag{2.9}$$

2.3.2. Couette flow

To further verify the implementation of first-order slip velocity boundary conditions, as well as the first- and second-order temperature jump boundary conditions and the viscous dissipation term, the two-dimensional, fully developed, steady state, Newtonian, ideal gas ($Pr = 0.715$, $\gamma = 1.4$), shear driven flow with constant properties, as shown in Figure 2.2(a), is numerically modeled. The analytic velocity solution is obtained by integrating the momentum equation, $\mu\left(\partial^2 u/\partial y^2\right) = 0$, twice and applying the general slip velocity boundary condition given in Eq. (1.7) at $y = 0$ and h (because $\partial^2 u/\partial y^2 = 0$, the second-order slip velocity boundary condition term does not have an effect). The resulting analytic velocity solution, Eq. (2.10), and the Boltzmann equation solution, as presented by [16] for comparable conditions (hard sphere molecules, diffuse reflection boundary condition), are compared to the numerical velocity solutions in Fig. 2.2(b) and 2.2(c) for the parameters specified. The average and maximum difference between analytic and numeric data is 0.09% and 0.44%, respectively, while the average difference between the analytic and the Boltzmann equation data is 2.27%.

$$\frac{u(y/h)}{u_w} = \frac{-1+2(y/h)}{1+4\beta_{v1}Kn} \tag{2.10}$$

Using the same assumptions as stated above, the analytic solution to the temperature profile is derived by substituting the velocity profile, Eq. (2.10), into the energy equation, $\left(\partial^2 T/\partial y^2\right) = -(\mu/k)(\partial u/\partial y)^2$, integrating twice, and applying the general temperature jump boundary condition given in Eq. (1.8) at $y = 0$ and h. The resulting analytic temperature distribution, Eq. (2.11), is presented in terms of the Brinkman number, $Br = \mu u_w^2 / k(T_m - T_w)$, which is the parameter typically used to quantify viscous dissipation effects. The DSMC solution presented by [17], Eq. (2.11), and the numerical temperature results are compared in Fig. 2.2(d) for each of the three temperature jump boundary condition models and the Br, Ma_w, and Kn_w values specified. The average difference between all numerical and analytical data of comparable boundary conditions is 0.84% while the maximum difference is 3.07%. Due to the statistical scatter, typical of DSMC data, the average error between analytic and DSMC data is 14.59% for $\beta_{t2} = 0.0$, the Smoluchowski model [18], 16.21% for $\beta_{t2} = 3.012$, the Deissler model [14], and 16.18% for $\beta_{t2} =-0.816$, the Karniadakis and Beskok model [9]. However, the similar trends between the numerical data and the DSMC data, and the negligible errors between the analytic and numeric data presented in Fig. 2.2, verify that the modified algorithm accurately represents first- and second-order temperature jump boundary conditions with viscous dissipation effects.

$$\frac{T(y/h)-T_w}{T_m - T_w} = 2Br \cdot \frac{2\beta_{t1}Kn + 8\beta_{t2}Kn^2 + (y/h) - (y/h)^2}{(1+4\beta_{v1}Kn)^2} \tag{2.11}$$

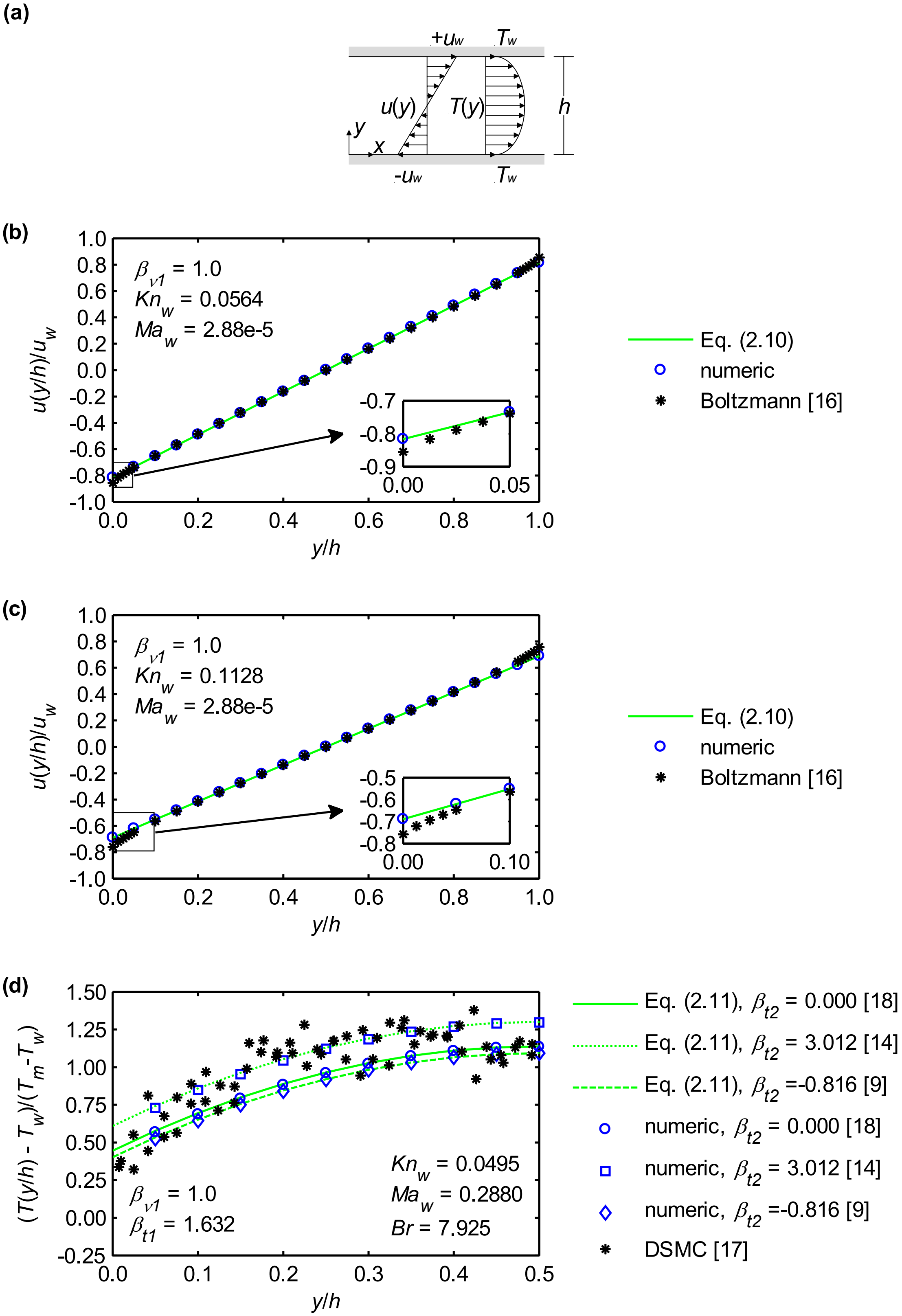

Fig. 2.2. Couette flow: (a) configuration, (b) velocity profile, $Kn_m = 0.0564$, (c) velocity profile, $Kn_m = 0.1128$, (d) temperature profile, $Kn_w = 0.0495$.

2.3.3. Creep flow

To verify the implementation of the creep flow boundary condition, the two-dimensional, fully developed, steady state, Newtonian, ideal gas, temperature gradient driven flow with constant properties and negligible inertial forces, as shown in Fig. 2.3(a), is numerically modeled. The analytic solution to the velocity profile, $u_c = (3/4)(\mu R/P)(\partial T/\partial x)\big|_{y=0}$ [13], and the Boltzmann equation solution, as presented by [12] for comparable conditions (hard sphere molecules, diffuse reflection boundary condition, uniform temperature gradient, negligible inertial forces), are compared to the numerical velocity solutions in Fig. 2.3(b) and 2.3(c) for the parameters specified. The average and maximum differences between analytical and numerical data are 0.77% and 1.07%, while the average difference between the analytic solution and Boltzmann equation data is 16.77%. These results indicate that the numerical implementation of creep flow boundary conditions produces negligible error when compared to analytic data. The analytic solution, however, while accurate in predicting the overall mass flow rate for a thermally driven flow, is somewhat of a simplification with respect to the actual velocity profile that will, consequently, affect numerically predicted frictional and heat transfer values at high u_c and Kn.

The preceding verifications of the described microscale modifications to the algorithm support the use of the modified algorithm for the research outlined in Chapter 1. As each of the studies outlined in Chapter 1 are completed, the resulting numerical data must be substantiated. To accomplish this, the numerical data are compared to analytical, and previously published numerical and experimental data for the cases in which these data exist. Generally, however, the research studies outlined have been

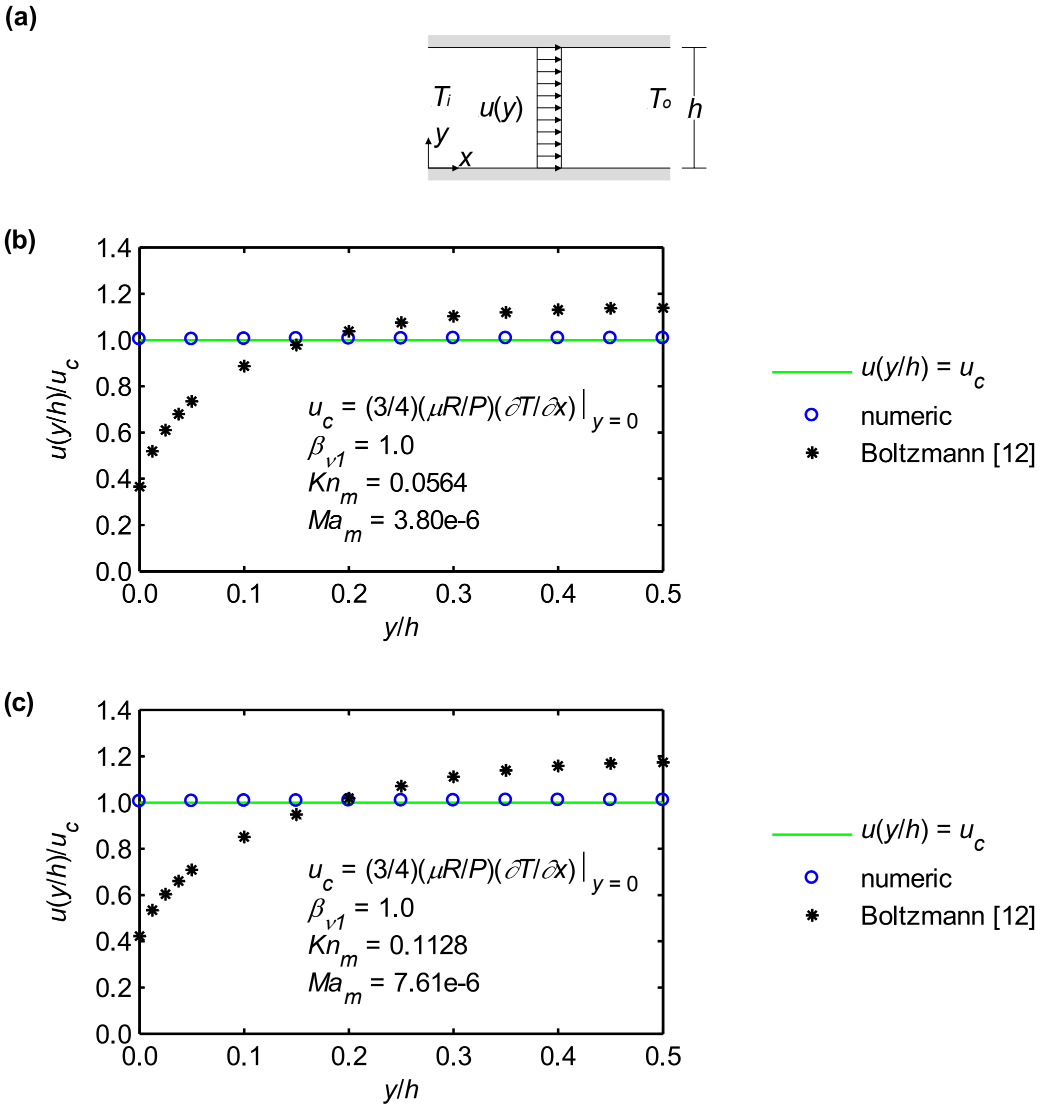

Fig. 2.3. Creep flow: (a) configuration, (b) velocity profile, $Kn_m = 0.0564$, (c) velocity profile, $Kn_m = 0.1128$.

selected specifically because data for these configurations do not yet exist. As such, grid convergence studies are completed for each problem to verify that the solution converges as expected, and that a grid independent solution is approached. Additionally, general trends in the resulting numerical predictions, due to specific effects, such as rarefaction, viscous dissipation, geometry, etc., are compared to similar, simpler configurations for which results have been established, and physical explanations for trends are given.

2.4. Nomenclature

Br	Brinkman number, $\mu u_w^2 / k(T_m - T_w)$
c_p	specific heat at constant pressure
c_v	specific heat at constant volume
D_h	hydraulic diameter
e	internal energy per unit mass
$\boldsymbol{f}$	force per unit volume
H_{rs}	energy exchange coefficient
h	channel height
K_{rs}	momentum exchange coefficient
k	thermal conductivity
Kn	Knudsen number, λ / D_h
L	channel length
Ma	Mach number, $Re\,Kn\sqrt{2/(\pi\gamma)}$
N	number of materials
P	pressure
Pr	Prandtl number, $c_p \mu / k$
q	thermal energy exchange rate
R	gas constant
Re	Reynolds number, $\rho u_m D_h / \mu$
T	temperature
t	time
$\boldsymbol{u}$	velocity vector

u	x velocity
u_c	creep velocity, $(3/4)(\mu R/P)\partial T/\partial x\|_{y=0}$
v	y velocity
w	z velocity
x,y, z	Cartesian coordinates

2.4.1. Greek symbols

β_{t1}	first-order temperature jump coefficient, $((2-\sigma_t)/\sigma_t)(2\gamma/(1+\gamma))(1/Pr)$
β_{t2}	second-order temperature jump coefficient
β_{v1}	first-order velocity slip coefficient, $(2-\sigma_v)/\sigma_v$
β_{v2}	second-order velocity slip coefficient
γ	ratio of specific heats
θ	volume fraction
λ	molecular mean free path, $\mu/\rho\sqrt{2RT_w/\pi}$
μ	dynamic viscosity
ρ	density
σ_t	thermal accommodation coefficient
σ_v	momentum accommodation coefficient
$\boldsymbol{\tau}$	shear stress
υ	specific volume
Φ	viscous dissipation

2.4.2. Subscripts

i	inlet property
m	mean value
o	outlet property
r	material index
s	material index
w	wall value

2.5. References

[1] F. Harlow, A. Amsden, Numerical calculation of almost incompressible flow, J. Comput. Phys. 3 (1968) 80-93.

[2] B.A. Kashiwa, N.T. Padial, R.M. Rauenzahn, W.B. VanderHeyden, A Cell-Centered ICE Method for Multiphase Flow Simulations, Los Alamos National Laboratory Technical Report LA-UR-93-3922, 1993.

[3] J.U. Brackbill, D.B. Kothe, H.M. Ruppel, FLIP: A low-dissipation, particle-in-cell method for fluid flow, Comput. Phys. Comm. 48 (1) (1987) 25-38.

[4] D. Sulsky, Z. Shi-Jian, H.L. Schreyer, Application of a particle-in-cell method to solid mechanics, Comput. Phys. Comm. 87 (1-2) (1995) 236-252.

[5] B.A. Kashiwa, A Multifield Model and Method for Fluid-Structure Interaction Dynamics, Los Alamos National Laboratory Technical Report LA-UR-01-1136, 2001.

[6] J.E. Guilkey, T. Harman, A. Xia, B. Kashiwa, P. McMurtry, An Eulerian-Lagrangian approach for large deformation fluid structure interaction problems, part 1: Algorithm development, in: S.K. Chakrabarti (Ed.), Fluid Structure Interaction II: Proceedings of the Second International Conference on Fluid Structure Interaction, Cadiz, Spain, WIT Press, Boston, 2003, pp. 143-156.

[7] T. Harman, J.E. Guilkey, B. Kashiwa, J. Schmidt, P. McMurtry, An Eulerian-Lagrangian approach for large deformation fluid structure interaction problems, part 2: Multi-physics simulations within a modern computational framework, in: S.K. Chakrabarti (Ed.), Fluid Structure Interaction II: Proceedings of the Second International Conference on Fluid Structure Interaction, Cadiz, Spain, WIT Press, Boston, 2003, pp. 157-166.

[8] J.E. Guilkey, T.B. Harman, B. Banerjee, An Eulerian–Lagrangian approach for simulating explosions of energetic devices, Comput. Struct. 85 (2007) 660-674.

[9] G.E. Karniadakis, A. Beskok, Micro Flows: Fundamentals and Simulation, Springer-Verlag, New York, 2002.

[10] J.M. Reese, M.A. Gallis, D.A. Lockerby, New directions in fluid dynamics: non-equilibrium aerodynamic and microsystem flows, Phil. Trans. R. Soc. Lond. A 361 (1813) (2003) 2967-2988.

[11] J.D. Anderson, Computational Fluid Dynamics: The Basics With Applications, McGraw-Hill, New York, 1995.

[12] T. Ohwada, Y. Sone, K. Aoki, Numerical analysis of the Poiseuille and thermal transpiration flows between two parallel plates on the basis of the Boltzmann equation for hard-sphere molecules, Phys. Fluids 1 (12) (1989) 2042-2049.

[13] J.C. Maxwell, On stresses in rarified gases arising from inequalities of temperature, Phil. Trans. R. Soc. Lond. 170 (1879) 231-256.

[14] R.G. Deissler, An analysis of second-order slip flow and temperature-jump boundary conditions for rarefied gases, Int. J. Heat Mass Transfer 7 (1964) 681-694.

[15] J.C. Shih, C.-M. Ho, J. Liu, Y.-C. Tai, Monatomic and polyatomic gas flow through uniform microchannels, in: Proceedings of American Society of Mechanical Engineers, Dynamic Systems and Control Division, Atlanta, Georgia, United States, 1996, pp. 197-203.

[16] Y. Sone, S. Takata, T. Ohwada, Numerical analysis of the plane Couette flow of a rarefied gas on the basis of the linearized Boltzmann equation for hard-sphere molecules, Eur. J. Mech. B Fluid 9 (3) (1990) 273-288.

[17] Y. Fang, W.W. Liou, Computations of the flow and heat transfer in microdevices using DSMC with implicit boundary conditions, J. Heat Transfer 124 (2) (2002) 338-345.

[18] M. Smoluchowski, Ueber wärmeleitung in verdünnten gasen, Annal. Phys. Chem. 64 (1898) 101-130.

CHAPTER 3

THE EFFECT OF CREEP FLOW ON TWO-DIMENSIONAL ISOFLUX MICROCHANNELS

Available online at www.sciencedirect.com
ScienceDirect
International Journal of Thermal Sciences 46 (2007) 1095–1103
International Journal of Thermal Sciences
www.elsevier.com/locate/ijts

The effect of creep flow on two-dimensional isoflux microchannels

Jennifer van Rij, Todd Harman, Timothy Ameel *

Department of Mechanical Engineering, University of Utah, Salt Lake City, UT 84112, USA

Received 6 July 2006; received in revised form 14 April 2007; accepted 15 April 2007

Abstract

Microchannel convective heat transfer and friction loss characteristics are numerically evaluated for gaseous, two-dimensional, steady state, laminar, constant wall heat flux flows. The effects of Knudsen number, accommodation coefficients, second-order slip boundary conditions, creep flow, and hydrodynamically/thermally developing flow are considered. These effects are compared through the Poiseuille number and the Nusselt number. Numerical values for the Poiseuille and Nusselt numbers are obtained using a continuum based three-dimensional, unsteady, compressible computational fluid dynamics algorithm that has been modified with slip boundary conditions. To verify the numerical results, analytic solutions of the hydrodynamically and thermally fully developed momentum and energy equations have been derived subject to both first- and second-order slip velocity and temperature jump boundary conditions. The resulting velocity and temperature profiles are then utilized to obtain the microchannel Poiseuille and Nusselt numbers as a function of Knudsen number, first- and second-order velocity slip and temperature jump coefficients, Brinkman number, and the ratio of the thermal creep velocity to the mean velocity. Excellent agreement between the numerical and analytical data is demonstrated. Second-order slip terms and creep velocity are shown to have significant effects on microchannel Poiseuille and Nusselt numbers within the slip flow regime.

Keywords: Microchannel; Slip; Creep; Viscous dissipation; Nusselt number; Poiseuille number

1. Introduction

Convective heat transfer and friction losses of gaseous microchannel flows are important due to their applications in microscale heat exchangers, sensors, reactors, power systems, etc. However, due to measurement and accuracy limitations there are currently no experimental data on convective heat transfer rates of gaseous microchannel flows in the slip regime. For this reason, accurate numerical models, verified by analytical solutions, are particularly important in the process of understanding and designing these microfluidic systems.

Numerous studies on microchannel convective heat transfer in the slip flow regime for both constant wall temperature and constant wall heat flux have been conducted. The majority of these studies have been analytical [1–8], although there are also several numerical studies based on either direct simulation Monte Carlo, DSMC [9–11], or on continuum methods with slip boundary conditions [12,13]. Nearly all of these studies have used the following simplifying assumptions: laminar, steady state, hydrodynamically fully developed, constant properties, no creep flow, and first-order accurate slip velocity and temperature jump boundary conditions with perfectly accommodating walls. Parameters that have been found to affect microchannel heat transfer rates and friction losses include the Knudsen number, the momentum and thermal accommodation coefficients, channel aspect ratio, compressibility, viscous dissipation, and the Peclet number. However, many of the simplifying assumptions and conclusions of these studies have not yet been verified numerically or experimentally, nor have the effects of creep, second-order accurate slip boundary conditions, or combined hydrodynamic/thermal flow development been fully investigated.

Theoretical studies within the slip flow regime ($0.01 \leqslant Kn \leqslant 0.1$) typically use the continuum momentum and energy equations with the slip boundary conditions shown in Eqs. (1) and (2) to account for rarefaction effects. The velocity slip boundary condition, Eq. (1), was first introduced by

---

[*] Corresponding author. Tel.: +1 801 585 9730; fax: +1 801 585 9826.
E-mail address: ameel@mech.utah.edu (T. Ameel).

1290-0729/$ – see front matter © 2007 Elsevier Masson SAS. All rights reserved.
doi:10.1016/j.ijthermalsci.2007.04.007

Nomenclature

Br	Brinkman number, $\mu u_m^2/q_o'' D_h$	
c_p	specific heat at constant pressure	$\mathrm{J\,kg^{-1}\,K^{-1}}$
D_h	hydraulic diameter, $2h$	m
f	friction factor, $8\tau_w/\rho u_m^2$	
h	channel height	m
k	thermal conductivity	$\mathrm{W\,m^{-1}\,K^{-1}}$
Kn	Knudsen number, λ/D_h	
Ma	Mach number, $u/\sqrt{kRT}$	
Nu	Nusselt number, $q_o'' D_h/k(T_w - T_m)$	
P	fluid pressure	Pa
Pe	Peclet number, $Pr \cdot Re$	
Po	Poiseuille number, $f \cdot Re$	
Pr	Prandtl number, $c_p\mu/k$	
q_o''	wall heat flux, $-k\partial T/\partial y\|_{y=0}$	$\mathrm{W\,m^{-2}}$
R	gas constant	$\mathrm{J\,kg^{-1}\,K^{-1}}$
Re	Reynolds number, $\rho u_m D_h/\mu$	
T	fluid temperature	K
T_m	mixed mean temperature, $(1/hu_m)\int_0^h u(y)\cdot T(y)\,\mathrm{d}y$	K
T_w	wall temperature	K
u	streamwise velocity	$\mathrm{m\,s^{-1}}$
u_c	creep velocity, $(3/4)(\mu/\rho T_w)\partial T/\partial x\|_{y=0}$	$\mathrm{m\,s^{-1}}$
u_m	mean velocity, $(1/h)\int_0^h u(y)\,\mathrm{d}y$	$\mathrm{m\,s^{-1}}$
u_s	slip velocity, $u\|_{y=0}$	$\mathrm{m\,s^{-1}}$
x, y, z	Cartesian coordinates	m

Greek symbols

α	thermal diffusivity, $k/\rho c_p$	$\mathrm{m^2\,s^{-1}}$
β_{T1}	first-order temperature jump coefficient, $((2-\sigma_T)/\sigma_T)(2\gamma/(\gamma+1))(1/Pr)$	
β_{T2}	second-order temperature jump coefficient	
β_{V1}	first-order velocity slip coefficient, $(2-\sigma_V)/\sigma_V$	
β_{V2}	second-order velocity slip coefficient	
ε	relative error	
γ	ratio of specific heat capacities	
λ	molecular mean free path, $\mu/\rho\sqrt{2RT_w/\pi}$	m
μ	viscosity	$\mathrm{kg\,m^{-1}\,s^{-1}}$
ρ	density	$\mathrm{kg\,m^{-3}}$
σ_T	thermal accommodation coefficient	
σ_V	momentum accommodation coefficient	
τ_w	wall shear stress, $\mu\partial u/\partial y\|_{y=0}$	Pa

Maxwell [14], and the temperature jump boundary condition, Eq. (2), was originally proposed by Smoluchowski [15].

$$u|_{y=0} = \left(\frac{2-\sigma_V}{\sigma_V}\right)\lambda\frac{\partial u}{\partial y}\bigg|_{y=0} + \frac{3}{4}\frac{\mu}{\rho T_w}\frac{\partial T}{\partial x}\bigg|_{y=0} \tag{1}$$

$$T|_{y=0} - T_w = \left(\frac{2-\sigma_T}{\sigma_T}\right)\left(\frac{2\gamma}{\gamma+1}\right)\frac{\lambda}{Pr}\frac{\partial T}{\partial y}\bigg|_{y=0} \tag{2}$$

Values for the momentum and thermal accommodation coefficients range from 0 to 1, where these values represent complete specular and diffuse reflections, respectively. The first term in Eq. (1) is the velocity slip due to the wall shear stress, and the second term is the thermal creep velocity, u_c, due to the streamwise temperature gradient. Eqs. (1) and (2) are first-order approximations, in Kn, and only applicable in the slip flow regime. However, in an effort to improve the slip flow model, and extend the continuum equations' range of applicability into the transition regime ($0.1 \leqslant Kn \leqslant 1.0$), several second-order slip boundary condition models have been proposed. The boundary conditions derived by Deissler [16] are given in Eqs. (3) and (4), and the boundary conditions suggested by Karniadakis and Beskok [17] are given in Eqs. (5) and (6).

$$u|_{y=0} = \left(\frac{2-\sigma_V}{\sigma_V}\right)\lambda\frac{\partial u}{\partial y}\bigg|_{y=0} - \frac{9\lambda^2}{8}\left[\frac{\partial^2 u}{\partial y^2} + \frac{1}{2}\frac{\partial^2 u}{\partial x^2} + \frac{1}{2}\frac{\partial^2 u}{\partial z^2}\right]_{y=0} + u_c \tag{3}$$

$$T|_{y=0} - T_w = \left(\frac{2-\sigma_T}{\sigma_T}\right)\left(\frac{2\gamma}{\gamma+1}\right)\frac{\lambda}{Pr}\frac{\partial T}{\partial y}\bigg|_{y=0} - \frac{9\lambda^2}{128}\left(\frac{177\gamma-145}{\gamma+1}\right) \times \left[\frac{\partial^2 T}{\partial y^2} + \frac{1}{2}\frac{\partial^2 T}{\partial x^2} + \frac{1}{2}\frac{\partial^2 T}{\partial z^2}\right]_{y=0} \tag{4}$$

$$u|_{y=0} = \left(\frac{2-\sigma_V}{\sigma_V}\right)\left[\lambda\frac{\partial u}{\partial y} + \frac{\lambda^2}{2}\frac{\partial^2 u}{\partial y^2}\right]_{y=0} + u_c \tag{5}$$

$$T|_{y=0} - T_w = \left(\frac{2-\sigma_T}{\sigma_T}\right)\left(\frac{2\gamma}{\gamma+1}\right)\frac{1}{Pr}\left[\lambda\frac{\partial T}{\partial y} + \frac{\lambda^2}{2}\frac{\partial^2 T}{\partial y^2}\right]_{y=0} \tag{6}$$

In addition to these two sets of boundary conditions, many other second-order boundary conditions have been proposed for the slip velocity, without a complimentary temperature jump boundary condition, and so will not be considered here. Although there is currently no consensus on which set of second-order boundary conditions is most accurate, it has been shown experimentally that the use of second-order boundary conditions does extend the range of the continuum approach when modeling microchannel mass flow rates [17–19]. For this reason, it is important that the effects of second-order slip boundary conditions on convective heat transfer be evaluated as well.

This study will analytically and numerically evaluate two-dimensional microchannel flows with constant wall heat flux using the continuum conservation equations and the various forms of the slip boundary condition models presented in Eqs. (1)–(6). The effects of Knudsen number, accommodation coefficients, and creep flow on microchannel friction losses and convective heat transfer will be evaluated numerically through the Poiseuille number, Po, and the Nusselt number, Nu. To validate the numerical model, analytic solutions for the hydrodynamically and thermally fully developed values of *Po* and *Nu*, which include the effects of second-order slip boundary conditions, creep velocity, and viscous dissipation, will be derived. With the numerical method verified, it will then be used to evaluate the thermally and hydrodynamically developing flows considered in this study, as well as more complex geometries and heating configurations in future studies.

2. Analytic solution

The flow configuration for the analytical model is shown in Fig. 1. The following simplifying assumptions are applied: two-dimensional, steady state, incompressible, thermally and hydrodynamically fully developed, symmetrically isoflux, Newtonian, ideal gas, constant properties, and laminar flow. With these simplifications the momentum equation takes the form

$$\frac{\partial^2 u}{\partial y^2} = \frac{1}{\mu}\frac{\mathrm{d}P}{\mathrm{d}x} \tag{7}$$

and the energy equation is

$$\frac{\partial^2 T}{\partial y^2} = \frac{u}{\alpha}\frac{\partial T}{\partial x} - \frac{u}{k}\frac{\partial P}{\partial x} - \frac{\mu}{k}\left(\frac{\partial u}{\partial y}\right)^2 \tag{8}$$

where both the pressure and temperature gradients in the x-direction are constants.

For two-dimensional, fully developed, planar flow all three sets of slip boundary conditions, Eqs. (1)–(6), may be written in the forms

$$u|_{y=0} = \left[\beta_{V1}\lambda\frac{\partial u}{\partial y} - \beta_{V2}\lambda^2\frac{\partial^2 u}{\partial y^2}\right]_{y=0} + u_c \tag{9}$$

$$T|_{y=0} = T_w + \left[\beta_{T1}\lambda\frac{\partial T}{\partial y} - \beta_{T2}\lambda^2\frac{\partial^2 T}{\partial y^2}\right]_{y=0} \tag{10}$$

Values for the first-order slip coefficient, β_{V1}, are typically near unity while values for the first-order jump coefficient, β_{T1}, may range from 0 to 100. The second-order slip and jump coefficients, β_{V2} and β_{T2}, vary depending on the model selected and are given in Table 1.

Using the general form of the slip velocity boundary condition, Eq. (9), and symmetry at the microchannel midplane, the momentum equation, Eq. (7), may be integrated twice to obtain the nondimensional velocity profile.

$$\frac{u(y)}{u_m} = \frac{u_s}{u_m} + 6\left(1 - \frac{u_s}{u_m}\right)\left(\frac{y}{h} - \frac{y^2}{h^2}\right) \tag{11}$$

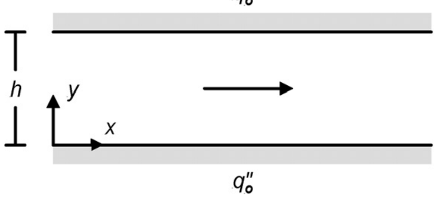

Fig. 1. Flow configuration.

Table 1
Second-order velocity slip and temperature jump coefficients

	First-order [14,15]	Second-order [16]	Second-order [17]
β_{V2}	0	$\frac{9}{8}$	$-\frac{\beta_{V1}}{2}$
β_{T2}	0	$\frac{9}{128}(\frac{177\gamma-145}{\gamma+1})$	$-\frac{\beta_{T1}}{2}$

Where u_s/u_m is defined as

$$\frac{u_s}{u_m} = 1 - \frac{(1 - u_c/u_m)}{(1 + 12\beta_{V1}Kn + 48\beta_{V2}Kn^2)} \tag{12}$$

The ratio u_c/u_m may be calculated based on the known mass flow rate, the flow properties, and the wall heat flux. With the velocity profile defined, the Poiseuille number may be expressed as

$$Po = 96\left(1 - \frac{u_s}{u_m}\right) \tag{13}$$

The velocity profile, Eq. (11), is substituted into the energy equation, Eq. (8), which is then integrated twice. The general form of the temperature jump boundary condition, Eq. (10), and symmetry at the midplane, are then applied to obtain the nondimensional temperature profile.

$$\begin{aligned}\frac{T_w - T(y)}{q''_o D_h/k} &= \left(\frac{1}{2}\right)\left(\frac{y}{h} - \frac{y^2}{h^2}\right)\left\{1 + \left[1 + 12Br\left(3 - \frac{u_s}{u_m}\right)\left(1 - \frac{u_s}{u_m}\right)\right]\right.\\ &\quad\left.\times\left(1 - \frac{u_s}{u_m}\right)\left(\frac{y}{h} - \frac{y^2}{h^2}\right)\right\} + \beta_{T1}Kn + 4\beta_{T2}Kn^2\\ &\quad\times\left[\frac{u_s}{u_m} - 12Br\left(3 - \frac{u_s}{u_m}\right)\left(1 - \frac{u_s}{u_m}\right)^2\right]\end{aligned} \tag{14}$$

Where the Brinkman number, *Br*, represents the effects of viscous dissipation. Using the temperature profile in Eq. (14) and the definitions of the mixed mean temperature, T_m, and the Nusselt number, *Nu*, the final form for the Nusselt number is

$$\begin{aligned}Nu = 420&\left[51 + 420\beta_{T1}Kn - 2\frac{u_s}{u_m}\left(9 - \frac{u_s}{u_m} - 840\beta_{T2}Kn^2\right)\right.\\ &+ 12Br\left(3 - \frac{u_s}{u_m}\right)\left(1 - \frac{u_s}{u_m}\right)^2\\ &\left.\times\left(9 - 2\frac{u_s}{u_m} - 1680\beta_{T2}Kn^2\right)\right]^{-1}\end{aligned} \tag{15}$$

Nu presented in Eq. (15), with u_s/u_m defined in Eq. (12), expresses the thermal energy exchange of a two-dimensional, fully developed, isoflux microchannel in terms of the degree of rarefaction (*Kn*); slip flow model parameters, β_{V1}, β_{V2}, β_{T1}, and β_{T2}; creep flow (u_c/u_m); and viscous dissipation (*Br*). For continuum flow ($Kn = 0$), with negligible viscous dissipation ($Br = 0$), Eq. (15) reduces to the continuum value of 8.235. For continuum flow, with viscous dissipation, Eq. (15) reduces to the *Nu* equation given in [20] for flow with viscous dissipation. For slip flow with no viscous dissipation, no creep flow ($u_c/u_m = 0$), and first-order slip terms only ($\beta_{V2} = \beta_{T2} = 0$), Eq. (15) reduces to the equation originally derived by Inman [17] (with $Kn = \lambda/h$, rather than $Kn = \lambda/2h$ used here). Although it is expected that these solutions for *Po* and *Nu*, given by Eqs. (13) and (15) respectively, are more accurate than first-order models and models that do not include creep and viscous dissipation effects they are still only applicable to situations of approximately the same conditions for which the solutions were derived, that is two-dimensional, isoflux, nearly incompressible, constant property flows within the slip flow regime.

3. Computational model

The computational fluid dynamics (CFD) algorithm used in this study is based on the ICE (Implicit, Continuous-fluid Eulerian) method. ICE is a finite volume, multi-material CFD algorithm that originated [21], and was subsequently developed, at Los Alamos National Laboratory [22]. The ICE implementation used in this study is well developed and documented [23–25]. The code is three-dimensional, fully compressible, unsteady, and capable of modeling variable fluid properties, fluid-structure interactions, and chemical reactions. Although, the present study will not use the majority of the algorithms described capabilities, it has been selected for several reasons. First, by developing and verifying the algorithm's capability to model slip flow in this study, it may then be used in future studies for more complicated microscale flows which utilize the code's more advanced capabilities and would consequently not be feasible with most commercial CFD algorithms. Second, as an 'open' research code it is very flexible in comparison to commercial codes and relatively easy to make customized changes to, such as second-order slip boundary conditions. And finally, when using this code there is significant computing power and expertise available where the study is performed.

To accurately model microchannel flows using this algorithm, several additional capabilities have been implemented and verified. These modifications include slip flow with creep velocity boundary conditions, temperature jump boundary conditions, and viscous dissipation. The implementation of these modifications is consistent with the existing code in being numerically second-order accurate both spatially and temporally. Any form of the slip boundary conditions presented in Eqs. (1)–(6) may be numerically employed. Also, any of these modifications may be either included or neglected with each calculation, such that each contribution to the numerical result may be observed.

3.1. Model parameters and solution criteria

To decrease the computational time required to reach a solution only half of the symmetric microchannel, shown in Fig. 1, is modeled. Two types of problems are numerically evaluated, thermally developing flows and combined hydrodynamically/thermally developing flows. For both cases the channel outlet pressure is specified to obtain the desired flow *Kn*. For thermally developing flows, the inlet pressure is specified to obtain the desired flow *Pe*, while the inlet and outlet velocities are allowed to evolve to their fully developed profiles. For hydrodynamically/thermally developing flows, a uniform inlet velocity is specified to obtain the desired flow *Pe*, while the inlet pressure and outlet velocity are allowed to evolve. For both cases, a uniform inlet temperature is specified while the outlet temperature is allowed to evolve to its fully developed profile; and a uniform heat flux boundary condition and slip velocity boundary condition, dependent on the flow *Kn*, are applied at the channel wall.

Because the algorithm is unsteady the flow properties must evolve from a set of initial conditions to steady state conditions subject to the boundary conditions. For all of the data presented, the initial velocity field is zero and the initial temperature field is equal to the inlet temperature. The magnitude and number of time steps required to reach steady state are dependent on the grid resolution, *Kn*, and *Pe* for each flow. The convergence criteria for each time step is a mass flux residual less than 10^{-8} for each control volume. The criterion used to establish that the flow is steady state is, $|(u^{n+1} - u^n)/u^{n+1}| \leqslant 10^{-10}$ and $|(T^{n+1} - T^n)/T^{n+1}| \leqslant 10^{-10}$, for each control volume, where n is the number of the time step.

For the numerical results to be comparable to the analytic solutions, the flow must be fully developed, steady state, nearly incompressible, and have constant properties. Given these stipulations, the flow *Pe*, and wall heat flux are specified to be small enough that the density and temperature changes within the flow are less than a few percent and the flow Mach number (*Ma*) is small. Using constant properties of air, $Pe = 0.5$, and $Kn = 0.01$, 0.04, and 0.12 the resulting $Ma = 0.005$, 0.019, and 0.056, respectively. For the *Pe* values used in this study a channel length of $3h$ was found to be sufficient for the parameters of interest, *Po* and *Nu*, to reach nearly constant, locally fully developed values while avoiding significant compressibility effects due to a longer channel. (Evidence of this statement will be seen shortly in the plots presented for developing *Po* and *Nu* in Figs. 2, and 9–12.)

3.2. Grid dependence

The resulting numerical velocity and temperature fields may be used to calculate *Po* and *Nu* along the length of the microchannel. The accuracy of the numerical solutions and the time required to reach a steady-state solution are dependent on the grid resolution. This is shown for thermally developing *Nu* with the conditions specified in Table 2 and Fig. 2. These data indicate that the numerical solution converges to the exact analytic solution with approximately second-order numerical accuracy, and that the solution is sufficiently accurate at the finest resolution that is practical due to computational time limitations. Grid dependence studies have been completed with similar results for each numerical solution presented in the results section, with only the results from the finest resolution (40×120 for each case) being presented. It may also be observed in Fig. 2, that as stated previously, *Nu* reaches a nearly constant, locally fully developed state well before the end of the channel at $3h$.

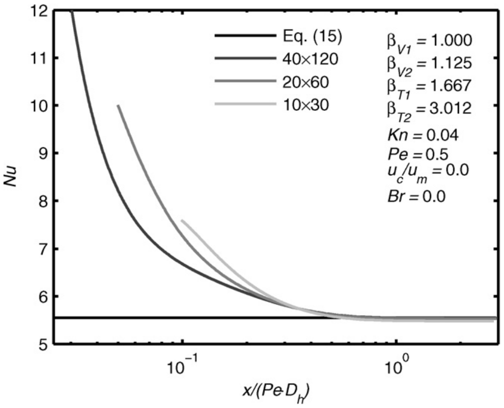

Fig. 2. Grid dependence data.

Table 2
Conditions for the grid dependence study

Grid resolution	Nu_∞	ε_{Nu_∞}	Po_∞	ε_{Po_∞}	Time
Eq. (13) or (15)	5.550	–	61.287	–	–
40 × 120	5.545	−0.08%	61.238	−0.08%	116 h
20 × 60	5.533	−0.31%	61.092	−0.32%	3.75 h
10 × 30	5.482	−1.23%	60.515	−1.26%	0.75 h

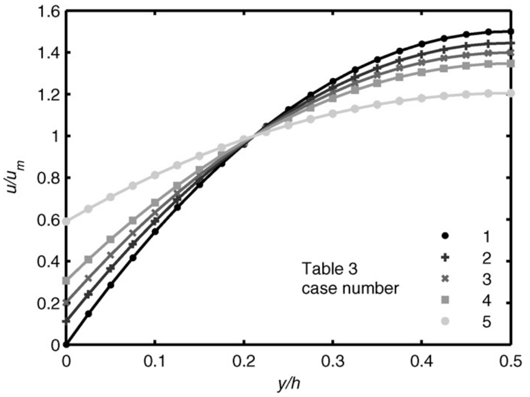

Fig. 3. Analytical and numerical velocity profiles.

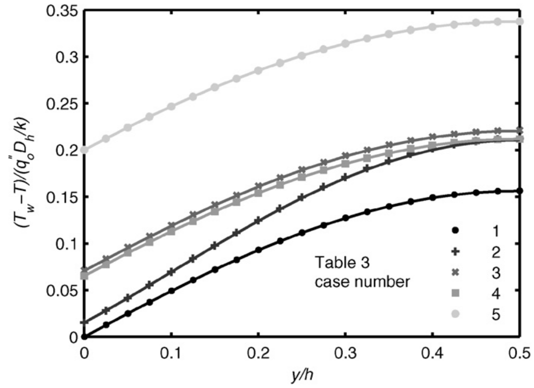

Fig. 4. Analytical and numerical temperature profiles.

Table 3
Conditions for comparison of analytical and numerical velocity and temperature profiles

Case number	Boundary condition	β_{V1}	β_{T1}	Kn	$\frac{u_c}{u_m}$	Br
1	no slip	1.0	1.667	0.00	0.00	0.00
2	second-order [16]	1.0	1.667	0.01	0.00	0.05
3	second-order [16]	1.0	1.667	0.04	−0.25	0.00
4	second-order [17]	1.0	1.667	0.04	0.00	0.00
5	first-order [14,15]	1.0	1.667	0.12	0.00	0.00

3.3. *Code verification*

To verify that the numerical algorithm accurately models the effects of the various slip boundary conditions, creep velocity, and viscous dissipation the analytically and numerically computed fully developed velocity and temperature profiles are compared in Figs. 3 and 4 for the flow conditions specified in Table 3. The nondimensional velocity profiles are given in Fig. 3, where the symbols represent the numerically computed values and the lines represent the analytic solution, Eq. (11). The nondimensional temperature profiles are presented in Fig. 4, where the lines again represent the analytic solutions, Eq. (14). The differences between the numerically and analytically computed values are negligible.

4. Results and discussion

In the following presentation of the numerical and analytical results *Po* and *Nu* are normalized by their continuum values, which are 96 and 8.235, respectively. Also, to reduce the number of variables involved, the nondimensional parameters, $\beta_{V1}Kn$ and β_{T1}/β_{V1}, introduced by Larrode et al. [4], will be used. $\beta_{V1}Kn$ represents the level of rarefaction, with $\beta_{V1}Kn = 0$ corresponding to continuum conditions. The ratio β_{T1}/β_{V1} represents the gas-wall interactions, and may range from 0 to more than 100. $\beta_{T1}/\beta_{V1} = 1.667$ corresponds to typical properties for air when $\sigma_V = \sigma_T = 1$. $\beta_{T1}/\beta_{V1} = 0$ corresponds to the artificial condition of a no temperature jump boundary condition while there is a slip velocity boundary condition. It should be noted that when second-order Deissler boundary conditions are used either analytically or numerically, if $\beta_{T1} = 0$ then β_{T2} is also taken to be zero, although this is not explicitly stated in the boundary conditions presented in Eq. (4). Also, although it has been verified that the algorithm accurately models flows with viscous dissipation (Table 3, case number 2), by comparison to Eqs. (11) and (14), numerical results that include viscous dissipation will not be presented here so that second-order effects and creep flow effects may be seen more clearly.

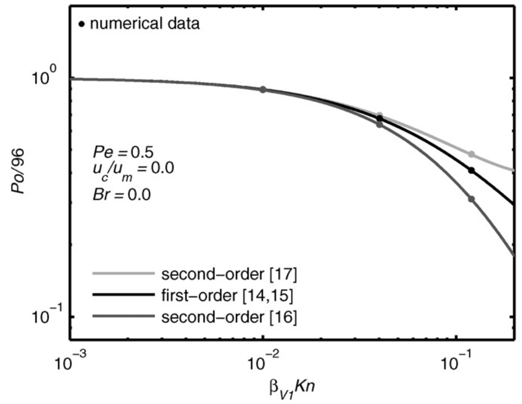

Fig. 5. Effect of slip boundary conditions on fully developed *Po*.

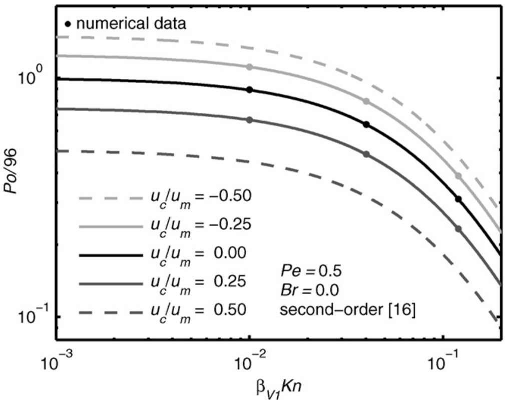

Fig. 7. Effect of creep velocity on fully developed *Po*.

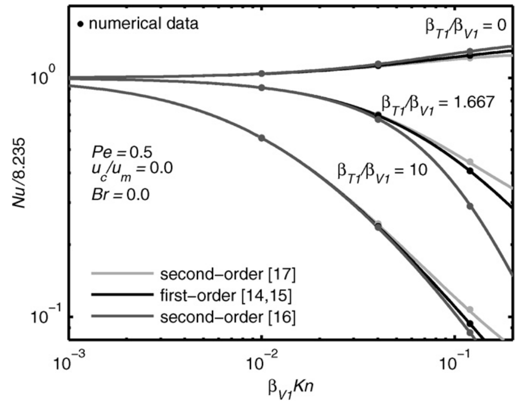

Fig. 6. Effect of slip boundary conditions on fully developed *Nu*.

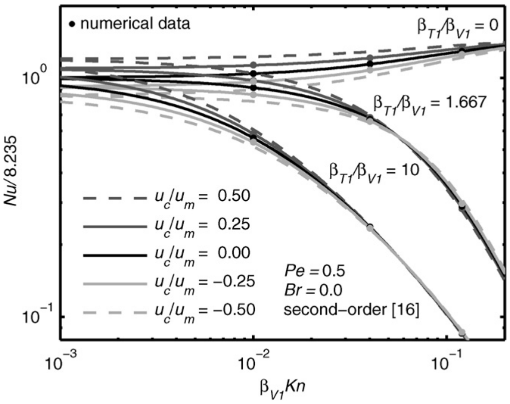

Fig. 8. Effect of creep velocity on fully developed *Nu*.

4.1. Fully developed Po and Nu

The numerical results for fully developed flows are compared to the analytically derived *Po* and *Nu* in Figs. 5–8. The numerical data are given by the symbols, and the analytic solutions are represented as lines. The average difference between the analytic *Po*, Eq. (13), and the numerical *Po* is 0.06%, and the maximum difference is 0.70%. The average difference between the analytic *Nu*, Eq. (15), and the numerical *Nu* is 0.33%, and the maximum difference is 1.72%.

The comparison of the resulting *Po*, when using first-order [14,15], second-order Deissler [16], or second-order Karniadakis and Beskok [17] boundary conditions is given in Fig. 5. A similar comparison for *Nu* is given in Fig. 6. For these data, creep flow and viscous dissipation effects are neglected, and $Pe = 0.5$. The data in Fig. 5 illustrate that as rarefaction, $\beta_{V1}Kn$, increases, the slip velocity increases, which results in a flatter velocity profile with reduced wall velocity gradients (as shown in Fig. 3) and consequently decreases *Po*. The increased slip flow at the wall, due to increasing rarefaction also amplifies the energy exchange near the wall which tends to increase *Nu*, as seen when $\beta_{T1}/\beta_{V1} = 0$ in Fig. 6. However, when $\beta_{T1}/\beta_{V1} \neq 0$, rarefaction increases the temperature jump at the wall as well as the slip velocity, which reduces the energy exchange and results in a shift in the temperature distribution (as shown in Fig. 4) which increases the mean temperature difference and consequently tends to decrease *Nu*. These results are consistent with previous first-order slip results [4,8] and indicate that slip decreases *Po*, and may either increase or decrease *Nu* depending on the magnitude of $\beta_{V1}Kn$ and β_{T1}/β_{V1}.

The results presented in Figs. 5 and 6 also indicate that second-order slip terms become more significant as rarefaction, $\beta_{V1}Kn$, increases. However, it is important to observe that the two second-order models have opposite effects when compared to the first-order boundary condition data. This result is expected, due to the opposite signs of the second-order coefficients, given in Table 1. The second-order Deissler coefficients are positive, which result in an increase in both the slip velocity and the temperature jump for increasing rarefaction, while the second-order Karniadakis and Beskok coefficients are negative, which result in a decrease for both the slip velocity and the temperature jump for increasing rarefaction. At $\beta_{V1}Kn = 0.12$ and $\beta_{T1}/\beta_{V1} = 1.667$, the second-order Deissler boundary conditions predict a 24.2% decrease in *Po* and a 28.0% decrease in *Nu*, as compared to the first-order boundary conditions, while the Karniadakis and Beskok boundary conditions predict a 16.5% increase in *Po* and a 8.2% increase in *Nu*, as compared to the first-order boundary conditions.

The effect of creep velocity on *Po* and *Nu* is shown in Figs. 7 and 8, respectively. For these data, viscous dissipation effects are neglected, second-order Deissler boundary conditions are used, and $Pe = 0.5$. The data in Fig. 7 indicate that creep flow in the same direction as the mean flow, positive u_c/u_m, increases the total slip velocity, which flattens the velocity profile and reduces *Po*. Conversely, creep flow in the opposite direction of the mean flow, negative u_c/u_m, decreases the total slip velocity at the wall, which increases the wall velocity gradient, thereby increasing *Po*.

There are several factors that contribute to the creep flow effect on *Nu*, as presented in Fig. 8. Creep flow in the same direction as the mean flow increases the total slip velocity, which increases the energy exchange near the wall and tends to increase *Nu*. Creep flow in the opposite direction of the mean flow decreases the total slip velocity, which decreases the energy exchange near the wall and tends to decrease *Nu*. This creep flow effect on *Nu* is seen most clearly for the lower $\beta_{V1}Kn$ values of Fig. 8. However, as rarefaction increases, the effect of the increasing temperature jump at the wall (for $\beta_{T1}/\beta_{V1} \neq 0$), and the decreasing velocity gradients decrease the energy exchange, which reduces *Nu*, as well as the effect of u_c/u_m on *Nu*. As rarefaction increases even further, the second-order effects become more significant. The second-order contribution to the temperature distribution, the last term of Eq. (14), is a function of the second-order temperature jump coefficient, β_{T2}, rarefaction, Kn^2, the total slip velocity, u_s/u_m, and the viscous dissipation, *Br* ($Br = 0$ for these calculations). Creep flow in the same direction as the mean flow increases the total slip velocity, thereby increasing the second-order effect on the temperature jump; whereas, creep flow in the opposite direction of the mean flow decreases the overall slip velocity, thereby decreasing the second-order effect on the temperature jump. For the second-order Deissler boundary conditions, which are used for the analysis in Fig. 8, this causes the lines of positive and negative u_c/u_m to cross at high $\beta_{V1}Kn$ (for $\beta_{T1}/\beta_{V1} \neq 0$). While not shown, neither the first-order, nor the second-order Karniadakis and Beskok boundary conditions with creep flow result in this effect at high $\beta_{V1}Kn$.

4.2. Entrance Po and Nu

Comparisons of numerically computed *Po* and *Nu* for thermally developing and combined hydrodynamically/thermally developing flow for the various slip boundary condition models and u_c/u_m are given in Figs. 9–12. Each figure displays the flow parameters used in the numerical model, with all of the hydrodynamically/thermally developing solutions represented by a dashed line, and all of the thermally developing solutions presented with a solid line. For the thermally developing solutions, the flow is hydrodynamically fully developed at the entrance, which results in a constant *Po* through the length of the channel. In general, all of the combined hydrodynamically/thermally developing *Po* and *Nu* are initially larger than the thermally developing *Po* and *Nu*, due to the larger velocities and velocity gradients at the wall. However, as the flows develop, the thermally and the combined hydrodynamically/thermally developing values converge to the fully developed values of *Po* and *Nu* which correspond to the data presented in Figs. 5–8. The effects of $\beta_{V1}Kn$ and β_{T1}/β_{V1} on thermally developing flow have been presented in previous studies [8], and so will not be presented here. However, these results are as would be expected based on the fully developed results. Increasing $\beta_{V1}Kn$, results in decreasing *Po* and *Nu* for both the entrance and the fully developed values, and increasing β_{T1}/β_{V1} results in decreasing *Nu* for both the entrance and fully developed values.

The data in Figs. 9 and 10 demonstrate the effect of the different slip boundary condition models through the thermal and combined hydrodynamic/thermal entrance lengths of *Po* and *Nu*, respectively. Just as in the fully developed case, Deissler boundary conditions generally predict lower *Po* and *Nu* values compared to the first-order model, and Karniadakis and Beskok boundary conditions predict higher *Po* and *Nu* values compared to the first-order model. The differing second-order effects, due to the opposite signs of the second-order coefficients given in Table 1, are even more significant at the channel entrance than for the fully developed values, due to the large first- and second-order velocity and temperature gradients at the channel entrance.

The effects of creep velocity on the thermal and combined hydrodynamic/thermal entrance length *Po* and *Nu* are shown in Figs. 11 and 12, respectively. For these results second-order Deissler boundary conditions are used. As in the fully developed case at $\beta_{V1}Kn = 0.04$, creep velocity in the same direction as the mean velocity reduces *Po* and increases *Nu*, while creep flow opposite to the mean flow increases *Po* and decreases *Nu*, compared to the case where creep flow is not considered. Close examination of Fig. 11 will reveal that the thermally developing *Po* curves that include creep flow are not perfectly horizontal; *Po* with negative creep flow decreases slightly, while *Po* with positive creep flow increases slightly. This is because the creep velocity contribution to the inlet flow is coupled to the thermal development and as such cannot be truly hydrodynamically fully developed until it is also thermally fully developed. At the channel entrance, before the constant axial temperature gradient is established, *Nu* for each of the three thermally developing flows is approximately the same value, and *Nu* for each of the three hydrodynamically/thermally developing flows is approximately the same value. As the axial temperature gradient and resulting creep velocity becomes constant, the *Nu* data that include creep flow diverge from *Nu* with no creep flow and approach the fully developed *Nu* values which are dependent on u_c/u_m.

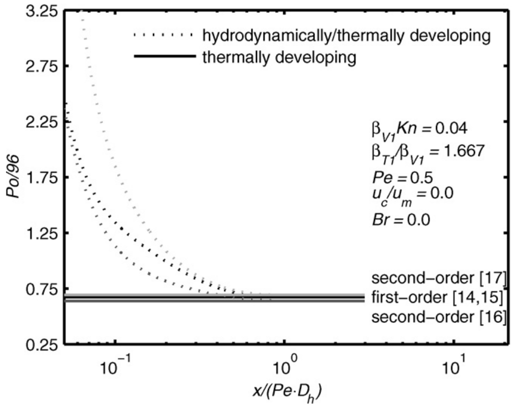

Fig. 9. Effect of slip boundary conditions on entrance *Po*.

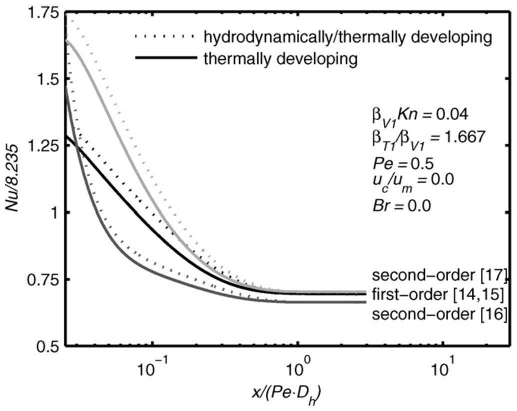

Fig. 10. Effect of slip boundary conditions on entrance *Nu*.

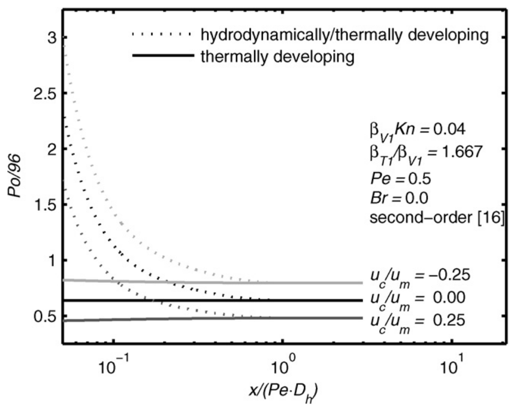

Fig. 11. Effect of creep velocity on entrance *Po*.

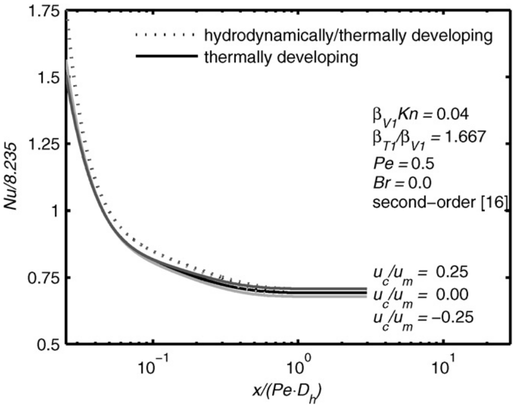

Fig. 12. Effect of creep velocity on entrance *Nu*.

5. Conclusions

The Poiseuille and Nusselt numbers of two-dimensional constant wall heat flux flows in the slip regime have been calculated both analytically and numerically using second-order slip and temperature jump boundary conditions. The analytical equations for *Po* and *Nu* are expressed in terms of the degree of rarefaction (*Kn*); the slip flow model parameters β_{V1}, β_{V2}, β_{T1}, and β_{T2}; the creep flow (u_c/u_m); and the amount of viscous dissipation (*Br*). The analytic solutions are valid for nearly incompressible, steady state, and hydrodynamically/thermally fully developed flows. Numerical solutions for microchannel *Po* and *Nu* are calculated using a continuum based three-dimensional, unsteady, compressible, CFD algorithm modified with slip boundary conditions. For fully developed flows the differences between numerically and analytically computed *Po* and *Nu* are negligible. With the numerical algorithm verified, it is then used to evaluate hydrodynamically/thermally developing *Po* and *Nu*.

Both analytical and numerical data indicate that second-order terms and creep velocity effects are significant within the slip flow regime. This study quantifies the effects of two second-order models [16,17]; however, the analytic solutions may be used for any second-order slip model with boundary conditions of the same general form. This variability is important due to the lack of experimental data and agreement on second-order boundary conditions. The significance of including creep flow in the analytical or numerical analysis of *Po* and *Nu* depends on the magnitude of the heat flux and the degree of rarefaction.

References

[1] R.M. Inman, Laminar slip flow heat transfer in a parallel-plate channel or a round tube with uniform wall heating, NASA TN D-2393 (1964).

[2] T.A. Ameel, X. Wang, R.F. Barron, R.O. Warrington, Laminar forced convection in a circular tube with constant heat flux and slip flow, Microscale Thermophysical Engineering 1 (1997) 303–320.

[3] R.F. Barron, X. Wang, T.A. Ameel, R.O. Warrington, The Graetz problem extended to slip-flow, International Journal of Heat and Mass Transfer 40 (1997) 1817–1823.

[4] F.E. Larrode, C. Housiadas, Y. Drossinos, Slip-flow heat transfer in circular tubes, International Journal of Heat and Mass Transfer 43 (2000) 2669–2680.

[5] G. Tunc, Y. Bayazitoglu, Heat transfer for gaseous flow in microtubes with viscous heating, American Society of Mechanical Engineers, Heat Transfer Division, (Publication) HTD 366 (2000) 299–306.

[6] G. Tunc, Y. Bayazitoglu, Convection at the entrance of micropipes with sudden wall temperature change, American Society of Mechanical Engineers, Heat Transfer Division, (Publication) HTD 372 (2002) 265–270.

[7] X. Chen, B. Xu, The Nusselt number and friction factor at the entrance of a micro-duct, International Communications in Heat and Mass Transfer 29 (2002) 763–772.

[8] S. Yu, Slip flow heat transfer in rectangular microchannels, Ph.D. thesis, University of Utah, USA, 2002.

[9] N.G. Hadjiconstantinou, Convective heat transfer in micro and nano channels: Nusselt number beyond slip flow, American Society of Mechanical Engineers, Heat Transfer Division, (Publication) HTD 366 (2000) 13–22.

[10] N.G. Hadjiconstantinou, O. Simek, Constant-wall-temperature Nusselt number in micro and nano-channels, Journal of Heat Transfer 124 (2002) 356–364.

[11] N.G. Hadjiconstantinou, The effect of viscous heat dissipation on convective heat transfer in small-scale slipping gaseous flows, International Conference on Microchannels and Minichannels 1 (2003) 269–273.

[12] H.P. Kavehpour, M. Faghri, Y. Asako, Effects of compressibility and rarefaction on gaseous flows in microchannels, Numerical Heat Transfer; Part A: Applications 32 (1997) 677–696.

[13] C.S. Chen, W.J. Kuo, Heat transfer characteristics of gaseous flow in long mini- and microtubes, Numerical Heat Transfer; Part A: Applications 46 (2004) 497–514.

[14] J.C. Maxwell, On stresses in rarified gases arising from inequalities of temperature, Philosophical Transactions of the Royal Society, London 170 (1879) 231–256.

[15] M. Smoluchowski, Ueber wärmeleitung in verdünnten gasen, Annalen der Physik und Chemie 64 (1898) 101–130.

[16] R.G. Deissler, An analysis of second-order slip flow and temperature-jump boundary conditions for rarefied gases, International Journal of Heat and Mass Transfer 7 (1964) 681–694.

[17] G.E. Karniadakis, A. Beskok, Micro Flows: Fundamentals and Simulation, Springer-Verlag, New York, 2002.

[18] J. Maurer, P. Tabeling, P. Joseph, H. Willaime, Second-order slip laws in microchannels for helium and nitrogen, Physics of Fluids 15 (2003) 2613–2621.

[19] S. Colin, P. Lalonde, R. Caen, Validation of a second-order slip flow model in rectangular microchannels, Heat Transfer Engineering 25 (2004) 23–30.

[20] R.K. Shah, A.L. London, Laminar Flow Forced Convection in Ducts, Academic Press, New York, 1978.

[21] F. Harlow, A. Amsden, Numerical calculation of almost incompressible flow, Journal of Computational Physics 3 (1968) 80–93.

[22] B. Kashiwa, R. Rauenzahn, A cell-centered ICE method for multiphase flow simulations, Los Alamos National Laboratory Technical Report LA-UR-93-3922 (1994).

[23] J.E. Guilkey, T. Harman, A. Xia, B. Kashiwa, P. McMurtry, An Eulerian-Lagrangian approach for large deformation fluid structure interaction problems, Part 1: Algorithm development, Advances in Fluid Mechanics, Fluid Structure Interaction II 36 (2003) 143–156.

[24] T. Harman, J.E. Guilkey, B. Kashiwa, J. Schmidt, P. McMurtry, An Eulerian-Lagrangian approach for large deformation fluid structure interaction problems, Part 2: Multi-physics simulations within a modern computational framework, Advances in Fluid Mechanics, Fluid Structure Interaction II 36 (2003) 157–166.

[25] S.G. Parker, J. Guilkey, T. Harman, A component-based parallel infrastructure for the simulation of fluid-structure interaction, Engineering with Computers 22 (2006) 277–292.

CHAPTER 4

THE EFFECT OF VISCOUS DISSIPATION AND RAREFACTION ON RECTANGULAR MICROCHANNEL CONVECTIVE HEAT TRANSFER

Available online at www.sciencedirect.com
ScienceDirect
ELSEVIER
International Journal of Thermal Sciences 48 (2009) 271–281
International Journal of Thermal Sciences
www.elsevier.com/locate/ijts

The effect of viscous dissipation and rarefaction on rectangular microchannel convective heat transfer

J. van Rij, T. Ameel *, T. Harman

Department of Mechanical Engineering, University of Utah, Salt Lake City, UT 84112, USA

Received 29 March 2008; received in revised form 25 July 2008; accepted 29 July 2008

Abstract

The effect of viscous dissipation and rarefaction on rectangular microchannel convective heat transfer rates, as given by the Nusselt number, is numerically evaluated subject to constant wall heat flux ($H2$) and constant wall temperature (T) thermal boundary conditions. Numerical results are obtained using a continuum based, three-dimensional, compressible, unsteady computational fluid dynamics algorithm with slip velocity and temperature jump boundary conditions applied to the momentum and energy equations, respectively. For the limiting case of parallel plate channels, analytic solutions for the thermally and hydrodynamically fully developed momentum and energy equations are derived, subject to both first- and second-order slip velocity and temperature jump boundary conditions, from which analytic Nusselt number solutions are then obtained. Excellent agreement between the analytical and numerical results verifies the accuracy of the numerical algorithm, which is then employed to obtain three-dimensional rectangular channel and thermally/hydrodynamically developing Nusselt numbers. Nusselt number data are presented as functions of Knudsen number, Brinkman number, Peclet number, momentum and thermal accommodation coefficients, and aspect ratio. Rarefaction and viscous dissipation effects are shown to significantly affect the convective heat transfer rate in the slip flow regime.

Keywords: Microchannel; Nusselt number; Slip flow; Brinkman number; Viscous dissipation

1. Introduction

Many technological advances in computation speed, power supply requirements, diagnostics, and control issues are contingent on the reduction of thermal fluid systems to the microscale. However, as thermal fluid system sizes are reduced to the microscale, effects that are negligible at a macroscale may become significant, and thus change the predicted behavior of these systems. For gaseous flows, some of these effects include rarefaction, viscous dissipation, compressibility, and axial conduction, which may be characterized by the Knudsen number, *Kn*, Brinkman number, *Br*, Mach number, *Ma*, and Peclet number, *Pe*, respectively. Fundamental to the design of many thermal fluid systems is the accurate evaluation of convective heat transfer rates, typically presented in the form of the Nusselt number, *Nu*. Although, the assessment of gaseous microchannel *Nu*, subject to effects of *Kn*, *Br*, *Ma*, and *Pe*, has been an active area of research, there are currently no experimentally determined values of local convective heat transfer rates, due to measurement and accuracy limitations at the microscale, and rarified microchannel *Nu* data must generally be acquired analytically or numerically.

The most common means of analytically or numerically modeling a rarified flow within the slip regime, $0.01 \leqslant Kn \leqslant 0.1$, is through the use of slip velocity and temperature jump boundary conditions applied to the conventional continuum momentum and energy equations. The original slip velocity boundary condition, given in Eq. (1), and temperature jump boundary condition, given in Eq. (2), were derived by Maxwell [1] and Smoluchowski [2], respectively.

$$u|_{y=0} - u_w = \left[\left(\frac{2-\sigma_v}{\sigma_v}\right)\frac{\lambda}{\mu}\tau + \frac{3}{4}\frac{\mu R}{P}\frac{\partial T}{\partial x}\right]_{y=0} \tag{1}$$

$$T|_{y=0} - T_w = \left[\left(\frac{2-\sigma_t}{\sigma_t}\right)\left(\frac{2\gamma}{1+\gamma}\right)\frac{\lambda}{Pr}\frac{\partial T}{\partial y}\right]_{y=0} \tag{2}$$

---

* Corresponding author. Tel.: +1 801 585 9730; fax: +1 801 585 9826.
E-mail address: ameel@mech.utah.edu (T. Ameel).

1290-0729/$ – see front matter © 2008 Elsevier Masson SAS. All rights reserved.
doi:10.1016/j.ijthermalsci.2008.07.010

Nomenclature

AR	aspect ratio, b/h	
b	channel width	m
Br	Brinkman number, $Br_{H2} = \mu u_m^2/(q_w D_h)$, $Br_T = \mu u_m^2/(k(T_i - T_w))$	
c_p	specific heat at constant pressure	$\mathrm{J\,kg^{-1}\,K^{-1}}$
c_v	specific heat at constant volume	$\mathrm{J\,kg^{-1}\,K^{-1}}$
D_h	hydraulic diameter, $2bh/(b+h)$	m
e	internal energy per unit mass	$\mathrm{J\,kg^{-1}}$
h	channel height	m
k	thermal conductivity	$\mathrm{W\,m^{-1}\,K^{-1}}$
Kn	Knudsen number, λ/D_h	
L	channel length	m
Ma	Mach number, $(Kn\,Pe/Pr)\sqrt{2/(\pi\gamma)}$	
Nu	Nusselt number, $q_{w,m}D_h/(k(T_w - T_m))$	
P	pressure	Pa
Pe	Peclet number, $Pr\,Re$	
Pr	Prandtl number, $c_p\mu/k$	
q	heat flux	$\mathrm{W\,m^{-2}}$
R	gas constant	$\mathrm{J\,kg^{-1}\,K^{-1}}$
Re	Reynolds number, $\rho u_m D_h/\mu$	
T	temperature	K
t	time	s
u	velocity in x-direction	$\mathrm{m\,s^{-1}}$
v	velocity in y-direction	$\mathrm{m\,s^{-1}}$
$\mathbf{v}$	velocity vector	$\mathrm{m\,s^{-1}}$
x, y, z	Cartesian coordinates	m

Greek symbols

β	gas–wall interaction parameter, β_{t1}/β_{v1}	
β_{t1}	first-order temperature jump coefficient, $((2-\sigma_t)/\sigma_t)(2\gamma/(1+\gamma))(1/Pr)$	
β_{t2}	second-order temperature jump coefficient	
β_{v1}	first-order velocity slip coefficient, $(2-\sigma_v)/\sigma_v$	
$\beta_{v1}Kn$	rarefaction parameter	
β_{v2}	second-order velocity slip coefficient	
γ	ratio of specific heats, c_p/c_v	
λ	molecular mean free path, $\mu/(\rho\sqrt{2RT/\pi})$	m
μ	dynamic viscosity	$\mathrm{kg\,m^{-1}\,s^{-1}}$
ρ	density	$\mathrm{kg\,m^{-3}}$
σ_t	thermal accommodation coefficient	
σ_v	momentum accommodation coefficient	
$\boldsymbol{\tau}$	shear stress	Pa
Φ	viscous dissipation term, $\nabla\cdot(v\cdot\tau) - v\cdot(\nabla\cdot\tau)$	$\mathrm{J\,m^{-3}\,s^{-1}}$

Subscripts

$H2$	constant wall heat flux condition
i	inlet value
m	mean value
o	outlet value
T	constant wall temperature condition
w	wall value
∞	fully developed value

Superscripts

0	initial value

The first term in Eq. (1) is the velocity slip due to the shear stress at the wall, and the second term is the thermal creep velocity due to a temperature gradient tangential to the wall. Eqs. (1) and (2), as well as subsequent equations, are presented in a format assuming a Cartesian coordinate system, a wall normal direction (y), and a streamwise direction (x) (see Fig. 1). To reduce the number of variables involved, the nondimensional parameters β_{v1}, β_{t1}, $\beta_{v1}Kn$, and β, as defined in the nomenclature, are used hereafter, rather than the coefficients of Eqs. (1) and (2). $\beta_{v1}Kn$ is representative of the level of rarefaction, where $\beta_{v1}Kn = 0$, corresponds to continuum conditions, and $\beta_{v1}Kn \approx 0.10$, corresponds to the approximate upper limit of the slip regime. β is representative of the gas–wall interactions, where $\beta = 0$ corresponds to the artificial condition of zero temperature jump with nonzero slip velocity, $\beta \approx 1.667$ corresponds to typical values for air ($\gamma = 1.4$, $Pr = 0.7$) when $\sigma_v = \sigma_t = 1$, and β values as high as 100 are possible (depending on the relative magnitudes of γ, Pr, σ_v and σ_t, where values of σ_v and σ_t must be measured experimentally, and are presented for several common fluid-surface interactions in [3]).

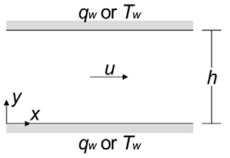

Fig. 1. Two-dimensional channel configuration.

In addition to the first-order slip model given by Eqs. (1) and (2), numerous second-order models and modifications have been proposed to improve the accuracy and range of applicability of the slip flow representation of rarefaction into the lower transition regime [3]. These second-order boundary condition models are often compared for two-dimensional, planar, constant property flow, without creep flow. For this configuration, many second-order models may be written in the format of Eqs. (3) and (4), where values of β_{v2} and β_{t2} depend on the second-order model.

$$u|_{y=0} - u_w = \left[\beta_{v1}\lambda\frac{\partial u}{\partial y} - \beta_{v2}\lambda^2\frac{\partial^2 u}{\partial y^2}\right]_{y=0} \tag{3}$$

$$T|_{y=0} - T_w = \left[\beta_{t1}\lambda\frac{\partial T}{\partial y} - \beta_{t2}\lambda^2\frac{\partial^2 T}{\partial y^2}\right]_{y=0} \tag{4}$$

Currently, there is insufficient experimental data to establish the use of any particular second-order model over another.

Nonetheless, several evaluations have shown second-order boundary conditions to be useful with respect to evaluating microchannel mass flow rates [4,5], and as such, theoretical convective heat transfer solutions with second-order terms may prove valuable as additional experimental and theoretical results become available.

Viscous dissipation effects in macroscale systems are typically only significant for high velocity or highly viscous flows. In microscale systems, however, large channel length to hydraulic diameter ratios result in large velocity and pressure gradients, and consequently thermal energy generation due to viscous dissipation. A slight increase in fluid temperature may be significant relative to the small temperature gradients typically present in microchannels, and as a result alter the convective heat transfer rate and any temperature dependent fluid properties. Because the function of many microfluidic systems is cooling, viscous dissipation becomes a limiting factor that must be accurately represented. Recently, several theoretical studies have focused specifically on the effects of viscous dissipation in the slip flow regime [6–11]. All of these studies are for parallel plate flow, except for [7], which examines the effect of viscous dissipation for rectangular microchannels and the $H1$ thermal boundary condition. Also, nearly all of these previous studies evaluated the effect of viscous dissipation without also considering the related flow work and shear work effects, which for a rarified gas flow are of the same order of magnitude as viscous dissipation [6,12,13].

The significance of both compressibility and streamwise conduction effects may be established by the magnitude of Pe, which is directly related to Ma for a given $Kn, Ma = (Kn\,Pe/Pr)\sqrt{2/(\pi\gamma)}$. Pe represents the ratio of thermal energy convected to the fluid to thermal energy axially conducted within the fluid. A low Pe, corresponding to a low Ma, which is common in micro flows, and generally indicates that compressibility effects are less significant while streamwise conduction effects are nonnegligible. Prior studies indicate that axial conduction effects at low Pe result in an increase in Nu for constant wall temperature thermal boundary conditions [13,14]. Numerical studies which have examined the effects of compressibility in microchannels found that, although compressible flow never reaches a fully developed state, compressible flow at low Mach numbers, 'nearly incompressible flow,' may reach a 'locally fully developed' state, for which the local values of wall friction and heat transfer are approximately equivalent to incompressible values [15,16].

The objective of this study is to numerically evaluate the effects of rarefaction and viscous dissipation for nearly incompressible, rectangular microchannel convective heat transfer rates in the slip flow regime, subject to constant wall heat flux ($H2$) and constant wall temperature (T) thermal boundary conditions [13]. Numerical results are obtained using a three-dimensional, compressible, unsteady computational fluid dynamics algorithm. Continuum based conservation equations, constitutive models (Newtonian–Fourier), and equation-of-state model (ideal gas), with slip velocity and temperature jump boundary conditions are utilized, based on the assumption that these approximations are reasonably accurate within the slip flow regime. To verify the numerical results, analytic solutions for thermally and hydrodynamically fully developed parallel plate constant wall heat flux and constant wall temperature Nusselt numbers are derived as a function of rarefaction ($\beta_{v1}Kn$), viscous dissipation (Br), gas–wall interactions (β), and second-order velocity slip and temperature jump terms (β_{v1}, β_{t2}). Second-order terms are retained in this analytic analysis to provide a possible basis of comparison for future experimental results, beyond this however, the effect of second-order terms is not investigated in this study. Following the algorithm verification, three-dimensional rectangular microchannel and thermally/hydrodynamically developing Nusselt number data are numerically evaluated and presented as functions of $\beta_{v1}Kn, \beta, Br, Pe$, and aspect ratio, AR. Viscous dissipation effects are examined in conjunction with flow work effects, which previous studies have neglected. Compressibility, axial conduction, and creep flow effects are not directly considered in this study, however, due to the low Ma (low Pe) utilized to achieve nearly incompressible flow, axial conduction effects will be evident in the constant wall temperature Nu results.

2. Analytic solutions

The flow configuration that is analytically evaluated is a two-dimensional parallel-plate microchannel of separation distance h, as illustrated in Fig. 1. To obtain analytic solutions, the following simplifying assumptions are applied: two-dimensional, steady state, incompressible, thermally and hydrodynamically fully developed, Newtonian, ideal gas, constant properties, laminar flow, and either symmetrically constant wall heat flux or constant wall temperature. With these simplifications the momentum equation is given in Eq. (5) and the energy equation, in terms of temperature, with viscous dissipation, $\mu(\partial u/\partial y)^2$, and flow work, $u\,\partial P/\partial x$, terms is given in Eq. (6).

$$\mu\frac{\partial^2 u}{\partial y^2} = \frac{dP}{dx} \tag{5}$$

$$k\frac{\partial^2 T}{\partial y^2} = u\rho c_p\frac{\partial T}{\partial x} - u\frac{\partial P}{\partial x} - \mu\left(\frac{\partial u}{\partial y}\right)^2 \tag{6}$$

With symmetry applied at the microchannel midplane, and the general second-order slip velocity boundary condition, Eq. (3), applied at the wall, the momentum equation, Eq. (5), may be integrated twice to obtain the nondimensional velocity profile given in Eq. (7), in terms of the slip velocity to mean velocity ratio, u_s/u_m, Eq. (8).

$$\frac{u(y/h)}{u_m} = \frac{u_s}{u_m} + 6\left(1 - \frac{u_s}{u_m}\right)\left(\frac{y}{h} - \frac{y^2}{h^2}\right) \tag{7}$$

$$\frac{u_s}{u_m} = 1 - \frac{1}{1 + 12\beta_{v1}Kn + 48\beta_{v2}Kn^2} \tag{8}$$

The velocity profile, Eq. (7), is then substituted into the energy equation, Eq. (6). For the fully developed constant wall heat flux case both the pressure and temperature gradients in the x-direction are constants, and for the fully developed constant wall temperature case the pressure gradient in the x-direction is constant, and the temperature gradient in the x-direction approaches zero. In either case, the energy equation, Eq. (6), may be integrated twice by applying the general second-order temperature jump boundary condition, Eq. (4), at the wall and symmetry at the midplane. The resulting nondimensional temperature profile for constant wall heat flux is given in Eq. (9), with the ensuing Nu_{H2} given in Eq. (10), and the constant wall temperature nondimensional temperature profile is given in Eq. (11), with the subsequent Nu_T given in Eq. (12).

$$\begin{aligned}\frac{T(y/h)-T_w}{q_w D_h/k} = {} & -\frac{1}{2}\left(\frac{y}{h}-\frac{y^2}{h^2}\right) \\ & \times\left\{1+\left[1+12Br_{H2}\left(3-\frac{u_s}{u_m}\right)\left(1-\frac{u_s}{u_m}\right)\right]\right. \\ & \left.\times\left(1-\frac{u_s}{u_m}\right)\left(\frac{y}{h}-\frac{y^2}{h^2}\right)\right\} \\ & -\beta_{t1}Kn-4\beta_{t2}Kn^2\left[\frac{u_s}{u_m}\right. \\ & \left.-12Br_{H2}\left(3-\frac{u_s}{u_m}\right)\left(1-\frac{u_s}{u_m}\right)^2\right] \end{aligned} \tag{9}$$

$$\begin{aligned} Nu_{H2} = {} & 420\left[51+420\beta_{t1}Kn-2\frac{u_s}{u_m}\left(9-\frac{u_s}{u_m}-840\beta_{t2}Kn^2\right)\right. \\ & +12Br_{H2}\left(3-\frac{u_s}{u_m}\right)\left(1-\frac{u_s}{u_m}\right)^2 \\ & \left.\times\left(9-2\frac{u_s}{u_m}-1680\beta_{t2}Kn^2\right)\right]^{-1} \end{aligned} \tag{10}$$

$$\begin{aligned}\frac{T(y/h)-T_w}{T_i-T_w} = {} & -6Br_T\left(1-\frac{u_s}{u_m}\right)\left[3\left(1-\frac{y}{h}\right)^2\frac{y^2}{h^2}\right. \\ & -24\beta_{t2}Kn^2 \\ & +\frac{u_s}{u_m}\left\{\left(\frac{y}{h}-\frac{y^2}{h^2}\right)\left[1-3\left(\frac{y}{h}-\frac{y^2}{h^2}\right)\right]\right. \\ & \left.\left.+2\beta_{t1}Kn+32\beta_{t2}Kn^2\right\}\right] \end{aligned} \tag{11}$$

$$\begin{aligned} Nu_T = {} & 420\frac{u_s}{u_m}\left[27-5040\beta_{t2}Kn^2\right. \\ & \left.+\left(9+420\beta_{t1}Kn+6720\beta_{t2}Kn^2\right)\frac{u_s}{u_m}-\frac{u_s^2}{u_m^2}\right]^{-1} \end{aligned} \tag{12}$$

Nu_{H2}, Eq. (10) and Nu_T, Eq. (12), with u_s/u_m defined in Eq. (8), represent the energy exchange of constant wall heat flux and constant wall temperature, thermally and hydrodynamically fully developed parallel plate microchannel flows. These interactions are a result of the combined effects of rarefaction (*Kn*), the slip flow model parameters (β_{v1}, β_{v2}, β_{t1}, and β_{t2}), and viscous dissipation, flow work, and shear work (*Br*). Viscous dissipation acts as a distributed heat source, with the majority of the thermal energy generated near the wall, due to the larger velocity gradients. Flow work acts as a distributed heat sink, with the majority of the thermal energy absorbed near the center of the flow, due to the larger velocity magnitudes. And, shear work, $u\,\partial\tau/\partial y|_{y=0}$, acts as a heat source at the wall, due to the thermal energy generated by the slipping flow. For fully developed, continuum flow there is no shear work at the wall, and the thermal energy generated by viscous dissipation is exactly equal to the thermal energy absorbed by flow work, regardless of the magnitude of *Br*, as discussed in [12] and [13]. Within the slip flow regime, the thermal energy generated by viscous dissipation and shear work is exactly equal to the thermal energy absorbed by flow work, again regardless of the magnitude of *Br*, as discussed in [6].

For continuum flow ($Kn = 0$), with negligible viscous dissipation ($Br_{H2} = 0$), Nu_{H2}, Eq. (10), reduces to the conventional value of 8.235. For continuum flow with viscous dissipation, Nu_{H2} reduces to the equation given by [13] for two-dimensional flow with viscous dissipation. For slip flow with first-order terms only ($\beta_{v2} = \beta_{t2} = 0$) and no viscous dissipation, Nu_{H2} reduces to the equation originally derived by Inman [17] (with $Kn = \lambda/h$, rather than $Kn = \lambda/D_h$ used here). When both viscous dissipation and flow work are considered in the continuum flow regime, the energy added by viscous dissipation is equal to the energy absorbed by flow work and, as a result, the fully developed mean temperature is not a function of Br_{H2}. The temperature distribution and wall temperature, however, do vary with Br_{H2}, and as such, Nu_{H2} is a function of Br_{H2}. If the flow work contribution to the energy exchange, $u\,\partial P/\partial x$, is neglected in the previous analysis, both the wall temperature and the mean temperature are shifted by equal amounts [12] (from their values when both viscous dissipation and flow work are considered), and as a result the nondimensional temperature distribution and Nu_{H2} remain the same as given in Eqs. (9) and (10).

For continuum flow, Nu_T, Eq. (12), reduces to zero, which is consistent with results presented in [12] and [13]. $Nu_T = 0$ is notably different from 7.54, the typical Nu_T value reported for constant wall temperature parallel plate flow without axial conduction effects. This is, again, a result of the competing effects of viscous dissipation and flow work, which result in $\partial T_m/\partial x = 0$, $\partial T/\partial y|_{y=0} = 0$, and consequently $Nu_T = 0$, regardless of the magnitude of Br_T or *Pe*. The temperature profile, however, is not uniform, and for $Br_T \neq 0$ the fully developed mean temperature, T_m, is always less than the wall temperature, T_w, by an amount dependent on the magnitude of Br_T. If the flow work term, $u\,\partial P/\partial x$, is neglected in the preceding derivation, T_m is always greater than T_w by an amount dependent on the magnitude of Br_T, and the resulting Nu_T is given by Eq. (13).

$$Nu_T = 140\left(8+140\beta_{t1}Kn+1680\beta_{t2}Kn^2-\frac{u_s}{u_m}\right)^{-1} \tag{13}$$

For continuum flow, Eq. (13) reduces to 17.5, which is consistent with results presented in [8,9,11]. However, rarified flows are generally gaseous, and flow work in gaseous flows is of the same order of magnitude as viscous dissipation. For this reason, it is expected that Eq. (12) is a more accurate representation of the energy exchange in the slip flow regime than Eq. (13).

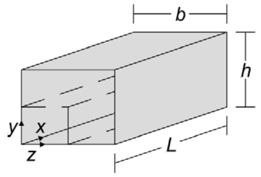

Fig. 2. Rectangular channel configuration.

3. Numerical model

The computational fluid dynamics (CFD) algorithm used for this study has been described and verified for previous microchannel investigations [18–21]. The algorithm is a finite volume, multi-material CFD code based on the ICE (Implicit, Continuous-fluid, Eulerian) method. The ICE implementation used in this study is well developed and documented [22–24]. The code is three-dimensional, fully compressible, unsteady, and capable of modeling variable fluid properties, fluid-structure interactions, and chemical reactions. To accurately model microchannel flows, the algorithm has been modified to selectively model first- or second-order slip boundary conditions, creep flow, and viscous dissipation. The implementation of these modifications is consistent with the original code in being numerically second-order accurate both spatially and temporally.

3.1. Model parameters and criteria

The flow configuration that is numerically analyzed is illustrated in Fig. 2, and is modeled assuming laminar flow of a Newtonian, ideal gas, with constant properties of air ($\gamma = 1.4$, $Pr = 0.7$), and a uniformly spaced computational grid. For this flow, the governing mass, momentum, and energy equations that are numerically solved are given in Eqs. (14), (15), and (16) respectively.

$$\frac{\partial \rho}{\partial t} + \nabla \cdot (\rho \mathbf{v}) = 0 \tag{14}$$

$$\frac{\partial (\rho \mathbf{v})}{\partial t} + \nabla \cdot (\rho \mathbf{v}\mathbf{v}) = -\nabla P + \nabla \cdot \boldsymbol{\tau} \tag{15}$$

$$\frac{\partial (\rho e)}{\partial t} + \nabla \cdot (\rho \mathbf{v} e) = -P(\nabla \cdot \mathbf{v}) + \nabla \cdot (k \nabla T) + \Phi \tag{16}$$

To decrease the computational time required to reach a solution, only one quarter of the symmetric microchannel is modeled. (For parallel plate flows, the model is two-dimensional, and one half of the microchannel is modeled.) Two types of problems are numerically evaluated, thermally developing flows and thermally/hydrodynamically developing flows. For both cases the outlet pressure, along with either the inlet pressure or the inlet velocity, are specified to obtain a given flow *Pe*, *Br* and *Kn*. At the channel wall, either a uniform heat flux or a constant wall temperature is specified. For thermally developing flows a inlet pressure and a uniform inlet temperature are specified while the outlet temperature and the inlet and outlet velocities are allowed to evolve to their fully developed profiles. For combined thermally/hydrodynamically developing flows both a uniform inlet temperature and a uniform inlet velocity are specified while the outlet temperature and velocity are allowed to evolve to their fully developed profiles. An example of the required numerical parameters, and the resulting nondimensional parameters, is given in Table 1 for one set of conditions – a thermally/hydrodynamically developing, constant wall temperature flow.

For the numerical results to be comparable to the analytic solutions, the flow must be locally fully developed, steady state, nearly incompressible, and have constant properties. Given these stipulations, the flow *Pe* and wall heat flux, or wall temperature, are specified such that the total density change within the flow is less than a few percent, and the *Ma* is generally less than approximately 0.05. For the low *Pe* values used in this study, channel lengths of 4*h* for parallel plate channels, and 6*h* for rectangular channels, were found to be sufficient for the flow to develop while avoiding significant compressibility effects due to a longer channel. Because the algorithm is unsteady, flow properties must evolve from a set of initial conditions to steady state conditions subject to the boundary conditions. For all of the data presented, the initial velocity field is zero and the

Table 1
Example computational and nondimensional problem specification for a thermally/hydrodynamically developing, constant wall temperature flow

Computational problem specification		
Inlet boundary	Outlet boundary	Wall boundary
$\partial P/\partial x\|_{x=0} = 0.0$ (Pa m^{-1})	$P_o = 82745.4329$ (Pa)	$\partial P/\partial y\|_{y=0} = 0.0$ (Pa m^{-1})
$\partial \rho/\partial x\|_{x=0} = 0.0$ (kg m^{-4})	$\partial \rho/\partial x\|_{x=L} = 0.0$ (kg m^{-4})	$\partial \rho/\partial y\|_{y=0} = 0.0$ (kg m^{-4})
$T_i = 300.155907$ (K)	$\partial T/\partial x\|_{x=L} = 0.0$ (K m^{-1})	$T\|_{y=0} = T_w + \beta_{t1}\lambda \partial T/\partial y\|_{y=0}$ (K)
		$T_w = 300$ (K), $\sigma_t = 1.0$
$u_i = 6.68919094$ (m s^{-1})	$\partial u/\partial x\|_{x=L} = 0.0$ (m s^{-1})	$u\|_{y=0} = u_w + \beta_{v1}(\lambda/\mu)\tau\|_{y=0}$ (m s^{-1})
		$u_w = 0.0$ (m s^{-1}), $\sigma_v = 1.0$
Initial conditions	Grid parameters	Fluid properties
$\rho^0 = 0.96103871$ (kg m^{-3})	$b = \infty$ (m) (*symmetry)*	$c_v = 717.5$ (J kg^{-1} K^{-1})
$T^0 = 300.155907$ (K)	$h/2 = 0.5 \cdot 10^{-6}$ (m)	$k = 0.02583$ (W m^{-1} K^{-1})
$u^0 = 0.0$ (m s^{-1})	$L = 4.0 \cdot 10^{-6}$ (m)	$\gamma = 1.4$
	$\Delta x = \Delta y = (h/2)/40$ (m)	$\mu = 1.8 \cdot 10^{-5}$ (kg m^{-1} s^{-1})
Nondimensional problem specification		
$AR = \infty$, $\beta_{v1} Kn = 0.04$, $\beta = 1.667$, $Pe = 0.5$, $Br_T = 0.2$		

initial temperature field is equal to the inlet temperature. The magnitude and number of time steps required to reach steady state are dependent on the grid resolution, *Kn*, and *Pe*. The convergence criteria for each time step is a mass flux residual less than 10^{-9} for each control volume. The criterion used to establish that the flow is steady state is $|(u^{n+1} - u^{n})/u^{n+1}| \leqslant 10^{-10}$ and $|(T^{n+1} - T^{n})/T^{n+1}| \leqslant 10^{-10}$, for each control volume, where n is the number of the time step.

3.2. Model verification and grid resolution

The algorithm's ability to model the effects of the first- and second-order slip boundary conditions and creep flow, for two-dimensional constant wall heat flux flows was demonstrated in [18]. To establish that the algorithm also accurately models the effects of viscous dissipation, numerically and analytically computed nondimensional temperature profiles are compared in Fig. 3, for several representative cases. The numerically computed values, presented as symbols, are the result of thermally developing parallel plate flow at $x = 3.75h$ and $Pe = 0.5$. The analytically computed values, Eq. (9) in Fig. 3(a), and Eq. (11) in Fig. 3(b), are presented as lines. Based on this comparison, the differences between the analytically and numerically computed temperature profiles are negligible, thereby verifying the ability of the algorithm to model viscous dissipation effects.

To verify that the algorithm is capable of modeling convective heat transfer in rectangular microchannels, and to determine the grid resolution required to do so, grid resolution studies for fully developed, continuum flow Nu_{H2} and Nu_T are presented in Table 2. These data are obtained for $Pe = 0.5$, without viscous dissipation effects. The numerical Nu_{H2} are compared to the analytically determined values given by [13]. At $Pe = 0.5$ axial conduction effects in Nu_T are nonnegligible and analytic solutions are unavailable; Nu_T data are instead compared to the correlation values given by [14], which are reported to include axial conduction effects and to be within 8% of accurate. The data in Table 2 indicate that the numerical algorithm converges with approximately second-order numerical accuracy, and that at the highest grid resolution Nu_{H2} are within 0.1% of analytic solutions, and Nu_T are within 2.2% of correlation values. This indicates that the finest grid resolution for each *AR* is sufficiently accurate and, consequently, all of the following numerical results are obtain at this resolution (equivalently, for $AR = \infty$ the grid is $320 \times 40 \times 1$).

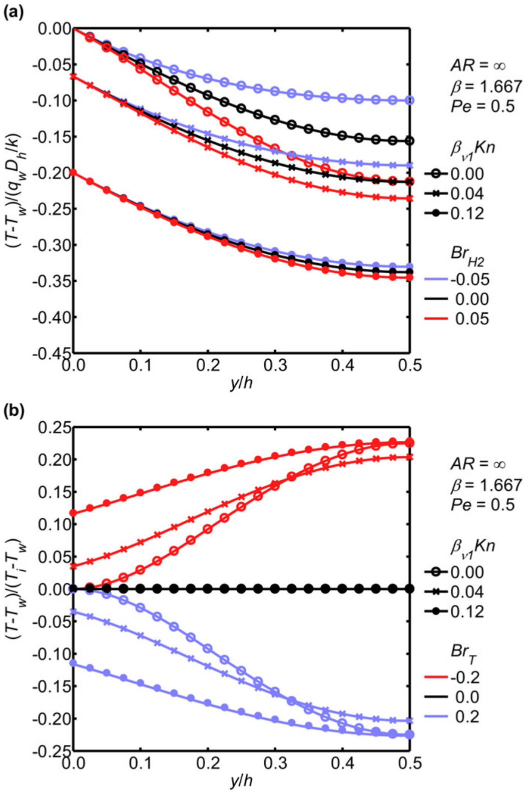

Fig. 3. Comparison of analytical and numerical temperature profiles: (a) constant wall heat flux, Eq. (9), (b) constant wall temperature, Eq. (11).

Table 2
Grid resolution and numerical accuracy study, $Kn = 0$, $Pe = 0.5$, $Br = 0$

	Grid	Nu_{H2}, present	Nu_{H2}, [13]	Nu_T, present	Nu_T, [14]
$AR = 1$	$120 \times 10 \times 10$	3.175	3.09	3.404	3.293
	$240 \times 20 \times 20$	3.108		3.372	
	$480 \times 40 \times 40$	3.092		3.364	
$AR = 2$	$120 \times 10 \times 20$	3.070	3.02	3.853	3.849
	$240 \times 20 \times 40$	3.031		3.835	
	$480 \times 40 \times 80$	3.022		3.831	
$AR = 5$	$120 \times 10 \times 50$	2.964	2.93	5.455	5.405
	$240 \times 20 \times 100$	2.936		5.447	
	$480 \times 40 \times 200$	2.929		5.445	

4. Results and discussion

4.1. Locally fully developed Nu

Locally fully developed values of Nu_{H2} and Nu_T are presented in Fig. 4 for the specified *AR*, $\beta_{v1}Kn$, β, *Br*, and *Pe* values. Nu_{H2} and Nu_T for $AR = \infty$, 5, 2, and 1 are given in Figs. 4(a), 4(b), 4(c), and 4(d), respectively, and although each data set exhibits similar trends in $\beta_{v1}Kn$, β, and *Br*, the effect of *AR* is significant, and the scaling of each plot should be noted. For these data, first-order slip boundary conditions, without creep flow, are used. Numerically computed values are given by symbols, with the connecting lines representing the data trend; except in the case of parallel plate flow, $AR = \infty$, for which the lines are the previous derived analytic *Nu* solutions, Eqs. (10), (12), and (13). For $AR = \infty$, Fig. 4(a), the average difference between the analytic and numeric Nu_{H2} is 0.35%, and the maximum is 1.43%. The average difference between the analytic and numeric Nu_T is 0.28%, and the maximum in 1.03%. Also, in Fig. 4(a), Nu_T derived with viscous dissipation effects, but

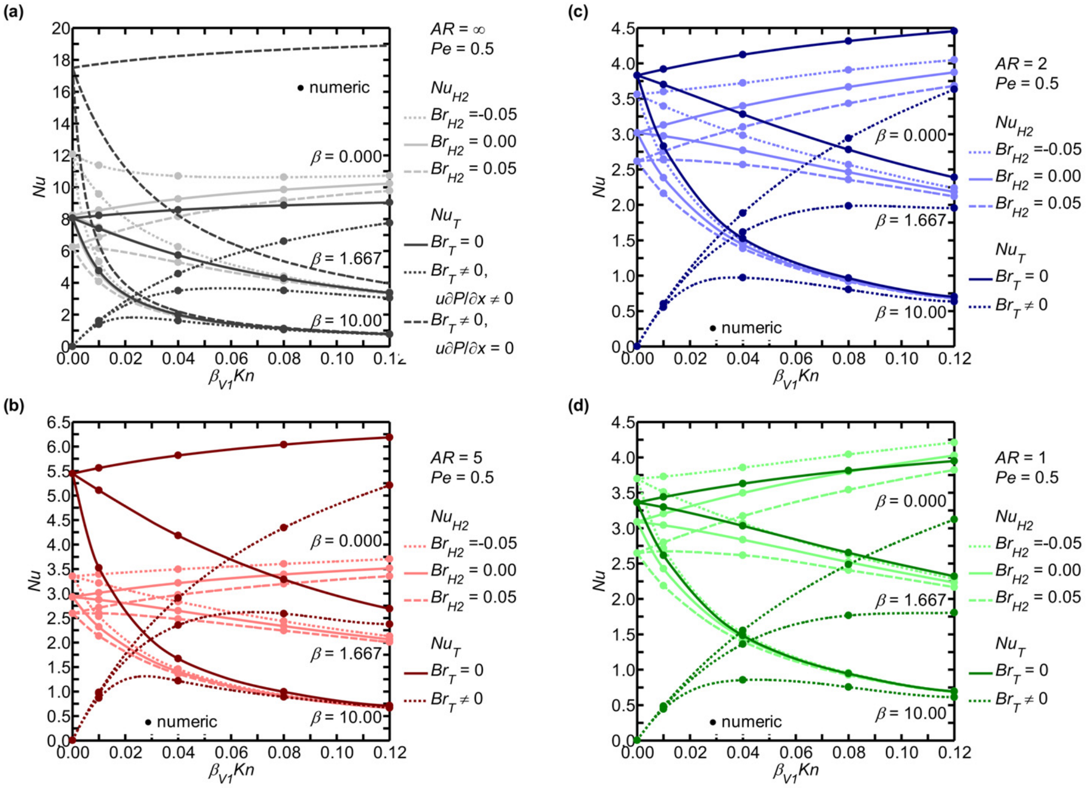

Fig. 4. Effect of viscous dissipation and rarefaction on fully developed Nu_{H2} and Nu_T: (a) $AR = \infty$, (b) $AR = 5$, (c) $AR = 2$, (d) $AR = 1$.

without flow work effects, Eq. (13), serves as a comparison to Nu_T given by Eq. (12), which includes both viscous dissipation and flow work effects and is assumed to be the more accurate representation of the thermal energy exchange in constant wall temperature rarified flows.

The Nu_{H2} and Nu_T data in Fig. 4 without viscous dissipation effects, $Br = 0$, demonstrate that as rarefaction, $\beta_{v1}Kn$, increases, Nu may increase or decrease, depending on β. Increasing rarefaction increases the slip velocity, which increases the energy exchange near the wall and tends to increase Nu, as displayed when $\beta = 0$, for all AR. However, for $\beta \neq 0$, an increase in rarefaction also increases the temperature jump at the wall. An increase in the temperature jump reduces the energy exchange, increases the mean temperature difference $|T_w - T_m|$, and tends to decrease Nu, particularly for large β. These trends are consistent with previously reported slip flow Nu data, without viscous dissipation effects [25].

The Nu_{H2} data in Fig. 4 with viscous dissipation effects, $Br \neq 0$, indicate that for all AR and $\beta_{v1}Kn$ values investigated, positive Br_{H2}, heating, decreases Nu_{H2}, and negative Br_{H2}, cooling, increases Nu_{H2}. As discussed previously, viscous dissipation generates thermal energy predominantly near the wall. This results in an increase in the fluid temperature at the wall, which for heating, increases the difference between the mixed mean fluid temperature and the average wall temperature, thereby reducing Nu_{H2}; while for cooling, this decreases the difference between the mixed mean fluid temperature and the average wall temperature, thereby increasing Nu_{H2} (see Fig. 3(a)). The data in Fig. 4 also indicate that viscous dissipation effects are reduced for increasing $\beta_{v1}Kn$. For $AR = \infty$ and $\beta_{v1}Kn = 0.00$, a Br_{H2} of ± 0.05 will produce a 24.1% decrease in Nu_{H2} for heating, and a 46.6% increase in Nu_{H2} for cooling, while at $\beta_{v1}Kn = 0.12$ ($\beta = 1.667$) the same Br_{H2} results in a 1.5% decrease in Nu_{H2} for heating, and a 1.5% increase in Nu_{H2} for cooling. This reduced effect of Br_{H2} on Nu_{H2} with increasing $\beta_{v1}Kn$ is due to the reduced velocity gradients caused by increasing slip at the wall. Although trends in Nu_{H2} due to viscous dissipation and rarefaction are the same for all AR investigated, these effects are more significant for $AR = \infty$ than for $AR = 1$, 2, and 5. This is because the parallel plate channel has larger velocity gradients, resulting in increased viscous dissipation, and with no side wall heat flux contribution, the thermal energy generated by viscous dissipation is relatively more significant.

The Nu_T data presented in Fig. 4 with viscous dissipation effects, $Br_T \neq 0$ were obtained for $Pe = 0.5$ and $Br_T = -0.2$;

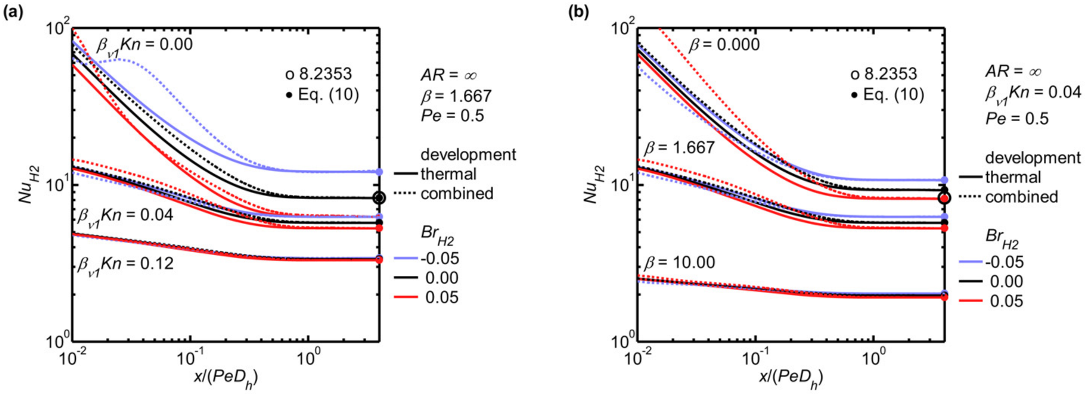

Fig. 5. Thermally and hydrodynamically developing Nu_{H2}: (a) effect of $\beta_{v1}Kn$ and Br_{H2}, (b) effect of β and Br_{H2}.

however, for a given $\beta_{v1}Kn$, β, AR, and slip boundary condition model, all flows with viscous dissipation and flow work result in the same fully developed value of Nu_T, regardless of the magnitude of Pe or Br_T. As discussed previously, for continuum flow, the thermal energy generated by viscous dissipation, predominantly near the walls due to the larger velocity gradients, is equal to the thermal energy absorbed by flow work, predominantly near the center of the flow due to the larger velocity magnitudes. This energy balance results in $\partial T_m/\partial x = 0$, a net wall heat flux of zero, and therefore $Nu_T = 0$ for the constant wall temperature boundary condition. Within the slip flow regime, the slip flow at the wall reduces both the average cross sectional velocity gradients and the maximum core velocity. Although this results in a decrease in both the thermal energy generated by viscous dissipation, and the thermal energy absorbed by flow work, the decrease in viscous dissipation is more significant. The difference, however, is exactly equal to the thermal energy generated by shear work at the wall due to the slipping flow – meaning that, viscous dissipation, flow work, and shear work are still balanced energy sources and sinks, i.e. $\partial T_m/\partial x = 0$, regardless of the magnitude of Br_T or Pe [6]. However, the shear work at the wall creates a nonzero wall heat flux and therefore a nonzero Nu_T. The shear work, $u\partial\tau/\partial y|_{y=0}$, is a function of both the slip velocity and the wall normal velocity gradients. As $\beta_{v1}Kn$ increases, the slip velocity increases, and for the lower slip flow regime this increases the shear work and therefore increases Nu_T. However, as the slip velocity increases the velocity gradients throughout the flow decrease, and for the upper end of the slip regime this leads to a decrease in the shear work (for $AR = \infty$, the point of maximum shear work is $\beta_{v1}Kn = 0.083$). These effects, combined with the effect of AR and temperature jump ($\beta \neq 0$), which, decreases the energy exchange with increasing $\beta_{v1}Kn$, result in the Nu_T trends displayed in Fig. 4.

4.2. Thermally and hydrodynamically developing Nu

Numerical results for thermally and hydrodynamically developing parallel plate Nu_{H2} and Nu_T are presented in Figs. 5 and 6 as functions of x/PeD_h (the nondimensional axial distance), $\beta_{v1}Kn$, β, Br, and Pe. For these data, first-order slip boundary conditions, without creep flow, are used. Thermally developing flow is represented by the solid lines, and thermally/hydrodynamically developing flow, 'combined' flow, is represented by the dotted lines. To verify the accuracy of the numerical data, and that the flow has reached a locally fully developed state, analytic solutions for fully developed Nu, Eq. (10) for Nu_{H2}, and Eq. (12) for Nu_T, are displayed as solid symbols at $x/PeD_h = 4$, the channel outlet. Also, conventional fully developed parallel plate Nu, without rarefaction or viscous dissipation effects, $Nu_{H2} = 8.2353$ in Fig. 5 and $Nu_T = 8.0582$ ($Pe = 0.5$) in Fig. 6, are displayed as circles at $x/Pe\,D_h = 4$ to serve as a point of reference for changes in Nu due to rarefaction, viscous dissipation, and developing flow effects. Additionally, to demonstrate the basis of the thermally/hydrodynamically developing Nu_{H2} and Nu_T results presented in Figs. 5 and 6, velocity profiles and temperature profiles (relative to T_w) for several cases are illustrated in Fig. 7.

Thermally and hydrodynamically developing Nu_{H2}, with viscous dissipation effects, are given in Fig. 5 for various levels of $\beta_{v1}Kn$, Fig. 5(a), and β, Fig. 5(b). Temperature profiles for thermally/hydrodynamically developing flow, with constant wall heat flux thermal boundary conditions, $\beta = 1.667$, $Pe = 0.5$, $\beta_{v1}Kn = 0.00$ and 0.04, and $Br_{H2} = \pm 0.05$ are illustrated in Fig. 7(b). Again, negative Br_{H2} indicates cooling, positive Br_{H2} denotes heating and $Br_{H2} = 0$ signifies no viscous dissipation effect. For the flows examined in Fig. 5, the average Nu_{H2} entrance length (i.e., distance from the channel entrance where $Nu(x) = 0.99Nu_\infty$) is roughly $1.0Pe\,D_h$, and varies little for each of the parameters varied – entrance length increases slightly for combined developing flow, lower values of $\beta_{v1}Kn$, lower values of β, and negative Br_{H2}. As may be expected based on the fully developed Nu_{H2} results presented previously, these results indicate that increasing $\beta_{v1}Kn$, Fig. 5(a), or increasing β, Fig. 5(b), result in a decrease in Nu_{H2} for both developing and fully developed flow. The effect of Br_{H2} on hydrodynamically fully developed flow, shown previously in

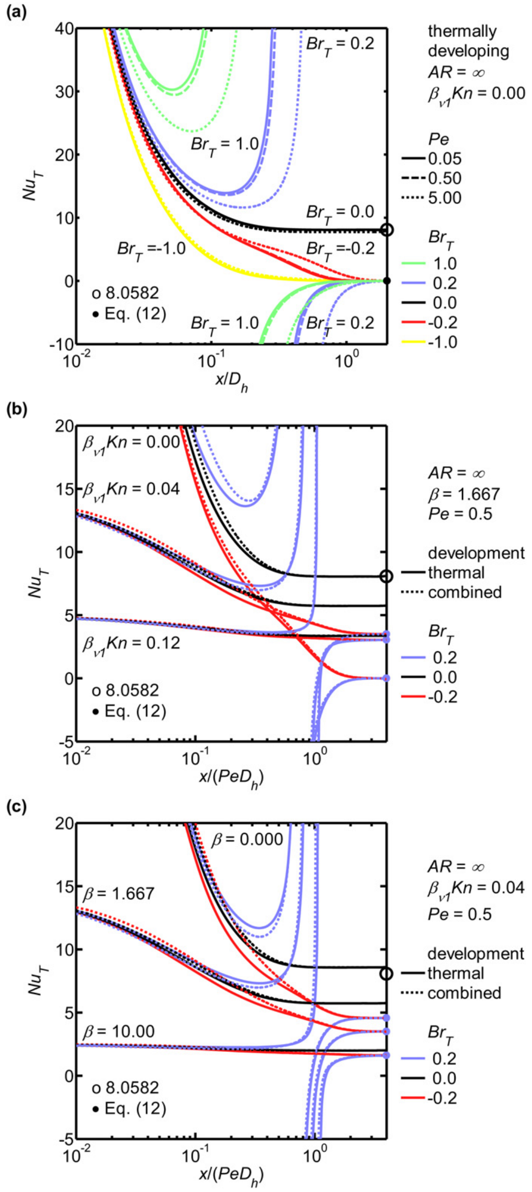

Fig. 6. Thermally and hydrodynamically developing Nu_T: (a) effect of Pe and Br_T, (b) effect of $\beta_{v1}Kn$ and Br_T, (c) effect of β and Br_T.

Figs. 3(a) and 4, is to increase the wall temperature, which, for heating, increases the wall-mean temperature difference and decreases Nu_{H2}, and for cooling, decreases the wall-mean temperature difference and increases Nu_{H2}. This Br_{H2} effect is also evident in the developing Nu_{H2} presented in Figs. 5 and 7(b). Developing Nu_{H2} are larger at the channel inlet, compared to fully developed values, due to the initially small wall-mean temperature difference $|T_w - T_m|$, as illustrated in Fig. 7(b).

Thermally/hydrodynamically developing flows also have large velocities near the wall at the channel inlet, which tends to increase Nu_{H2} beyond that of thermally developing flow alone, as evident in Fig. 5 for $Br_{H2} = 0$. Thermally/hydrodynamically developing flows with $Br_T \neq 0$, additionally, have viscous dissipation and flow work effects that are a function of the hydrodynamic flow development, which, as may be surmised from the velocity profiles in Fig. 7(a), are initially concentrated immediately next to the channel wall at the inlet. For continuum flow, $\beta_{v1}Kn = 0$, at $0.01\,Pe\,D_h$, the dominant effect, moving from the wall to the center of the flow, is first viscous dissipation, then flow work, followed by viscous dissipation again. At $0.01\,Pe\,D_h$ heat conducted at the wall does not yet have a significant effect through the center of the flow, and changes in the temperature profile are primarily due to viscous dissipation and pressure flow effects. As a result of the counteracting viscous dissipation and flow work effects closest to the wall, T_w is slightly decreased, compared to thermally developing flow, and due to the viscous dissipation effect nearest to the center of the flow, the temperature at the center of the flow is slightly increased, compared to thermally developing flow. Because $|T_w - T_m|$ is initially very small, this results in an increase in Nu_{H2} for heating, and decrease in Nu_{H2} for cooling, compared to thermally developing flow, as displayed in Fig. 5(a), for $\beta_{v1}Kn = 0$ and $0.01\,Pe\,D_h$. As the velocity profile develops, the large viscous dissipation and flow work effects near the wall are distributed through the channel and the second region of viscous dissipation is eliminated. As this occurs, viscous dissipation and flow work create a temperature gradient that is conducive to heating, but has an insulating effect for cooling. This results in an accelerated temperature profile development for heating, and a slowed temperature profile development for cooling, as displayed in Figs. 5(a) and 7(b) for $\beta_{v1}Kn = 0$, $Br_{H2} = \pm 0.05$, and ~ 0.032–$0.32\,Pe\,D_h$. In a rarified flow, $\beta_{v1}Kn \neq 0$, slip flow significantly reduces the velocity and pressure gradients at the channel inlet. Compared to continuum flow, this both reduces the magnitude, and alters the distribution of the viscous dissipation and flow work effects. With increased slip near the inlet, flow work is the most significant effect immediately next to the wall (for the $\beta_{v1}Kn$ values examined here). This results in a decrease in $|T_w - T_m|$ for heating, an increase in $|T_w - T_m|$ for cooling, and consequently an increase in Nu_{H2} for $+Br_{H2}$, and a decrease in Nu_{H2} for $-Br_{H2}$, compared to flows that are only developing thermally, as displayed in Fig. 5, for $\beta_{v1}Kn \neq 0$ and $\pm Br_{H2}$. As the flow develops hydrodynamically, viscous dissipation and flow work effects are distributed throughout the cross section of the flow, with viscous dissipation acting predominantly at the walls and flow work acting predominantly at the center of the flow, and the fully developing Nu_{H2} values discussed previously are achieved.

Thermally and hydrodynamically developing Nu_T, with viscous dissipation effects, are given in Fig. 6 for various levels of Pe, Fig. 6(a), $\beta_{v1}Kn$, Fig. 6(b), and β, Fig. 6(c). Temperature profiles for thermally/hydrodynamically developing flow, with

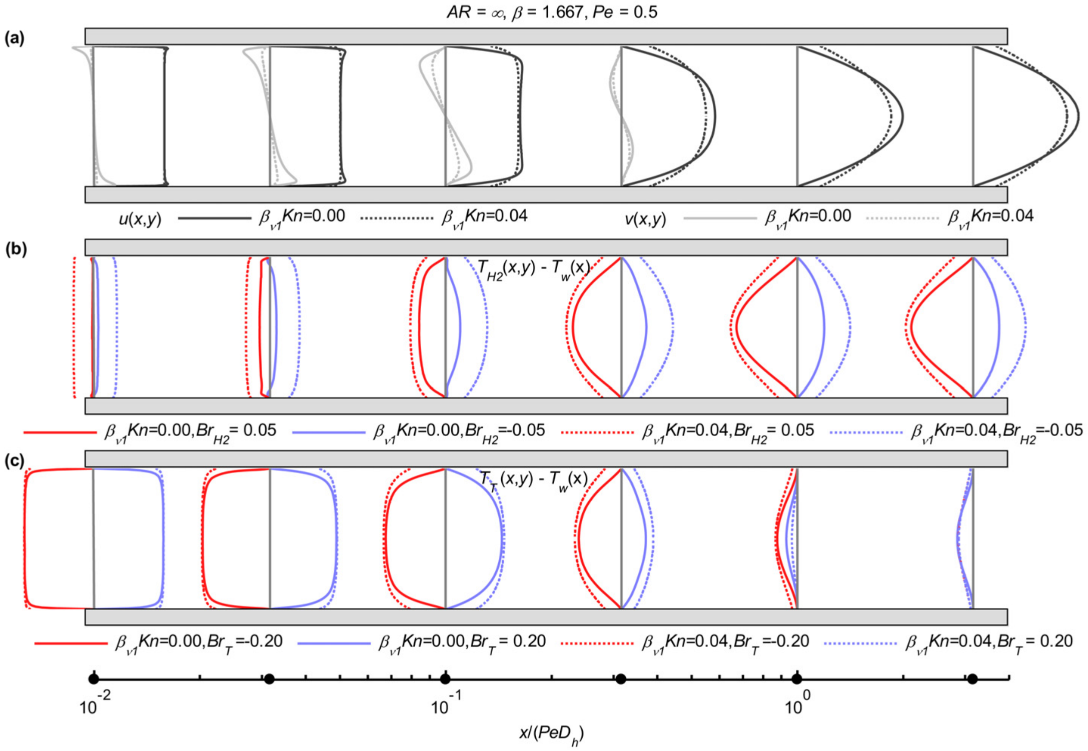

Fig. 7. Thermally/hydrodynamically developing flow: (a) $u(x, y)$ and $v(x, y)$, (b) $T_{H2}(x, y)$, (c) $T_T(x, y)$.

constant wall temperature boundary conditions, $\beta = 1.667$, $Pe = 0.5$, $\beta_{v1}Kn = 0.00$ and 0.04, and $Br_T = \pm 0.20$ are illustrated in Fig. 7(c). Negative Br_T indicates heating, positive Br_T denotes cooling, and $Br_T = 0$ signifies no viscous dissipation effect. For the flows examined in Fig. 6, Nu_T entrance lengths are between approximately $0.5\,Pe\,D_h$ and $4\,Pe\,D_h$, where the entrance length increases for $Br_T \neq 0$ (most significantly for positive Br_T), higher values of Pe, lower values of $\beta_{v1}Kn$, lower values of β, and thermally/hydrodynamically developing flow. The data in Fig. 6(a) demonstrate the effect of Pe and Br_T on thermally developing Nu_T, for continuum flow, $\beta_{v1}Kn = 0$. For cases when viscous dissipation is negligible, $Br_T = 0$, the developing mean fluid temperature approaches the wall temperature, for either heating or cooling, and fully developed Nu_T is a function of Pe. When viscous dissipation and flow work effects are considered ($Br_T \neq 0$), the developing mean fluid temperature, for either heating or cooling, approaches a constant that is less than the wall temperature by an amount dependent on the magnitude of Br_T. The resulting fully developed Nu_T, as predicted by Eq. (12), and discussed previously, is not a function of the magnitude of Br_T or Pe. These developing Nu_T results are most comprehendible when viewed in conjunction with the temperature profiles illustrated in Fig. 7(c) for $\beta_{v1}Kn = 0$ (although, these are for hydrodynamically developing flow). Developing Nu_T are larger at the channel entrance, due to the large temperature gradients at the wall. As the temperature profile develops, Nu_T initially decreases for both heating and cooling. Nu_T for cooling however, reaches a minimum at the axial location were the heat conduction from the wall reaches the center of the flow [12]. As the mean fluid temperature of the cooling flow continues to decrease, due to the effect of flow work, Nu_T exhibits a singularity point where $T_m = T_w$, and is negative just after this when $T_m < T_w$ (q_w is still negative). For continuum non-slip flow, q_w for both heating and cooling, approaches zero, resulting in a fully developed Nu_T value of zero. For slip flow, the fully developed q_w is positive, not zero, due to the effect of shear work at the wall. This results in a positive, nonzero fully developed Nu_T, which for a given value of $\beta_{v1}Kn$ and β, is the same for either heating or cooling, and does not depend on the magnitude of Br_T, as has been discussed previously with the fully developed Nu_T results presented in Fig. 4. Many of the effects of hydrodynamically developing flow on Nu_T, displayed in Figs. 6(a) and 6(b), are similar to those discussed previously for hydrodynamically developing Nu_{H2}. For $Br_T = 0$, hydrodynamically developing flow initially increases Nu_T, compared to thermally developing Nu_T. For $Br_T \neq 0$ and $\beta_{v1}Kn = 0$, Nu_T initially increases, followed by an accelerated thermal development for heating, and for cooling Nu_T initially decreases followed by a slowed thermal development (this effect however, is much less significant for Nu_T, than for Nu_{H2}, and consequently is not displayed in Fig. 6). For $Br_T \neq 0$ and $\beta_{v1}Kn \neq 0$, hydrodynamically developing slip flow results in flow work adjacent to the wall that initially increases Nu_T for heating and decreases Nu_T for cooling, compared to thermally developing Nu_T.

5. Summary and conclusions

The effect of viscous dissipation and rarefaction on rectangular microchannel convective heat transfer is numerically evaluated subject to constant wall heat flux ($H2$) and constant wall temperature (T) thermal boundary conditions in the slip flow regime. Nu_{H2} and Nu_T are presented in terms of the degree of rarefaction ($\beta_{v1}Kn$); the gas–wall interaction parameter (β); viscous dissipation (Br_{H2} or Br_T); and axial conduction (Pe). These results are valid for nearly incompressible, steady state flows. Numerical results are obtained using a continuum based, three-dimensional, compressible, unsteady CFD algorithm, modified with slip velocity and temperature jump boundary conditions. To verify the numerical results, analytic solution for thermally and hydrodynamically fully develop Nu_{H2} and Nu_T are derived for the limiting case of parallel plate channels.

Both analytical and numerical data indicate that effects of viscous dissipation, flow work, and axial conduction are all significant within the slip flow regime for thermally/hydrodynamically developing and locally fully developed Nusselt numbers. The significance of each of these terms depends on the degree of rarefaction, the gas–wall interactions, and the heating configuration. Viscous dissipation effects may either increase or decrease Nu depending on the heating configuration, and are reduced with increasing rarefaction. Viscous dissipation increases Nu_{H2} for cooling, and decreases Nu_{H2} for heating as a function of Br_{H2}, $\beta_{v1}Kn$, β, and AR. The combined effects of viscous dissipation, flow work, and shear work within the slip flow regime cause Nu_T to increase, from zero for continuum flow, with increasing $\beta_{v1}Kn$ by an amount dependent on AR and β but not on the magnitude of Br_T or Pe. Based on the results presented for rarified, constant wall temperature flows, the effects of flow work and shear work may not be assumed to be negligible when viscous dissipation is a significant parameter.

Acknowledgements

Partial support of this work by National Science Foundation grant number DGE9987616, of the Integrative Graduate Education and Research Traineeship Program, and US Department of Energy grant number W-7405-ENG-48, through the Center for the Simulation of Accidental Fires and Explosions, is gratefully acknowledged.

References

[1] J.C. Maxwell, On stresses in rarified gases arising from inequalities of temperature, Philosophical Transactions of the Royal Society of London 170 (1879) 231–256.

[2] M. Smoluchowski, Ueber Wärmeleitung in Verdünnten Gasen, Annalen der Physik und Chemie 64 (1898) 101–130.

[3] G.E. Karniadakis, A. Beskok, Micro Flows: Fundamentals and Simulation, Springer-Verlag, New York, 2002.

[4] J. Maurer, P. Tabeling, P. Joseph, H. Willaime, Second-order slip laws in microchannels for helium and nitrogen, Physics of Fluids 15 (2003) 2613–2621.

[5] S. Colin, P. Lalonde, R. Caen, Validation of a second-order slip flow model in rectangular microchannels, Heat Transfer Engineering 25 (2004) 23–30.

[6] N.G. Hadjiconstantinou, Dissipation in small scale gaseous flows, Journal of Heat Transfer 125 (2003) 944–947.

[7] T.N. Aynur, L. Kuddusi, N. Egrican, Viscous dissipation effect on heat transfer characteristics of rectangular microchannels under slip flow regime and H1 boundary conditions, Heat and Mass Transfer 42 (2006) 1093–1101.

[8] C.-H. Chen, Slip-flow heat transfer in a microchannel with viscous dissipation, Heat and Mass Transfer 42 (2006) 853–860.

[9] H.-E. Jeong, J.-T. Jeong, Extended Graetz problem including streamwise conduction and viscous dissipation in microchannel, International Journal of Heat and Mass Transfer 49 (2006) 2151–2157.

[10] O. Aydin, M. Avci, Analysis of laminar heat transfer in micro-Poiseuille flow, International Journal of Thermal Sciences 46 (2007) 30–37.

[11] K. Hooman, Entropy generation for microscale forced convection: Effects of different thermal boundary conditions, velocity slip, temperature jump, viscous dissipation, and duct geometry, International Communications in Heat and Mass Transfer 34 (2007) 945–957.

[12] J.W. Ou, K.C. Cheng, Effects of flow work and viscous dissipation on Graetz problem for gas flows in parallel-plate channels, Heat and Mass Transfer 6 (1973) 191–198.

[13] R.K. Shah, A.L. London, Laminar Flow Forced Convection in Ducts, Academic Press, New York, 1978.

[14] M. Renksizbulut, H. Niazmand, G. Tercan, Slip-flow and heat transfer in rectangular microchannels with constant wall temperature, International Journal of Thermal Sciences 45 (2006) 870–881.

[15] H.P. Kavehpour, M. Faghri, Y. Asako, Effects of compressibility and rarefaction on gaseous flows in microchannels, Numerical Heat Transfer, Part A: Applications 32 (1997) 677–696.

[16] C. Hong, Y. Asako, S.E. Turner, M. Faghri, Friction factor correlations for gas flow in slip flow regime, Journal of Fluids Engineering 129 (2007) 1268–1276.

[17] R.M. Inman, Laminar slip flow heat transfer in a parallel-plate channel or a round tube with uniform wall heating, NASA TN D-2393, 1964.

[18] J. van Rij, T. Harman, T. Ameel, The effect of creep flow on two-dimensional isoflux microchannels, International Journal of Thermal Sciences 46 (2007) 1095–1103.

[19] J. van Rij, T. Ameel, T. Harman, The effect of viscous dissipation on two-dimensional microchannel heat transfer, in: Proceedings of 2006 ASME International Mechanical Engineering Congress and Exposition IMECE2006, Chicago, IL, United States, 2006.

[20] J. van Rij, T. Ameel, T. Harman, Constant wall temperature Nusselt and Poiseuille numbers in rectangular microchannels, in: Proceedings of 2007 ASME–JSME Thermal Engineering Summer Heat Transfer Conference HT2007, Vancouver, BC, Canada, 2007.

[21] J. van Rij, T. Ameel, T. Harman, Effects of creep flow and viscous dissipation in the slip regime for isoflux rectangular microchannels, in: Proceedings of 2007 ASME International Mechanical Engineering Congress and Exposition IMECE2007, Seattle, WA, United States, 2007.

[22] B.A. Kashiwa, N.T. Padial, R.M. Rauenzahn, W.B. VanderHeyden, A cell-centered ICE method for multiphase flow simulations, Los Alamos National Laboratory Technical Report LA-UR-93-3922, 1993.

[23] S.G. Parker, J. Guilkey, T. Harman, A component-based parallel infrastructure for the simulation of fluid–structure interaction, Engineering with Computers 22 (2006) 277–292.

[24] J.E. Guilkey, T.B. Harman, B. Banerjee, An Eulerian–Lagrangian approach for simulating explosions of energetic devices, Computers and Structures 85 (2007) 660–674.

[25] S. Yu, Slip flow heat transfer in rectangular microchannels, Ph.D. thesis, University of Utah, USA, 2002.

CHAPTER 5

AN EVALUATION OF SECONDARY EFFECTS ON MICROCHANNEL FRICTIONAL AND CONVECTIVE HEAT TRANSFER CHARACTERISTICS

International Journal of Heat and Mass Transfer 52 (2009) 2792–2801

Contents lists available at ScienceDirect

International Journal of Heat and Mass Transfer

journal homepage: www.elsevier.com/locate/ijhmt

An evaluation of secondary effects on microchannel frictional and convective heat transfer characteristics

J. van Rij, T. Ameel [*], T. Harman

Department of Mechanical Engineering, University of Utah, Salt Lake City, UT 84112, USA

ARTICLE INFO

Article history:
Received 28 May 2008
Received in revised form 4 December 2008
Available online 11 February 2009

Keywords:
Rarified flow
Viscous dissipation
Axial conduction

ABSTRACT

The frictional and convective heat transfer characteristics of rarified flows in rectangular microchannels, with either isoflux or isothermal boundary conditions, are evaluated subject to second-order slip boundary conditions, creep flow, viscous dissipation, and axial conduction effects. Numerical results are obtained using a continuum based, three-dimensional, compressible, unsteady computational fluid dynamics algorithm with first- and second-order slip velocity and temperature jump boundary conditions applied to the momentum and energy equations, respectively. The results, reported in the form of Poiseuille and Nusselt numbers, are found to be significant functions of aspect ratio, Knudsen number, slip model parameters, Brinkman number, and Peclet number.

1. Introduction

The heat transfer and friction losses of steady state gaseous flows in microchannels are important due to their applications in microscale heat exchangers, sensors, reactors, power systems, etc. For this reason, there have been numerous studies on slip flow frictional losses and convective heat transfer for constant wall temperature and constant wall heat flux boundary conditions within parallel plate, cylindrical, rectangular, and trapezoidal microchannels. Because conventional micro fabrication methods often produce planar and rectangular channel geometries, an accurate evaluation and understanding of the flow and heat transfer characteristics for rectangular microchannels is particularly important. The majority of previous studies have been analytical, although there are also several numerical studies based on either statistical or continuum methods. Nearly all theoretical studies have assumed first-order accurate slip velocity and temperature jump boundary conditions, laminar, steady state, hydrodynamically fully developed, constant property flow with negligible creep flow, viscous dissipation, and axial conduction effects. However, the accuracy of these simplifications, and consequently the results of these studies, have not yet been verified numerically or experimentally.

There are several factors that cause microscale fluid systems to behave differently than standard macroscale fluid systems. For micro systems with gaseous flows, rarefaction effects may be considerable. Rarefaction takes place as either the size or the pressure of a fluid system decreases, resulting in a mean free path of the fluid molecules that is comparable to the characteristic length of the system itself. When this occurs, discontinuities between the fluid and the solid surface, as well as other noncontinuum behaviors begin to develop. Typically, the Knudsen number, *Kn*, is used to represent the degree of rarefaction, or noncontinuum effects present. The Knudsen number is defined as the ratio of the fluid's molecular mean free path to the characteristic length of the flow. Empirically, the Knudsen number has been used to classify flows into four different regimes [1]. While in the continuum flow regime ($Kn \leqslant 0.01$), conventional continuum conservation of momentum and energy methods, such as the Navier–Stokes equations, may be used. For the free molecular flow regime ($Kn \geqslant 10$), free molecular models such as the Boltzmann equation must be solved. In the transition flow regime ($0.1 \leqslant Kn \leqslant 10$), either numerical solutions of the Boltzmann equation or direct-simulation-Monte-Carlo (DSMC) methods are commonly used. For the slip flow regime ($0.01 \leqslant Kn \leqslant 0.1$), it has been determined experimentally that the deviation of molecular motion from the continuum distribution is small enough that models based on the continuum equations may be used, but with 'slip velocity' and 'temperature jump' boundary conditions that take into account the incomplete momentum and energy exchange between the fluid molecules and the solid surface.

The original slip velocity boundary condition, given in Eq. (1), and temperature jump boundary condition, given in Eq. (2), were derived by Maxwell [2] and Smoluchowski [3], respectively.

$$u|_{y=0} - u_w = \left[\left(\frac{2-\sigma_v}{\sigma_v}\right)\frac{\lambda}{\mu}\tau + \frac{3}{4}\frac{\mu R}{P}\frac{\partial T}{\partial x}\right]_{y=0} \tag{1}$$

$$T|_{y=0} - T_w = \left[\left(\frac{2-\sigma_t}{\sigma_t}\right)\left(\frac{2\gamma}{1+\gamma}\right)\frac{\lambda}{Pr}\frac{\partial T}{\partial y}\right]_{y=0} \tag{2}$$

---

[*] Corresponding author. Tel.: +1 801 585 9730; fax: +1 801 585 9826.
E-mail address: ameel@mech.utah.edu (T. Ameel).

0017-9310/$ - see front matter © 2009 Elsevier Ltd. All rights reserved.
doi:10.1016/j.ijheatmasstransfer.2009.01.001

Nomenclature

AR	aspect ratio, b/h
b	one-half the channel width
Br	Brinkman number, $Br_{H2} = \mu u_m^2/(q_w D_h)$, $Br_T = \mu u_m^2/(k(T_i - T_w))$
c_p	specific heat at constant pressure
c_v	specific heat at constant volume
D_h	hydraulic diameter, $4hb/(h+b)$
f	friction factor, $8\tau_{w,m}/(\rho u_m^2)$
h	one-half the channel height
k	thermal conductivity
Kn	Knudsen number, λ/D_h
L	channel length
Ma	Mach number, $(PeKn/\mathrm{Pr})\sqrt{2/(\pi\gamma)}$
Nu	Nusselt number, $q_{w,m}D_h/(k(T_w - T_m))$
Pe	Peclet number, $Pr\ Re$
Po	Poiseuille number, $f\ Re$
Pr	Prandtl number, $c_p\mu/k$
q	heat flux
R	gas constant
Re	Reynolds number, $\rho u_m D_h/\mu$
T	temperature
u	streamwise velocity
u_c	creep velocity, $(3/4)(\mu R/P)(\partial T/\partial x)\|_{y=0}$
x, y, z	Cartesian coordinates

Greek symbols

β	gas–wall interaction parameter, β_{t1}/β_{v1}
β_{t1}	first-order temperature jump coefficient, $((2-\sigma_t)/\sigma_t)(2\gamma/(1+\gamma))(1/Pr)$
β_{t2}	second-order temperature jump coefficient
β_{v1}	first-order velocity slip coefficient, $(2-\sigma_v)/\sigma_v$
β_{v2}	second-order velocity slip coefficient
$\beta_{v1}Kn$	rarefaction parameter
ε	relative error
γ	ratio of specific heat capacities, c_p/c_v
λ	molecular mean free path, $\mu/(\rho\sqrt{2RT/\pi})$
μ	dynamic viscosity
ρ	density
σ_t	thermal accommodation coefficient
σ_v	momentum accommodation coefficient
τ	shear stress

Subscripts

$H2$	constant wall heat flux condition
i	inlet value
m	mean value
o	nominal continuum value
T	constant wall temperature condition
w	wall value

Eqs. (1) and (2), as well as subsequent equations, are presented in a format assuming a Cartesian coordinate system, a wall normal direction (y), and a streamwise direction (x). The first term in Eq. (1) is the slip velocity due to the shear stress at the wall, and the second term is the thermal creep velocity, u_c, due to a temperature gradient tangential to the wall. Values for the momentum accommodation coefficient, σ_v, and the thermal accommodation coefficient, σ_t, range from zero to one, where $\sigma_v = 0$ represents completely specular reflection, $\sigma_v = 1$, represents completely diffuse reflection, and $\sigma_t = 1$ corresponds to a perfect energy exchange.

Eqs. (1) and (2) are a result of a first-order expansion, in Kn, of the Boltzmann equation, and understood to be applicable only in the slip flow regime. However, in an effort to extend the range of applicability of slip flow boundary conditions to higher Knudsen number flows, specifically the transition regime, many 'second-order' modifications and methods have been proposed [1,4–9]. The boundary conditions derived by Deissler [4], given in Eqs. (3) and (4), and the boundary conditions suggested by Karniadakis and Beskok [1], given in Eqs. (5) and (6), are two of the more commonly applied second-order slip boundary condition models, as well as the only prevalent second-order models that provide temperature as well as velocity boundary conditions.

$$u|_{y=0} - u_w = \left[\left(\frac{2-\sigma_v}{\sigma_v}\right)\lambda\frac{\partial u}{\partial y} - \frac{9}{16}\lambda^2\left(2\frac{\partial^2 u}{\partial y^2} + \frac{\partial^2 u}{\partial x^2} + \frac{\partial^2 u}{\partial z^2}\right)\right]_{y=0} \tag{3}$$

$$\begin{aligned} T|_{y=0} - T_w = \Bigg[&\left(\frac{2-\sigma_t}{\sigma_t}\right)\left(\frac{2\gamma}{1+\gamma}\right)\frac{\lambda}{\mathrm{Pr}}\frac{\partial T}{\partial y} - \frac{9\lambda^2}{256}\left(\frac{177\gamma - 145}{\gamma + 1}\right) \\ &\times\left(2\frac{\partial^2 T}{\partial y^2} + \frac{\partial^2 T}{\partial x^2} + \frac{\partial^2 T}{\partial z^2}\right)\Bigg]_{y=0} \end{aligned} \tag{4}$$

$$u|_{y=0} - u_w = \left(\frac{2-\sigma_v}{\sigma_v}\right)\left[\lambda\frac{\partial u}{\partial y} + \frac{\lambda^2}{2}\frac{\partial^2 u}{\partial y^2}\right]_{y=0} \tag{5}$$

$$T|_{y=0} - T_w = \left(\frac{2-\sigma_t}{\sigma_t}\right)\left(\frac{2\gamma}{1+\gamma}\right)\frac{1}{\mathrm{Pr}}\left[\lambda\frac{\partial T}{\partial y} + \frac{\lambda^2}{2}\frac{\partial^2 T}{\partial y^2}\right]_{y=0} \tag{6}$$

Although many second-order models have been proposed, and some have proven useful in increasing the range and accuracy of the slip boundary condition representation of rarefaction, either experimentally [10,11], or numerically [1], there is currently insufficient experimental data to validate the use of any particular second-order model over another. Nonetheless, as additional experimental and theoretical results become available, convective heat transfer solutions with second-order terms may prove useful. Presently, however, there are few analytical or numerical convective heat transfer solutions based on second-order slip boundary condition models [1,4,12–17], and these are often presented for limited values of Knudsen number, momentum and thermal accommodation coefficients, geometry, etc., and consequently have limited applicability.

In addition to rarefaction effects, there are other effects that are often a result of 'scaling.' Scaling effects are not unique to micro flows, but where in a macro system they are typically negligible, in a micro system they become more prominent and may even dominate the flow characteristics. Many of the scaling effects in micro fluidic systems are a consequence of the increased surface area to volume ratio. This results in increased surface forces, which may produce large pressure drops, compressibility effects, and viscous dissipation; decreased inertial forces, which allows diffusion and conduction processes to become relatively more significant; and increased heat transfer, which may lead to variable fluid properties and creep flow.

While creep flow is typically negligible for large scale flows and fully developed, constant wall temperature flows, creep flow effects may become significant for constant wall heat flux flows within the slip regime. The effect of creep flow has been shown to significantly alter the pressure losses and convective heat transfer rates from that predicted when creep flow is neglected for several geometries [13,16,17]. However, the effect of creep flow on fully developed, constant wall heat flux, rectangular microchannel pressure losses and convective heat transfer rates, calculated in conjunction with slip velocity and temperature jump boundary conditions, has not yet been examined.

In macroscale systems, viscous dissipation effects are only significant for high velocity or highly viscous flows. However, in microscale systems large channel length to hydraulic diameter ratios result in large velocity and pressure gradients, and consequently thermal energy generation due to viscous dissipation. A slight increase in fluid temperature may be significant relative to the small temperature gradients typically present in microchannels, and as a result alter the convective heat transfer rate and any temperature dependant fluid properties, particularly viscosity, which further changes the convective heat transfer rate, as well as the frictional losses. Because the function of many micro fluidic systems is cooling, viscous dissipation becomes a limiting factor that must be accurately represented. Effects of viscous dissipation are characterized by the Brinkman number, *Br*, where $Br \approx 0$ indicates that viscous dissipation effects are negligible. Recently, several studies have focused specifically on viscous dissipation effects for slip flow convective heat transfer [18–26]. However, most of these studies evaluated the effect of viscous dissipation without also evaluating the effects of flow work and shear work, which for gaseous flows are of the same order of magnitude as viscous dissipation; and, viscous dissipation effects in rectangular microchannels with constant wall temperature (T) and constant wall heat flux ($H2$) thermal boundary conditions have not yet been evaluated.

The significance of streamwise conduction is generally established by the magnitude of the flow Peclet number. The Peclet number, *Pe*, represents the ratio of the thermal energy convected to the fluid, to the thermal energy axially conducted within the fluid. A low *Pe*, which is common for micro flows, generally indicates that streamwise conduction effects must be considered. Previous studies have established correlations for the convective heat transfer rate for both continuum and slip flows in parallel plate and circular duct channels with *Pe* as a parameter [25,27–30]. However, axial conduction effects have been neglected in studies on rectangular channel, constant wall temperature flows, and consequently there is an absence of *Nu* data for fully developed conditions at low *Pe* in both the continuum and slip flow regimes.

Based on the preceding review, it is evident that theoretical results for microchannel frictional and convective heat transfer characteristics are generally obtained assuming first-order accurate slip boundary conditions, while second-order slip boundary conditions, creep flow, viscous dissipation, and axial conduction are considered negligible secondary effects. However, the accuracy of these assumptions, and consequently the results of these studies, have not yet been verified numerically or experimentally. The intent of this study is to numerically evaluate the significance of second-order slip boundary conditions, creep flow, viscous dissipation, and axial conduction on the convective heat transfer rate and frictional losses of steady state, laminar, nearly incompressible, locally fully developed, constant wall temperature (T) and constant wall heat flux ($H2$) rectangular microchannel flows in the slip flow regime.

2. Numerical algorithm

The computational fluid dynamics (CFD) algorithm used for this study has been described, and verified in previous microchannel investigations [17,31–33]. The algorithm is based on ICE (Implicit, Continuous-fluid Eulerian), which is a finite volume, multi-material CFD method. The ICE implementation used in this study is well developed and documented [34–37]. The code is three-dimensional, fully compressible, unsteady, and capable of modeling variable fluid properties, fluid–structure interactions, and chemical reactions. To accurately model microchannel flows, the algorithm has been modified to model any of the first- or second-order slip boundary conditions models presented in Eqs. (1)–(6), creep flow, and viscous dissipation. Slip velocity, temperature jump, creep flow, and viscous dissipation effects may be either included or neglected with each computation. The implementation of these modifications is consistent with the original code in being numerically second-order accurate both spatially and temporally.

Numerical results are obtained for the three-dimensional, continuum, momentum and energy equations with both first- and second-order slip velocity and temperature jump boundary conditions for the flow configuration illustrated in Fig. 1. The flow is modeled assuming laminar flow of a Newtonian, ideal gas, with constant properties (c_p, k, μ) of air. To decrease the computational time required to reach a solution, only one quarter of the symmetric microchannel is modeled. The resulting velocity field is then evaluated to obtain the Poiseuille number, *Po*, which is an indication of the pressure drop characteristics and the temperature field is evaluated to obtain the Nusselt number, *Nu*, which represents the convective heat transfer characteristics.

2.1. Solution criteria

For the numerical solutions to be comparable to previous first-order analytic solutions, the flow must be nearly incompressible. To achieve this criterion, a low Mach number, $Ma = (PeKn/\mathrm{Pr})\sqrt{2/(\pi\gamma)}$, is maintained, generally 0.05 or less. For these low *Pe* flows, a channel length of $12h$ is found to be sufficient for *Po* and *Nu* values to become locally fully developed while avoiding significant compressibility effects due to a longer channel. For all cases, a uniform inlet velocity and temperature are specified while the outlet temperature and velocity profiles are allowed to evolve to their locally fully developed profiles. The inlet velocity, inlet temperature, outlet pressure, and wall temperature or wall heat flux are specified to obtain the intended flow *Pe*, u_c/u_m, Br_{H2} or Br_T, and *Kn*.

Because the algorithm is unsteady, all of the flow properties must evolve from a set of initial values to steady state conditions subject to the boundary conditions. The initial velocity field is zero and the initial temperature field is equal to the inlet temperature. The convergence criterion for each time step is a mass flux residual less than 10^{-9} for each control volume. The criterion used to establish that the flow is steady state is $|(u^{n+1} - u^n)/u^{n+1}| \leqslant 10^{-10}$ and $|(T^{n+1} - T^n)/T^{n+1}| \leqslant 10^{-10}$, for each control volume, where n is the number of the time step. The magnitude and number of time steps required to reach steady state are dependent on the grid resolution, $\beta_{v1}Kn$, and *Pe*.

2.2. Grid convergence and code verification

To assure that each numerical result is sufficiently accurate and converges to a grid independent solution, grid resolution studies have been completed for each *Po* and *Nu* reported. Table 1 presents the grid resolution studies for Nu_{H2} with $\beta_{v1}Kn = 0$, and $AR = 1$, 2, and 5. For each aspect ratio, the relative change in Nu_{H2} is less than 0.5% between the two highest grid resolutions. These data indicate that the numerical algorithm converges with approximately second-order numerical accuracy, and that the highest grid resolution

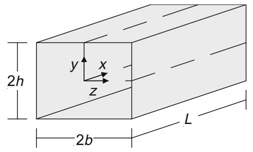

Fig. 1. Rectangular channel configuration.

Table 1
Grid resolution effects on rectangular channel, continuum flow Nu_{H2}, with comparison to analytic solutions.

AR	Grid	Nu_{H2}, present	Nu_{H2} [19]	Nu_{H2} [27]	Nu_{H2} [29]	Nu_{H2} [38]
1	10 × 10 × 120	3.175	3.10	3.09	3.135	3.091
	20 × 20 × 240	3.108				
	40 × 40 × 480	3.092				
2	10 × 20 × 120	3.070	3.03	3.02	3.065	3.022
	20 × 40 × 240	3.031				
	40 × 80 × 480	3.022				
5	10 × 50 × 120	2.964	2.90	2.93	2.961	2.922
	20 × 100 × 240	2.936				
	40 × 200 × 480	2.929				

tested for each *AR*, is sufficiently accurate when compared to the analytic solutions of [19,27,29,38]. Based on these data, all of the following results are obtained using the finest grid resolution given in Table 1.

The algorithm's ability to model first- and second-order velocity slip and temperature jump boundary conditions, as well as creep flow and viscous dissipation has been verified previously for two-dimensional flows with both constant wall heat flux and constant wall temperature boundary conditions [17,31]. Prior to conducting the current study, it must also be verified that the algorithm is capable of accurately modeling axial conduction effects, and three-dimensional, rectangular microchannel pressure losses and convective heat transfer with first-order slip boundary conditions. To establish that the algorithm is accurate in modeling axial conduction effects, numerical and analytical Nu_T [29], as a function of *Pe*, for parallel plate continuum flow are compared in Table 2. These data indicate that the code accurately models axial conduction effects, with an average difference between numerically and analytically computed Nu_T of 0.10%, and a maximum difference of 0.35%.

To verify that the algorithm accurately models first-order slip flow pressure losses in rectangular microchannels, numerically computed *Po*, for the parameters given in Fig. 2(a), are compared to the analytically computed values of [39]. The analytical and numerical *Po* in this comparison do not differ by more than 0.14% and, on average, by only 0.04%, thereby verifying that the algorithm is capable of modeling first-order slip flow pressure losses. To verify that the algorithm accurately models first-order convective heat transfer in rectangular microchannels, numerically computed Nu_{H2}, for the parameters given in Fig. 2(b), are compared to the analytically computed values of [19,29]. This comparison demonstrates that the numerically computed Nu_{H2} values closely agree with the analytically computed values of [29], but the analytic values are an average of 1.26% higher. Although this discrepancy is minor, it may be noted that the values of [29], presented in Table 2 for continuum flow, are also slightly higher, 1.39% on average, than all other references [19,27,38]. The analytically computed values of [19] for $AR = 1$ are all within 0.5% of the present numerical data. At $AR = 5$, there are more significant differences, nearly 10% in some cases, however, the predicted tends due to rarefaction, remain comparable. The excellent agreement of the present Nu_{H2} data and the analytic data of [29], as well as the general agreement in trends of [19], indicates that the code is capable of accurately modeling first-order slip flow convective heat transfer rates for rectangular microchannels.

Table 2
Comparison of numerically and analytically computed Nu_T for parallel plate, continuum flow with axial conduction.

Pe	Nu_T, present	Nu_T [29]	ε (%)
0.005	8.117	8.119	−0.02
0.05	8.111	8.111	0.00
0.5	8.050	8.058	−0.10
5.0	7.720	7.747	−0.35
50	7.563	7.562	0.01

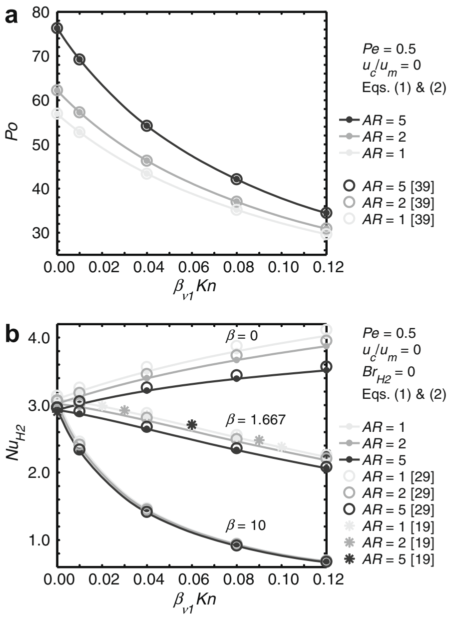

Fig. 2. Comparison of numerically and analytically computed: (a) *Po*, (b) Nu_{H2}.

3. Results and discussion

An evaluation and summary of the effects of first- and second-order slip boundary condition models, creep flow, viscous dissipation, and axial conduction on rectangular microchannel pressure drop and convective heat transfer characteristics are presented in Figs. 3–8. All *Po* and *Nu* are normalized by nominal continuum values without creep flow, or viscous dissipation effects, Po_o and Nu_o, respectively. All numerically computed values are specified by symbols, with the connecting lines representing the data trend. All other relevant flow parameters are indicated in the Figures.

3.1. Second-order slip boundary condition effects

Fully developed Po/Po_o, for the different slip flow boundary condition models, are presented in Fig. 3 for $AR = 1$, 2, 5, and ∞. The boundary conditions are first-order slip, Eqs. (1) and (2), second-order Deissler slip, Eqs. (3) and (4), and second-order Karniadakis and Beskok slip, Eqs. (5) and (6). For these data $Pe = 0.5$, $Br = 0$, and $u_c/u_m = 0$. The data in Fig. 3 indicate that Po/Po_o decreases with $\beta_{v1}Kn$ for all *AR*, and that the effect of *AR* on *Po* is significant in both the continuum and slip flow regimes. Within the continuum flow regime, Po_o decreases from 96, for $AR = \infty$, to 56.9, for $AR = 1$, due to the reduced average wall shear stress caused by the proximity of the corners. Within the slip flow regime, increasing rarefaction, $\beta_{v1}Kn$, increases the slip velocity at the walls, which results in a flatter velocity profile with reduced wall velocity gradients and

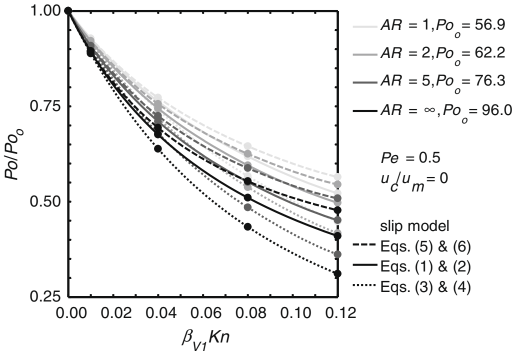

Fig. 3. Effect of second-order slip boundary conditions on fully developed Po/Po_o.

consequently reduces Po/Po_o for all AR. Although Po/Po_o decreases with $\beta_{v1}Kn$ for all AR, the slip velocity is a function of both $\beta_{v1}Kn$ and the average wall velocity gradients, which are larger for higher AR flow, and as a result Po/Po_o decreases more significantly for higher AR flows.

The data in Fig. 3 also illustrate that second-order slip terms become more significant as $\beta_{v1}Kn$ increases. However, the two second-order models have opposite effects when compared to the first-order boundary condition data. This result is expected, due to the opposite signs of the second-order coefficients, given in Eqs. (3) and (5). As compared to the first-order boundary condition data, the second-order Deissler boundary conditions result in an increase in the slip velocity and consequently reduces Po/Po_o with $\beta_{v1}Kn$, while the second-order Karniadakis and Beskok boundary conditions result in a decrease in the slip velocity and consequently increases Po/Po_o with $\beta_{v1}Kn$. Second-order effects are more significant for larger AR due, again, to the larger average wall velocity gradients.

Fully developed Nu_{H2} and Nu_T are presented in Fig. 4 for the same slip flow boundary condition models, Pe, Br, u_c/u_m, and AR values as the Po/Po_o data in Fig. 3. The data in Fig. 4 indicate that both Nu_T and Nu_{H2} may increase or decrease with $\beta_{v1}Kn$, depending on β, for all AR investigated, and that the effect of AR on Nu_T is more significant in both the continuum and the slip flow regimes than it is for Nu_{H2}. Within the continuum flow regime, Nu_T increases significantly from 3.36, at $AR = 1$, to 8.06, at $AR = \infty$ ($Pe = 0.5$). This is due to the varying wall heat flux, which is maximum at the midpoint of the longest side and zero at the corners, resulting in a lower average wall heat flux at lower AR. Nu_{H2}, however, is nearly constant with respect to AR – it decreases approximately 6% from 3.09, at $AR = 1$, to 2.91, at $AR = 10$, and does not approach the $AR = \infty$ value of $Nu_{H2} = 8.235$ [27]. This behavior is due to the $H2$ boundary condition, for which the heat flux is constant both axially and peripherally (the nondimensional wall temperature is maximum at the corners and minimum at the midpoint of the long side), and as such the heat flux on the two side walls will always have an effect, even at large AR.

The data trends in Fig. 4 for the slip flow regime are related to the fact that as rarefaction, $\beta_{v1}Kn$, increases, both the slip velocity and the temperature jump at the wall increase, for $\beta \neq 0$. An increase in the slip velocity enhances the energy exchange near the wall, which tends to increase both Nu_T and Nu_{H2}, as displayed when $\beta = 0$. However, for $\beta \neq 0$, increasing $\beta_{v1}Kn$ also increases the temperature jump, which reduces the energy exchange, increases the difference between the mixed mean fluid temperature and the wall temperature, and tends

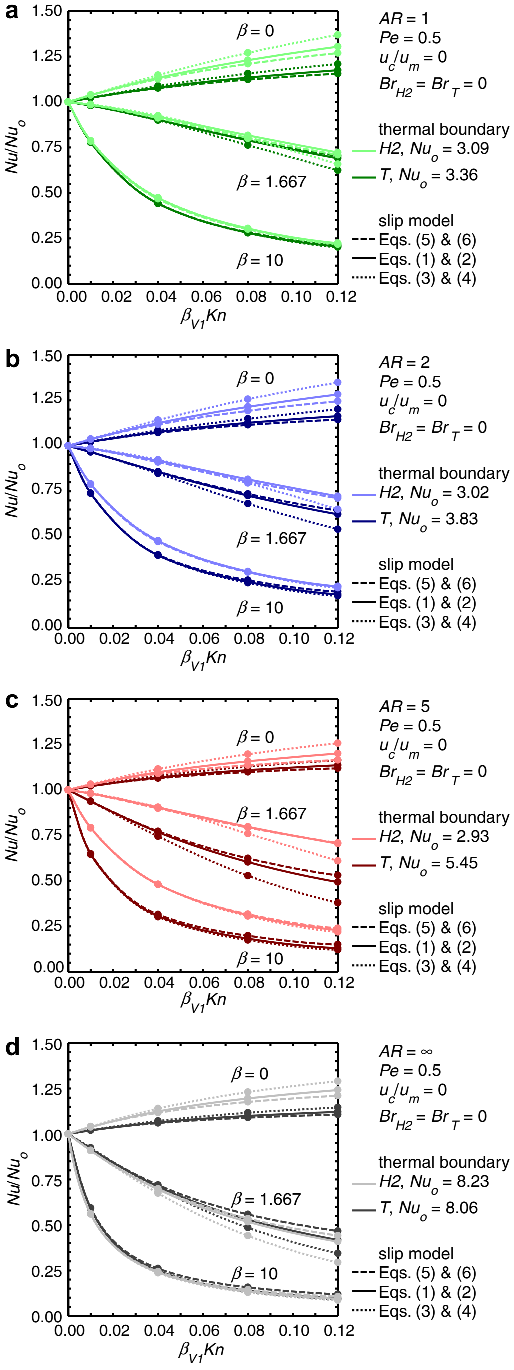

Fig. 4. Effect of second-order slip boundary conditions on fully developed Nu/Nu_o: (a) $AR = 1$, (b) $AR = 2$, (c) $AR = 5$, (d) $AR = \infty$.

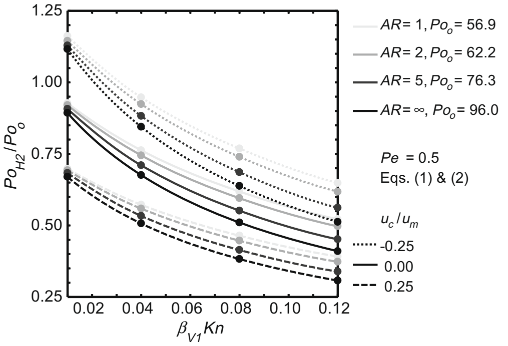

Fig. 5. Effect of creep flow on fully developed Po_{H2}/Po_o.

to decrease both Nu_T and Nu_{H2}. While the wall heat flux is independent of AR and $\beta_{v1}Kn$ for the $H2$ boundary condition, the average wall heat flux for the constant wall temperature boundary condition is reduced for both decreasing AR, and increasing $\beta_{v1}Kn$. These effects result in a less significant increase in Nu_T due to slip, when $\beta = 0$, and a more significant decrease in Nu_T with $\beta_{v1}Kn$, when $\beta \neq 0$, compared to Nu_{H2}.

The results in Fig. 4 also indicate that second-order temperature jump terms become more significant as $\beta_{v1}Kn$ increases. For the constant wall temperature boundary condition the average wall normal first-order and second-order temperature gradients are of opposite sign for all AR, β, and $\beta_{v1}Kn$ evaluated. When $\beta \neq 0$, this causes the second-order Deissler boundary conditions to predict an increase in the temperature jump (decrease in Nu_T), compared to the first-order boundary condition data; while the second-order Karniadakis and Beskok boundary conditions predict a decrease in the temperature jump (increase in Nu_T), compared to the first-order boundary conditions. For the constant wall heat flux boundary condition, the average wall normal first-order and second-order temperature gradients are of the same sign for lower AR and $\beta_{v1}Kn$ values, and of opposite sign for increasing AR and $\beta_{v1}Kn$ values. This causes the second-order Deissler boundary conditions to predict a decrease in temperature jump (increase in Nu_{H2}) for lower AR and $\beta_{v1}Kn$, and an increase in temperature jump (decrease in Nu_{H2}) for higher AR and $\beta_{v1}Kn$, compared to first-order boundary condition data, when $\beta \neq 0$; while the second-order Karniadakis and Beskok boundary conditions predict an increase in temperature jump (decrease in Nu_{H2}) for lower AR and $\beta_{v1}Kn$, and a decrease in temperature jump (increase in Nu_{H2}) at higher AR and $\beta_{v1}Kn$, compared to first-order boundary condition data, when $\beta \neq 0$.

3.2. Creep flow effects

The effect of creep flow on fully developed Po/Po_o and Nu/Nu_o is presented in Figs. 5 and 6, respectively, for creep velocity to mean velocity ratios, u_c/u_m, of −0.25, 0.00, and 0.25, and for AR = 1, 2, 5, and ∞. For these data first-order slip boundary conditions are used, $Pe = 0.5$, and viscous dissipation effects are neglected. Nu_T data are not presented, as creep flow is negligible for thermally fully developed constant wall temperature boundary conditions. Also, because creep flow is zero at $Kn = 0.00$, creep flow effects on Po/Po_o and Nu/Nu_o are not presented for $\beta_{v1}Kn$ less than 0.01. Positive u_c/u_m, creep flow in the same direction as the mean flow, is the result of heating; while negative u_c/u_m, creep flow in the opposite direction of the mean flow, is the result of cooling.

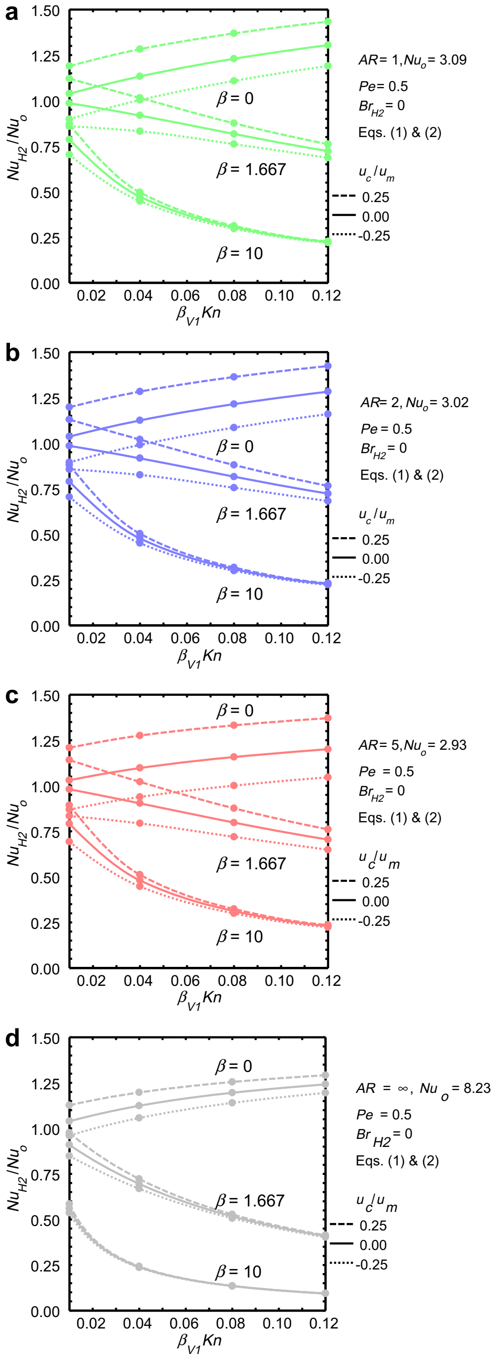

Fig. 6. Effect of creep flow on fully developed Nu_{H2}/Nu_o: (a) AR = 1, (b) AR = 2, (c) AR = 5, (d) AR = ∞.

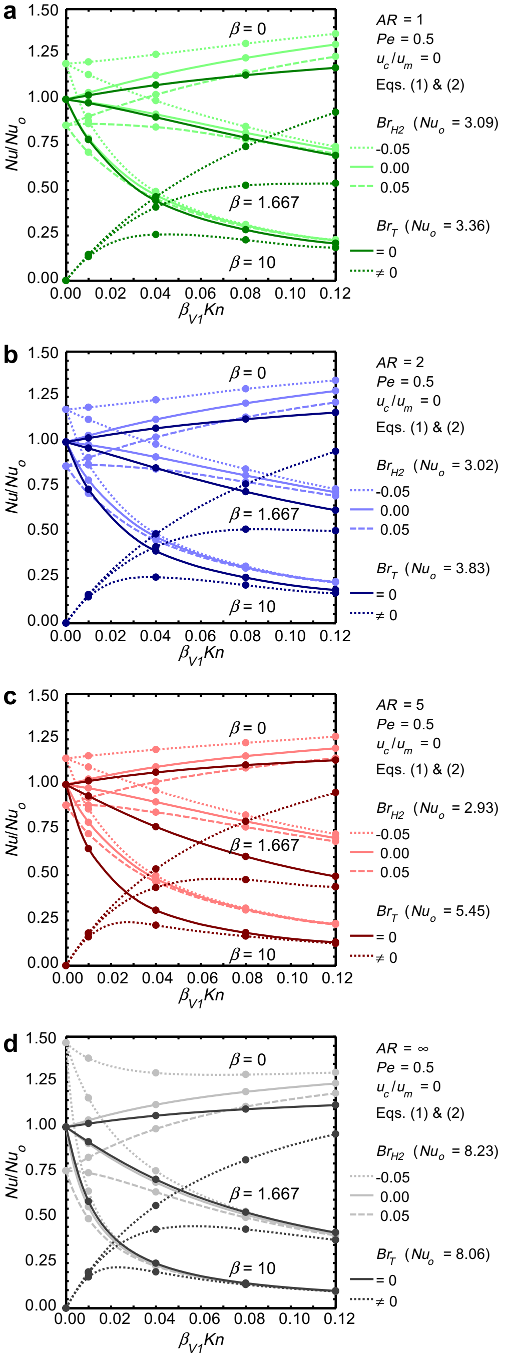

Fig. 7. Effect of viscous dissipation on fully developed Nu/Nu_o: (a) $AR = 1$, (b) $AR = 2$, (c) $AR = 5$, (d) $AR = \infty$.

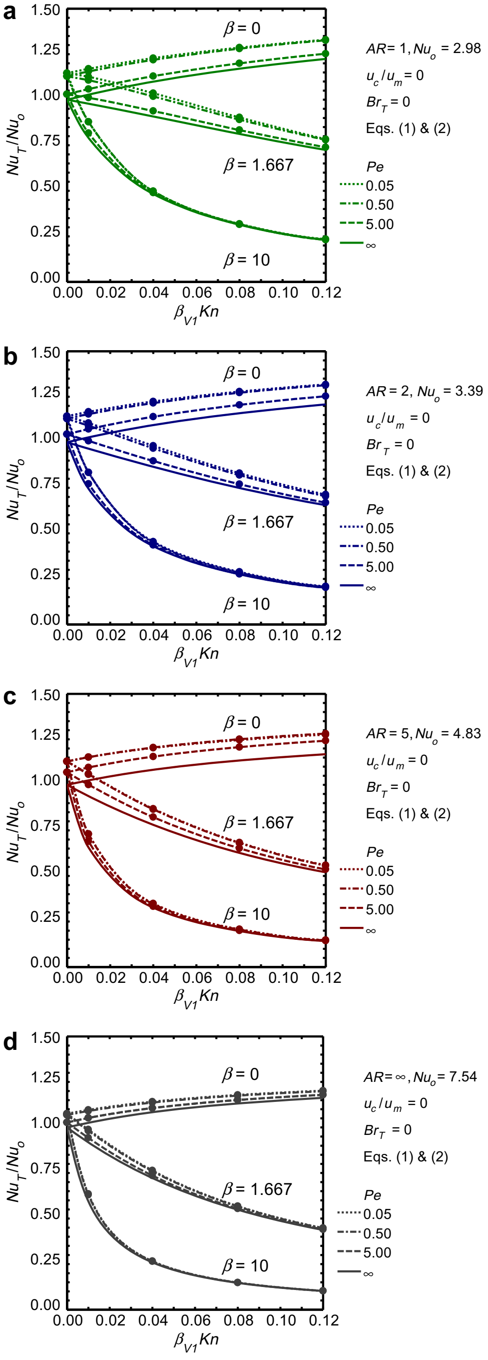

Fig. 8. Effect of axial conduction on fully developed Nu_T/Nu_o: (a) $AR = 1$, (b) $AR = 2$, (c) $AR = 5$, (d) $AR = \infty$.

The data in Fig. 5 demonstrate that in addition to the *AR* and $\beta_{v1}Kn$ effects previously discussed, positive u_c/u_m, heating, decreases Po/Po_o for all *AR*, while negative u_c/u_m, cooling, increases Po/Po_o for all *AR*. Positive u_c/u_m increases the total slip velocity, which decreases the average wall shear stress and reduces Po/Po_o. Conversely, negative u_c/u_m decreases the total slip velocity at the wall which increases the average wall shear stress, thereby increasing Po/Po_o. Also, because positive u_c/u_m reduces the average wall shear stress there is less of a decrease in Po/Po_o with $\beta_{v1}Kn$, and because negative u_c/u_m increases the average wall shear stress there is more of a decrease in Po/Po_o with $\beta_{v1}Kn$.

There are several factors that contribute to the creep flow effect on Nu_{H2}, as presented in Fig. 6. Creep flow in the same direction as the mean flow, heating, increases the total slip velocity, which increases the energy exchange near the wall and tends to increase Nu_{H2}. Creep flow in the opposite direction of the mean flow, cooling, decreases the total slip velocity, which decreases the energy exchange near the wall and tends to decrease Nu_{H2}. However, as rarefaction increases, the effect of the increasing temperature jump at the wall, for $\beta \neq 0$, and decreasing velocity gradients decrease the energy exchange, which increases the mean temperature difference $(T_w - T_m)$ and reduces Nu_{H2}, as well as the effect of u_c/u_m on Nu_{H2}. Although Nu_{H2} for $AR = \infty$ follows the same general trends as Nu_{H2} for $AR = 1$, 2, and 5 the effects of creep flow are reduced without the heat flux and creep flow contribution from the two side walls.

3.3. Viscous dissipation effects

The effect of viscous dissipation, and the related effects of flow work and shear work, on fully developed Nu_{H2} and Nu_T are given in Fig. 7 for $AR = 1$, 2, 5, and ∞. For these data, first-order slip boundary conditions are used, $Pe = 0.5$, and $u_c/u_m = 0$. Because μ is assumed to be constant, viscous dissipation has no additional effect on Po/Po_o. The Po/Po_o data corresponding to the data in Fig. 7 are the same as that given in Fig. 3 for first-order slip boundary conditions. The Nu_{H2} and Nu_T data presented in Fig. 7 are a result of the combined effects of rarefaction ($\beta_{v1}Kn$), the gas–wall interactions (β), and viscous dissipation, flow work, and shear work (*Br*). Viscous dissipation acts as a distributed heat source, with the majority of the thermal energy generated near the wall, due to the larger velocity gradients. Flow work acts as a distributed heat sink, with the majority of the thermal energy absorbed near the center of the flow, due to the larger velocity magnitudes. And, shear work, $u\partial\tau/\partial y|_{y=0}$, acts as a heat source at the wall, due to the thermal energy generated by the slipping flow.

The Nu_{H2} data in Fig. 7 demonstrate that in addition to the *AR* and $\beta_{v1}Kn$ effects discussed previously, positive Br_{H2}, heating, decreases Nu_{H2}, and negative Br_{H2}, cooling, increases Nu_{H2}. This is because viscous dissipation results in an increase in the fluid temperature at the wall, which for heating, increases the difference between the mixed mean fluid temperature and the average wall temperature, thereby reducing Nu_{H2}; while for cooling, this decreases the difference between the mixed mean fluid temperature and the average wall temperature, thereby increasing Nu_{H2}. For the constant wall heat flux boundary condition, flow work decreases the wall temperature and the mixed mean fluid temperature by equal amounts, and consequently Nu_{H2} is unaffected by the flow work contribution [40]. The data in Fig. 7 also indicate that the effect of viscous dissipation is reduced for increasing rarefaction. The reduced effect of Br_{H2} on Nu_{H2} with increasing $\beta_{v1}Kn$ is due to the reduced velocity gradients caused by increasing slip at the wall. Although trends in Nu_{H2} due to viscous dissipation and rarefaction are the same for all *AR* investigated, these effects are more significant for $AR = \infty$ than for $AR = 1$, 2, and 5. This is because the parallel plate channel has larger velocity gradients, resulting in increased viscous dissipation, and with no side wall heat flux contribution the thermal energy generated by viscous dissipation is relatively more significant.

The Nu_T data presented in Fig. 7 with viscous dissipation effects, $Br_T \neq 0$ were obtained for $Pe = 0.5$ and $Br_T = -0.2$. However, as will be explained, for a given $\beta_{v1}Kn$, β, *AR*, and slip boundary condition model, all flows with viscous dissipation and flow work result in the same fully developed value of Nu_T, regardless of the magnitude of *Pe* or Br_T. For fully developed continuum flow, the thermal energy generated by viscous dissipation, is equal to the thermal energy absorbed by flow work. This energy balance results in $\partial T_m/\partial x = 0$, a net wall heat flux of zero, and therefore $Nu_T = 0$, as discussed by [40,27]. Within the slip flow regime, the slip flow at the wall reduces the average cross sectional velocity gradients as well as the maximum core velocity. Although this results in a decrease in both the thermal energy generated by viscous dissipation, and the thermal energy absorbed by flow work, the decrease in viscous dissipation is more significant. The difference, however, is exactly equal to the thermal energy generated by shear work at the wall by the slipping flow - meaning that, for a given velocity profile (which depends on $\beta_{v1}Kn$ and *AR*), viscous dissipation, flow work, and shear work are still balanced energy sources and sinks, i.e. $\partial T_m/\partial x = 0$, regardless of the magnitude of Br_T or *Pe* [20]. However, the shear work at the wall creates a nonzero wall heat flux and therefore a nonzero Nu_T. The shear work, $u\partial\tau/\partial y|_{y=0}$, is a function of both the slip velocity and the wall normal velocity gradients. As $\beta_{v1}Kn$ increases, the slip velocity increases, and for the lower slip flow regime this increases the shear work and therefore increases Nu_T. However, as the slip velocity increases the velocity gradients throughout the flow decrease, and for the upper end of the slip regime this leads to a decrease in the shear work. These effects, combined with the effect of *AR* and temperature jump $(\beta \neq 0)$, which, decreases the energy exchange at the wall with increasing $\beta_{v1}Kn$, result in the Nu_T trends displayed in Fig. 7.

3.4. Axial conduction effects

Fully developed, slip flow Nu_T, computed using $Pe = 0.05$, 0.50, and 5.0, are presented in Fig. 8 for $AR = \infty$, 5, 2, and 1. Using the present compressible flow algorithm, Nu_T can not be computed at large *Pe* without introducing variation due to compressibility. For this reason, Nu_T presented at $Pe = \infty$ are the analytic solutions of [29], for which compressibility and axial conduction effects have been neglected. Nu_{H2} data are not presented, as axial conduction effects are negligible for thermally fully developed constant wall heat flux boundary conditions. Again, because μ is assumed to be constant, axial conduction has no additional effect on Po/Po_o. The Po/Po_o data corresponding to the data in Fig. 8 are the same as that given in Fig. 3 for first-order slip boundary conditions.

For continuum flow, $\beta_{v1}Kn = 0$, the trends of the $Nu(Pe)$ data presented in Fig. 8, for rectangular microchannels, are consistent with those previously presented for parallel plate channels in Table 2. These results indicate that axial conduction effects become significant as *Pe* decreases, and result in an increase in Nu_T. For the range of *Pe* investigated, the average absolute change in Nu_T, is 0.53, for continuum flow. This is equivalent to 7.6% and 15.0% differences, for parallel plate and square channel flows, respectively. Nu_T decreases considerably, approximately 60% of the overall change, from $Pe = 0.5$ to $Pe = 5.0$. This result is expected, as the thermal energy exchange transitions from being dominated by axial conduction, $Pe < 1$, to convection, $Pe > 1$.

The numerical data in the slip flow regime, are consistent with the trends and magnitudes of the data without axial conduction

Nu_T increases with AR, and may increase or decrease with $\beta_{v1}Kn$ depending on β. The data in Fig. 8 illustrate that for decreasing Pe, axial conduction effects increase Nu_T, however this effect is reduced as $\beta_{v1}Kn$ increases. The reduced axial conduction effects correspond to increased convection at the walls caused by the slip velocity for increasing $\beta_{v1}Kn$, and the decrease in the total energy exchange due to the temperature jump, for $\beta \neq 0$.

4. Summary and conclusions

The Poiseuille and Nusselt numbers for rectangular microchannels with both constant wall heat flux and constant wall temperature thermal boundary conditions in the slip regime have been numerically calculated. The resulting Po, Nu_{H2}, and Nu_T include the effects of second-order velocity slip and temperature jump boundary conditions, creep flow, and viscous dissipation with flow work. The numerical results for Po, Nu_{H2}, and Nu_T are presented in terms of the degree of rarefaction ($\beta_{v1}Kn$); the gas–wall interaction parameter (β); creep flow (u_c/u_m); viscous dissipation (Br_{H2} or Br_T); and axial conduction (Pe). These results are valid for incompressible or nearly incompressible, locally fully developed, steady state flows. The numerical solutions for microchannel Po, Nu_{H2}, and Nu_T have been calculated using a continuum based three-dimensional, unsteady, compressible, CFD algorithm modified with slip boundary conditions.

The results of this study indicate that the effects of second-order slip boundary conditions, creep flow, viscous dissipation with flow work, and axial conduction are all significant within the slip flow regime for rectangular microchannel pressure losses and convective heat transfer rates. The significance of each of these terms depends on the degree of rarefaction, the gas–wall interactions, and the thermal boundary conditions. Effects of second-order boundary conditions increase as rarefaction increases, with the two models studied having opposite effects when compared to first-order boundary conditions. The accuracy of solutions generated with the second-order boundary conditions requires comparison with experimental data, which does not currently exist. Creep flow results in an increase in Nu_{H2} for heating and decrease in Nu_{H2} for cooling by an amount dependant on u_c/u_m, $\beta_{v1}Kn$, β, and AR. The effects of creep flow, for a given u_c/u_m, are decreased with increasing $\beta_{v1}Kn$. Viscous dissipation increases Nu_{H2} for cooling and decreases Nu_{H2} for heating as a function of Br_{H2}, $\beta_{v1}Kn$, β, and AR. The combined effects of viscous dissipation, flow work, and shear work within the slip flow regime cause Nu_T to increase with increasing $\beta_{v1}Kn$, by an amount dependent on AR and β, but independent of Br_T and Pe. Axial conduction effects are significant for flow with low Peclet number, and may increase the Nusselt number by up to 15%, for the aspect ratios studied, compared to Nu_T without axial conduction effects. Effects of axial conduction increase with decreasing Pe, and are decreased with increasing $\beta_{v1}Kn$.

Acknowledgements

Partial support of this work by National Science Foundation Grant No. DGE9987616, of the Integrative Graduate Education and Research Traineeship Program, and US Department of Energy Grant No. W-7405-ENG-48, through the Center for the Simulation of Accidental Fires and Explosions, is gratefully acknowledged.

References

[1] G.E. Karniadakis, A. Beskok, Micro Flows: Fundamentals and Simulation, Springer-Verlag, New York, 2002.
[2] J.C. Maxwell, On stresses in rarified gases arising from inequalities of temperature, Philos. Trans. R Soc. Lond. 170 (1879) 231–256.
[3] M. Smoluchowski, Ueber wärmeleitung in verdünnten gasen, Annal. Phys. Chem. 64 (1898) 101–130.
[4] R.G. Deissler, An analysis of second-order slip flow and temperature-jump boundary conditions for rarefied gases, Int. J. Heat Mass Transfer 7 (1964) 681–694.
[5] J. Dai, D. Xu, C. Khoo Boo, Y. Lam Khin, Navier–Stokes simulation of gas flow in micro devices, J. Micromech. Microeng. 10 (2000) 372–379.
[6] J.-M. Li, B.-X. Wang, X.-F. Peng, 'Wall-adjacent layer' analysis for developed-flow laminar heat transfer of gases in microchannels, Int. J. Heat Mass Transfer 43 (2000) 839–847.
[7] H. Xue, Q. Fan, A new analytic solution of the Navier–Stokes equations for microchannel flows, Microscale Thermophys. Eng. 4 (2000) 125–143.
[8] D.A. Lockerby, J.M. Reese, High-resolution Burnett simulations of micro Couette flow and heat transfer, J. Comput. Phys. 188 (2003) 333–347.
[9] M.J. McNenly, M.A. Gallis, I.D. Boyd, Empirical slip and viscosity model performance for microscale gas flow, Int. J. Numerical Methods Fluids 49 (2005) 1169–1191.
[10] J. Maurer, P. Tabeling, P. Joseph, H. Willaime, Second-order slip laws in microchannels for helium and nitrogen, Phys. Fluids 15 (2003) 2613–2621.
[11] S. Colin, P. Lalonde, R. Caen, Validation of a second-order slip flow model in rectangular microchannels, Heat Transfer Eng. 25 (2004) 23–30.
[12] G. An, J.-M. Li, B.-X. Wang, Laminar heat transfer of gas in a parallel-plate microchannel with one wall temperature constant and the other adiabatic, Heat Transfer – Asian Res. 32 (2003) 58–64.
[13] C.o.-K. Chen, H.C. Weng, Developing natural convection with thermal creep in a vertical microchannel, J. Phys. D: Appl. Phys. 39 (2006) 3107–3118.
[14] J.N. Chung, J. Yan, Y. Kun, Numerical simulation of wall roughness on gaseous flow and heat transfer in a microchannel, Int. J. Heat Mass Transfer 49 (2006) 1329–1339.
[15] N. Xiao, J. Elsnab, S. Thomas, T. Ameel, Isothermal microtube heat transfer with second-order slip flow and temperature jump boundary conditions, in: Proceedings of 2006 ASME International Mechanical Engineering Congress and Exposition IMECE2006, Chicago, IL, United States, 2006, p. 9.
[16] X. Zhu, Q. Liao, M.D. Xin, Gas flow in microchannel of arbitrary shape in slip flow regime, Microscale Thermophys. Eng. 10 (2006) 41–54.
[17] J. van Rij, T. Harman, T. Ameel, The effect of creep flow on two-dimensional isoflux microchannels, Int. J. Thermal Sci. 46 (2007) 1095–1103.
[18] G. Tunc, Y. Bayazitoglu, Heat transfer in microtubes with viscous dissipation, Int. J. Heat Mass Transfer 44 (2001) 2395–2403.
[19] G. Tunc, Y. Bayazitoglu, Heat transfer in rectangular microchannels, Int. J. Heat Mass Transfer 45 (2002) 765–773.
[20] N.G. Hadjiconstantinou, Dissipation in small scale gaseous flows, J. Heat Transfer 125 (2003) 944–947.
[21] O. Aydin, M. Avci, Analysis of micro-Graetz problem in a microtube, Nanoscale Microscale Thermophys. Eng. 10 (2006) 345–358.
[22] O. Aydin, M. Avci, Thermally developing flow in microchannels, J. Thermophys. Heat Transfer 20 (2006) 628–632.
[23] T.N. Aynur, L. Kuddusi, N. Egrican, Viscous dissipation effect on heat transfer characteristics of rectangular microchannels under slip flow regime and H1 boundary conditions, Heat Mass Transfer/Waerme Stoffuebertragung 42 (2006) 1093–1101.
[24] C.-H. Chen, Slip-flow heat transfer in a microchannel with viscous dissipation, Heat Mass Transfer/Waerme Stoffuebertragung 42 (2006) 853–860.
[25] H.-E. Jeong, J.-T. Jeong, Extended Graetz problem including streamwise conduction and viscous dissipation in microchannel, Int. J. Heat Mass Transfer 49 (2006) 2151–2157.
[26] W. Sun, S. Kakac, A.G. Yazicioglu, A numerical study of single-phase convective heat transfer in microtubes for slip flow, Int. J. Thermal Sci. 46 (2007) 1084–1094.
[27] R.K. Shah, A.L. London, Laminar Flow Forced Convection in Ducts, Academic Press, New York, 1978 (Chapters 6 and 7).
[28] F. Yan, B. Farouk, Computations of low pressure fluid flow and heat transfer in ducts using the direct simulation Monte Carlo method, J. Heat Transfer 124 (2002) 609–616.
[29] S. Yu, Slip Flow Heat Transfer in Rectangular Microchannels, Ph.D. thesis, University of Utah, Salt Lake City, Utah, 2002.
[30] M. Renksizbulut, H. Niazmand, G. Tercan, Slip-flow and heat transfer in rectangular microchannels with constant wall temperature, Int. J. Thermal Sci. 45 (2006) 870–881.
[31] J. van Rij, T. Ameel, T. Harman, The effect of viscous dissipation on two-dimensional microchannel heat transfer, in: Proceedings of 2006 ASME International Mechanical Engineering Congress and Exposition IMECE2006, Chicago, IL, United States, 2006, p. 9.
[32] J. van Rij, T. Ameel, T. Harman, Constant wall temperature Nusselt and Poiseuille numbers in rectangular microchannels, in: Proceedings of 2007 ASME-JSME Thermal Engineering Summer Heat Transfer Conference HT2007, Vancouver, BC, Canada, 2007, pp. 893–900.
[33] J. van Rij, T. Ameel, T. Harman, Effects of creep flow and viscous dissipation in the slip regime for isoflux rectangular microchannels, in: Proceedings of 2007 ASME International Mechanical Engineering Congress and Exposition IMECE2007, Seattle, WA, United States, 2007, pp. 971–978.
[34] B.A. Kashiwa, N.T. Padial, R.M. Rauenzahn, W.B. VanderHeyden, A Cell-Centered Ice Method for Multiphase Flow Simulations, Los Alamos National Laboratory Technical Report LA-UR-93-3922, 1993.

[35] B.A. Kashiwa, A Multifield Model and Method for Fluid–Structure Interaction Dynamics, Los Alamos National Laboratory Technical Report LA-UR-01-1136, 2001.
[36] S.G. Parker, J. Guilkey, T. Harman, A component-based parallel infrastructure for the simulation of fluid–structure interaction, Eng. Comput. 22 (2006) 277–292.
[37] J.E. Guilkey, T.B. Harman, B. Banerjee, An Eulerian–Lagrangian approach for simulating explosions of energetic devices, Comput. Struct. 85 (2007) 660–674.
[38] M. Spiga, G.L. Morini, Nusselt numbers in laminar flow for H2 boundary conditions, Int. J. Heat Mass Transfer 39 (1996) 1165–1174.
[39] W.A. Ebert, E.M. Sparrow, Slip flow in rectangular and annular ducts, J. Basic Eng. (1965) 1018–1024.
[40] J.W. Ou, K.C. Cheng, Effects of flow work and viscous dissipation on Graetz problem for gas flows in parallel-plate channels, Heat Mass Transfer 6 (1973) 191–198.

CHAPTER 6

SLIP FLOW FLUID-STRUCTURE-INTERACTION

While many microscale systems are subject to both rarefaction and fluid-structure-interaction (FSI) effects, most commercial algorithms cannot model both, if either, of these effects for general applications. This study modifies the momentum and thermal energy exchange models of an existing, continuum based, multi-field, compressible, unsteady, Eulerian-Lagrangian FSI algorithm, such that the equivalent of first-order slip velocity and temperature jump boundary conditions are achieved at fluid-solid surfaces, which may move with time. Following the development and implementation of the slip flow momentum and energy exchange models, several basic configurations are considered and compared to established data to verify the resulting algorithm's capabilities. These verifications include: 1) velocity profiles of a rarified gas between parallel plates; 2) temperature profiles of a rarified gas between parallel plates; 3) drag coefficients, C_D, and Nusselt numbers, Nu, for low Reynolds number rarified flow around an infinite cylinder; and, 4) the transient, thermal/structural response of a damped-oscillatory three-dimensional finite cylinder subject to an impulsively started uniform, rarified flow.

6.1. Background

Both rarefaction and fluid-structure-interaction (FSI) effects are significant for many microscale systems. Examples include micro valves, pumps, actuators, particulate flows, porous flows, two-phase flows, micro-air-vehicles, combustion, and heat exchangers. Rarefaction, typically quantified by the Knudsen number, *Kn*, which is the ratio of the fluid's mean free path to the characteristic length of the system, becomes significant for gaseous systems at the microscale. Rarefaction results in discontinuities of the velocity and temperature at fluid-solid boundaries, which, for the slip flow regime, $0.01 \leq Kn \leq 0.1$, are typically modeled with first-order slip velocity [1] and temperature jump [2] boundary conditions applied to the continuum based conservation of momentum and energy equations, respectively. FSI effects are significant for any system in which the thermal-fluid and structural dynamics are coupled, and consequently can not be considered independently. As listed previously, there are already many microsystems that operate with FSI effects; and, as many microfabrication technologies evolve towards the use of more flexible materials than those historically used in the microelectronics industry, such as with printing and molding [3], FSI effects may become an even more significant microsystem design consideration. However, while there are many microscale systems that are subject to both rarefaction and FSI effects, currently available computational algorithms do not, typically, have the ability or versatility required to accurately model these effects for a generic microsystem, and as a result there are few studies which have considered FSI for microsystems [4-18], and no widely available studies that have numerically considered both FSI and rarefaction in a microsystem.

The primary objective of this study is to modify the momentum and energy exchange models of an existing FSI algorithm, such that the equivalent of first-order slip velocity and temperature jump boundary conditions are achieved at fluid-solid boundaries, which may move and deform arbitrarily with time. The FSI algorithm that is utilized is a three-dimensional, unsteady, continuum based Eulerian-Lagrangian methodology in which fluids, modeled using ICE (implicit, continuous fluid, Eulerian) and solid materials, modeled with MPM (the material-point-method), may be modeled either independently or simultaneously. ICE is a finite volume, cell-centered, multimaterial, compressible, computational-fluid-dynamics (CFD) algorithm that originated at Los Alamos National Laboratory [19, 20]. And, MPM is a particle based method for solid mechanics simulations [21, 22]. The development and documentation of the MPM-ICE implementation currently utilized is given in [23-26]. The MPM-ICE FSI algorithm utilizes a statistically averaged, or 'multifield,' approach, where, each material is continuously defined (ρ, $\boldsymbol{u}$, e, T, υ, θ, $\boldsymbol{\sigma}$, P), with some probability, over the entire computational domain. This approach differs from the, perhaps more common, separate domain methodology, in which, fluid and solid materials are defined separately, with only one material at each point, and interaction only occurs at material boundaries. The multifield approach is advantageous for the current application, because it tightly couples fluid-structure-interactions through the conservation equations, rather than explicitly though specified boundary conditions, which allows arbitrary distortion of material and material surfaces without explicit surface tracking, passing of boundary conditions, and excessive stability and convergence issues. Use of the MPM-ICE algorithm to evaluate rarefaction with FSI is further merited, as rarefaction effects have already been successfully studied utilizing the independent CFD (ICE) portion of the algorithm, with slip boundary conditions implemented at the computational domain boundaries [27-29].

The multimaterial governing conservation equations employed by the MPM-ICE algorithm, without effects that are not considered in the present research (chemical reactions, turbulence, multiphase Reynolds stress, gravity, etc.), are given in Eqs. (6.1) - (6.3) [26].

$$\frac{\partial \rho_r}{\partial t} + \nabla \cdot (\rho \boldsymbol{u})_r = 0 \tag{6.1}$$

$$\frac{\partial (\rho \boldsymbol{u})_r}{\partial t} + \nabla \cdot (\rho \boldsymbol{u}\boldsymbol{u})_r = -\theta_r \nabla P + \nabla \cdot (\theta \boldsymbol{\tau})_r + \sum_{s=1}^{N} \boldsymbol{f}_{rs} \tag{6.2}$$

$$\frac{\partial (\rho e)_r}{\partial t} + \nabla \cdot (\rho e \boldsymbol{u})_r = -\frac{P\theta_r}{\upsilon_r}\frac{d\upsilon_r}{dt} + (\theta \boldsymbol{\tau})_r : \nabla \boldsymbol{u}_r + \nabla \cdot (\theta_r k_r \nabla T_r) + \sum_{s=1}^{N} q_{rs} \tag{6.3}$$

Equations (6.1) - (6.3) are the ensemble average, *r*-material, conservation of mass, momentum, and energy equations respectively, where there are N materials, θ_r is the *r*-material volume fraction, and $\sum_{s=1}^{N} \boldsymbol{f}_{rs}$ and $\sum_{s=1}^{N} q_{rs}$ are models for the momentum and energy exchange between materials. Equations (6.1) – (6.3), along with individual material constitutive or equation-of-state models, and models for $\sum_{s=1}^{N} \boldsymbol{f}_{rs}$ and $\sum_{s=1}^{N} q_{rs}$, form a complete system of equations. The detailed numerical solution strategy utilized by the MPM-ICE algorithm to solve this system of equations is presented in [26], and consequently will not be duplicated here. However, in a few words, the numerical approach involves operator splitting. For each timestep, the quantities on the right-hand-side of Eqs. (6.1) - (6.3) are computed first - this is the Lagrangian phase of the timestep. The conserved quantities, that is, mass, momentum, and energy, for fluid materials are accounted for at the cell centers; while, the conserved quantities for solid materials are accounted for at the material particles. Consequently, during the Lagrangian phase, which is executed primarily within the cell-centered ICE framework, the solid materials are dually represented, both, at the particles, and at the cell centers, where the solid material conservation quantities are interpolated. In the second phase of the timestep, the Eulerian phase, the contribution due to advection, that is, the second term on the left of Eqs. (6.1) - (6.3), is added to the Lagrangian phase values, where the advected contributions are computed for fluid materials by ICE, and for solid materials by MPM. As such, during the Lagrangian phase, models for both the momentum and energy exchange between materials, $\sum_{s=1}^{N} \boldsymbol{f}_{\boldsymbol{rs}}$ and $\sum_{s=1}^{N} q_{rs}$, respectively, are utilized, while during the Eulerian phase, only the momentum exchange model is utilized.

The momentum and energy exchange models currently employed by the MPM-ICE algorithm to model FSI for standard continuum conditions ($Kn \approx 0$), are given in Eqs. (6.4) and (6.5).

$$\sum_{s=1}^{N} \boldsymbol{f}_{rs} = \sum_{s=1}^{N} K_{rs}\theta_r\theta_s\left(\boldsymbol{u}_s - \boldsymbol{u}_r\right) \tag{6.4}$$

$$\sum_{s=1}^{N} q_{rs} = \sum_{s=1}^{N} H_{rs}\theta_r\theta_s\left(T_s - T_r\right) \tag{6.5}$$

Eq. (6.4) models $\boldsymbol{f}_{\boldsymbol{rs}}$, the force per unit volume on material r, due to interaction with material s, as a function of the scalar momentum exchange coefficient, K_{rs}, the material volume fractions, and the relative velocity between the two materials. Similarly, Eq. (6.5) models q_{rs}, the thermal energy exchange rate per unit volume for material r, due to interaction with material s, as a function of the scalar energy exchange coefficient, H_{rs}, the material volume fractions, and the temperature difference between the two materials. To avoid stability and convergence restrictions, the momentum and thermal energy exchange between materials is calculated within each cell implicitly, for each timestep, as shown in Eqs. (6.6) and (6.7).

$$\rho_r \boldsymbol{u}_r^+ = \rho_r \boldsymbol{u}_r^- + \Delta t \sum_{s=1}^{N} K_{rs} \theta_r \theta_s \left(\boldsymbol{u}_s^+ - \boldsymbol{u}_r^+ \right) \tag{6.6}$$

$$\rho_r c_{\upsilon,r} T_r^+ = \rho_r c_{\upsilon,r} T_r^- + \Delta t \sum_{s=1}^{N} H_{rs} \theta_r \theta_s \left(T_s^+ - T_r^+ \right) \tag{6.7}$$

The '-' and '+' superscripts in Eqs. (6.6) and (6.7) indicate values before and after the momentum and thermal energy exchange between materials, respectively, at the point in the timestep that the exchange contributions are calculated. It is assumed with the calculation of Eqs. (6.6) and (6.7) that the material masses, volume fractions, and specific heats are not modified by the momentum and energy exchange between materials. (The exchange of mass, momentum, and energy due to a chemical reaction, although not consider in this study, would be modeled with additional terms in the governing equations, not Eqs. (6.4) and (6.5), as discussed in [26].) It is also necessary with the implementation of Eqs. (6.6) and (6.7) to specify momentum and energy exchange coefficients for all possible material pairs. However, K_{rs} must equal K_{sr}, and H_{rs} must equal H_{sr}, since the force, and heat transferred, from material r due to material s is equal and opposite the force, and heat transferred, from material s due to material r. And, $K_{rr} = H_{rr} = 0$, because the stress and heat flux within the same material are already considered in other terms of the momentum and energy conservation equations. A very large momentum transfer rate between materials r and s, specified by a large K_{rs} value, forces the relative velocity of the two materials to zero, consistent with a no-slip velocity boundary condition. Similarly, a large H_{rs} value produces a large thermal energy transfer rate between materials r and s, resulting in the equivalent of a thermal equilibrium boundary condition. In the current algorithm, K_{rs} and H_{rs} values are typically specified as arbitrarily large, constant, scalar quantities ($\sim 1\times 10^{15}$), which results in momentum and thermal energy transfer rates that are not directional relative to the fluid-solid surface, but produce the intended effect of conventional no-slip velocity and thermal equilibrium boundary conditions.

The objective of this study, as stated previously, is to modify the momentum and energy exchange models in the FSI algorithm, such that the equivalent of first-order slip velocity and temperature jump boundary conditions are achieved at fluid-solid surfaces for a rarified gas in the slip flow regime. To accomplish this, momentum and energy exchange coefficients, K_{rs}^{slip} and H_{rs}^{slip}, which result in tangential slip velocity and temperature jump values that correspond to values predicted by the standard first-order slip boundary conditions [1, 2], are derived as a function of the level of rarefaction. Then, because the slip flow momentum exchange coefficient is only applicable in the fluid-solid surface tangential direction, while a no-slip momentum exchange coefficient must still be applied in the fluid-solid surface normal direction, the momentum exchange coefficient can no longer be treated as a scalar quantity. Meaning that, the momentum exchange between materials must be calculated in fluid-solid surface normal and tangential coordinate directions, rather than the arbitrary global coordinate directions. Following the development and implementation of the slip flow momentum and energy exchange models, several basic configurations are considered and compared to established data to verify the resulting algorithm's capabilities. These verifications include: 1) velocity profiles of a rarified gas between parallel plates; 2) temperature profiles of a rarified gas between parallel plates; 3) drag coefficients, C_D, and Nusselt numbers, Nu, for low Reynolds number rarified flow around an infinite cylinder; and, 4) the transient, thermal/structural response of a damped-oscillatory three-dimensional finite cylinder subject to an impulsively started uniform, rarified flow.

6.2. Slip flow modifications

Several modifications to the momentum and energy exchange models in the MPM-ICE FSI algorithm must be implemented to correctly model the momentum and energy exchange between a rarified gas and a moving, deforming solid surface. First, slip flow momentum and energy exchange coefficients must be derived as a function of the level of rarefaction. Then, the slip flow momentum and thermal energy exchange models, with a tensor momentum exchange coefficient, must be applied at fluid-solid surfaces.

6.2.1. Slip flow momentum and energy exchange coefficients

The tangential momentum exchange between a rarified gas, denoted as material r, and a solid material, material s, is described by the first-order slip velocity boundary condition, Eq. (6.8) [1]. To obtain the force per unit volume on the rarified gas due to interaction with the solid, $\boldsymbol{f}_{rs}$, the shear stress on the gas, $-\boldsymbol{\tau}$ from Eq. (6.8), is multiplied by the fluid-solid surface area in the cell, A, as well as the gas volume fraction, θ_r, and then divided by the cell volume, V, as shown in Eq. (6.9). For $\boldsymbol{f}_{rs}$ in Eq. (6.9) to be equivalent to the momentum exchange model utilized by the algorithm, Eq. (6.4), the slip flow tangential momentum exchange coefficient, K_{rs}^{slip}, must be that given by Eq. (6.10).

$$\boldsymbol{u}_r - \boldsymbol{u}_s = \frac{\beta_v \lambda_r}{\mu_r} \boldsymbol{\tau} \tag{6.8}$$

$$\boldsymbol{f}_{rs} = -\theta_r \boldsymbol{\tau} \left(\frac{A}{V} \right) = \left(\frac{\theta_r \mu_r}{\beta_v \lambda_r} \right) \left(\frac{A}{V} \right) (\boldsymbol{u}_s - \boldsymbol{u}_r) \tag{6.9}$$

$$K_{rs}^{slip} = \left(\frac{\mu_r}{\beta_v \lambda_r} \right) \left(\frac{A}{V} \right) \left(\frac{1}{\theta_s} \right) \tag{6.10}$$

In a similar fashion, using the first-order temperature jump boundary condition, Eq. (6.11) [2], and the energy exchange model, Eq. (6.5), the slip flow energy exchange coefficient is obtained in Eqs. (6.12) - (6.13).

$$T_r - T_s = -\frac{\beta_t \lambda_r}{k_r} q'' \tag{6.11}$$

$$q_{rs} = \theta_r q'' \left(\frac{A}{V} \right) = \left(\frac{\theta_r k_r}{\beta_t \lambda_r} \right) \left(\frac{A}{V} \right) (T_s - T_r) \tag{6.12}$$

$$H_{rs}^{slip} = \left(\frac{k_r}{\beta_t \lambda_r} \right) \left(\frac{A}{V} \right) \left(\frac{1}{\theta_s} \right) \tag{6.13}$$

K_{rs}^{slip}, Eq. (6.10), and H_{rs}^{slip}, Eq. (6.13), are functions of the rarified gas viscosity, μ_r, thermal conductivity, k_r, and mean free path, λ_r; the solid material volume fraction, θ_s; the first-order slip velocity and temperature jump coefficients, β_v and β_t, respectively; and, the individual cell fluid-solid surface area, A, and volume, V. Values for μ_r, k_r, θ_s, and V are available within the unmodified algorithm, and A may be approximated as the area of the cell face that is most tangential to the fluid-solid surface within the cell. Values for β_v, β_t, and λ_r are calculated according to Eqs. (6.14) - (6.16), respectively [1, 2].

$$\beta_v = \frac{2-\sigma_v}{\sigma_v} \tag{6.14}$$

$$\beta_t = \left(\frac{2-\sigma_t}{\sigma_t}\right)\left(\frac{2\gamma_r}{1+\gamma_r}\right)\left(\frac{k_r}{c_{p,r}\mu_r}\right) \tag{6.15}$$

$$\lambda_r = \frac{\mu_r}{\rho_r\sqrt{2c_{\upsilon,r}(\gamma_r-1)T_r/\pi}} \tag{6.16}$$

The momentum accommodation coefficient, σ_v in Eq. (6.14), and the thermal accommodation coefficient, σ_t in Eq. (6.15), must be measured experimentally. Values for σ_v and σ_t range from zero to one, where $\sigma_v = 0$ represents completely specular reflection, $\sigma_v = 1$ represents completely diffuse reflection, and $\sigma_t = 1$ corresponds to a perfect energy exchange. Experimentally measured values for σ_v and σ_t are, however, typically near unity, and consequently, are approximated as such for all calculations presented within this study. With $\sigma_v = \sigma_t = 1$, and using typical properties for air, $\gamma = 1.4$ and $Pr = 0.7$, $\beta_\upsilon = 1.0$ and $\beta_t = 1.667$. The rarified gas mean free path, λ_r, Eq. (6.16), is calculated for each cell of the computational domain, at the beginning of each timestep, as a function of μ_r, ρ_r, $c_{\upsilon,r}$, γ_r, and T_r.

6.2.2. Slip flow momentum and thermal energy exchange between materials

The original slip velocity and temperature jump boundary conditions given in Eqs. (6.8) and (6.11) [1, 2], were derived with the assumption that a rarified gas flow within the slip flow regime may be accurately approximated as a continuum, everywhere, except at the fluid-solid boundaries. Likewise, for the numerical algorithm, in which all materials are continuously defined, to accurately model a flow within the slip flow regime, the algorithm must produce approximately equivalent velocities for all materials, and approximately equivalent temperatures for all materials within the same cell, everywhere, except at the fluid-solid boundaries, where discontinuities in the velocity and temperature between the fluid and solid materials may occur. Therefore, the unmodified K_{rs} and H_{rs}, i.e. the arbitrary large, constant, scalar values that result in negligible velocity and temperature differences between materials within the same cell, are applied in the usual manner, everywhere, except at the fluid-solid surface. At the fluid-solid surface, slip flow momentum and energy exchange coefficients, K_{rs}^{slip} and H_{rs}^{slip}, respectively, must be applied, once the fluid-solid surface is identified. In the MPM algorithm, solid materials are modeled with material particles, typically eight particles per cell. As such, a surface is identified as a cell that has material particles of the specified solid material, but with less than eight particles. Because the surface may be in motion, and surfaces are not explicitly tracked, it is necessary with this approach to test each cell of the computational domain, with each timestep, to determine if it is a surface cell. If a surface cell is identified, K_{rs}^{slip} and H_{rs}^{slip}, as defined in Eqs. (6.10) and (6.13), are then calculated for that cell.

Temperature is a scalar quantity, and consequently, once a surface cell is identified, and H_{rs}^{slip} is calculated, calculation of the thermal energy exchange between materials in that cell may precede using the usual algorithm, that is, the numerical implementation of Eq. (6.7), with H_{rs}^{slip} rather than H_{rs}. Velocity, however, is a vector quantity, and the momentum exchanged between materials must take place with respect to the coordinate system in which the velocity components are defined. In the unmodified algorithm, K_{rs} does not change with direction, and so, the exchange of momentum between materials may be executed in the arbitrary global Cartesian coordinate system, $(\boldsymbol{x},\boldsymbol{y},\boldsymbol{z})$, in which, the velocities are originally defined. However, because K_{rs}^{slip} is only applicable in the fluid-solid surface tangential direction, while the standard no-slip K_{rs} must be applied in the fluid-solid surface normal direction, the momentum exchange between materials for slip flow must be executed in a coordinate system defined by the fluid-solid surface. The surface coordinate system $(\boldsymbol{x}',\boldsymbol{y}',\boldsymbol{z}')$, as illustrated by a hypothetical surface in Fig. 6.1, is defined by rotating $(\boldsymbol{x},\boldsymbol{y},\boldsymbol{z})$ by φ about $\boldsymbol{z}$, and then ψ about $\boldsymbol{y}$, such that $\boldsymbol{y}'$ is the outward unit normal direction of the solid surface. Where $\boldsymbol{y}'$ is calculated using the density gradient of the solid material particles within the surface cell, as shown in Eq. (6.17).

$$\boldsymbol{y}' = -\nabla\rho_s / \left|\nabla\rho_s\right| \tag{6.17}$$

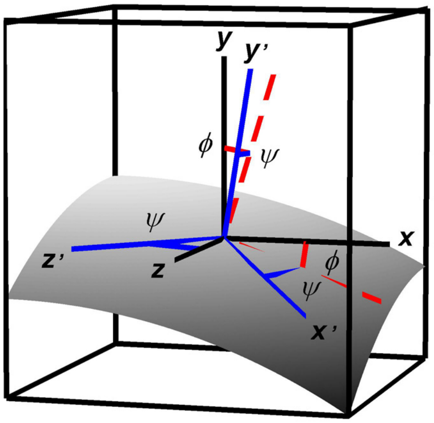

Fig. 6.1. Global and surface coordinate systems.

The material velocities in terms of $(\boldsymbol{x}', \boldsymbol{y}', \boldsymbol{z}')$ are obtained by applying the rotation matrix *Q*, given in Eq. (6.18), to $\boldsymbol{u}$ as shown in Eq. (6.19). By definition, *Q* is a real, orthogonal, special matrix ($Q^T = Q^{-1}$, $\det(Q) = 1$), in which the rows represent the $(\boldsymbol{x}', \boldsymbol{y}', \boldsymbol{z}')$ unit vectors as defined in the original $(\boldsymbol{x}, \boldsymbol{y}, \boldsymbol{z})$ system. Once the velocities are defined in terms of the $(\boldsymbol{x}', \boldsymbol{y}', \boldsymbol{z}')$ coordinates, the momentum exchange between materials is calculated for each surface coordinate direction, utilizing the numerical implementation of Eq. (6.6), with K_{rs}^{slip} in the ***x'*** and ***z'*** directions, and the no-slip K_{rs} in the ***y'*** direction. Following the exchange of momentum between materials in the $(\boldsymbol{x}', \boldsymbol{y}', \boldsymbol{z}')$ system, the material velocities are then returned to the $(\boldsymbol{x}, \boldsymbol{y}, \boldsymbol{z})$ description utilizing Q^T as shown in Eq. (6.20).

$$Q = \begin{bmatrix} x'_x & x'_y & x'_z \\ y'_x & y'_y & y'_z \\ z'_x & z'_y & z'_z \end{bmatrix} = \begin{bmatrix} cos\phi cos\psi & -sin\phi & cos\phi sin\psi \\ sin\phi cos\psi & cos\phi & sin\phi sin\psi \\ -sin\psi & 0 & cos\psi \end{bmatrix} \rightarrow \begin{bmatrix} \frac{y'_y y'_x}{\sqrt{1-y'^2_y}} & -\sqrt{1-y'^2_y} & \frac{y'_y y'_z}{\sqrt{1-y'^2_y}} \\ y'_x & y'_y & y'_z \\ \frac{-y'_z}{\sqrt{1-y'^2_y}} & 0 & \frac{y'_x}{\sqrt{1-y'^2_y}} \end{bmatrix} \tag{6.18}$$

$$\sum_{s=1}^{N} \boldsymbol{u}'^{-}_{s} = \sum_{s=1}^{N} Q\boldsymbol{u}^{-}_{s} \tag{6.19}$$

$$\sum_{s=1}^{N} \boldsymbol{u}^{+}_{s} = \sum_{s=1}^{N} Q^T \boldsymbol{u}'^{+}_{s} \tag{6.20}$$

As described previously, the models for momentum and thermal energy exchange between materials, and consequently the slip flow modifications made to these models, are implemented in the MPM-ICE algorithm to calculate both the momentum and thermal energy change during the Lagrangian phase of the timestep, as well as the fluid advection velocity during Eulerian phase of the timestep.

6.3. Numerical results

To verify the methodology and implementation of the modifications described for the slip flow momentum and energy exchange models, several basic configurations, as outlined previously, are numerically evaluated. For each configuration, the numerical results are substantiated with grid convergence and order-of-accuracy studies, as well as comparison to analytical, experimental, or previously established numerical data. The MPM-ICE algorithm, and therefore each of the following studies, is explicit with time. Consequently, the maximum stable timestep for each simulation is limited by either diffusion ($\Delta t \leq 0.5 \cdot \Delta x^2/v$, $\Delta t \leq 0.5 \cdot \Delta x^2/\alpha$) or the speed-of-sound ($\Delta t \leq cfl \cdot \Delta x/(|\boldsymbol{u}| + \mathrm{c})$) for each material [30]. The *cfl* utilized for all of the following studies is between 0.4 and 0.6. Aside from the three-dimensional, flexible cylinder study, the speed-of-sound in the solid material produces the limiting timestep. (Although, the ability to implicitly evaluate pressure exists in ICE, this does not increase the maximum timestep based on the speed-of-sound within the explicit MPM algorithm, and consequently, has not been utilized.) To obtain slow transient and steady state data, this acoustic timestep is very limiting, particularly for refined grid resolutions, and as a result, the relatively simple configurations, require significant computing resources, which are only feasible due to the massively parallel computing infrastructure for which the MPM-ICE algorithm was developed [31]. The first two studies, which are the evaluation of velocity and temperature profiles of a rarified gas between parallel plates, utilize 1 CPU for approximately 0.05 - 8h, depending on the grid resolution. The third study, rarified flow around a two-dimensional cylinder, utilizes 72 CPUs for approximately 12 - 400h, depending on the grid resolution. And, the final study, the three-dimensional, flexible cylinder, utilizes 150 CPUs for about 10 - 240h, again, depending on the grid resolution. The MPM-ICE algorithm is nondimensional, and so to reduce some of the numerical round-off error incurred with long computation times, each of the microscale problems are evaluated in terms of μm, μs, fg, and K. It should be noted that this is not 'scaling' the problem in an attempt to reduce the number of required timesteps. If the problem were scaled, all of the nondimensional variables that describe the physical process, such as *Re*, *Ma*, *Pr*, etc., must remain constant, and therefore the corresponding nondimensional timeframe required for the physical process to occur, such as the Fourier number, *Fo*, will also remain constant. Thus, unless the problem of interest is changed, i.e. changing *Re*, *Ma*, *Pr*, etc., scaling Δx may increase Δt, but will also proportionally increase the total time required to reach a specified point in the physical process, such as steady state, and the total number of explicit timesteps will remain the same.

6.3.1. Pressure driven flow between parallel plates

A pressure driven, fully developed, steady state, Newtonian, rarified ideal gas flow between parallel plates with constant properties and negligible inertial forces, as specified in Fig. 6.2(a), is modeled to verify the accuracy and implementation of the slip flow momentum exchange modifications in the MPM-ICE algorithm. The analytic velocity solution used to verify the numerical data, Eq. (6.21), is obtained by integrating the momentum equation, $\mu\left(\partial^2 u/\partial y^2\right) = dP/dx$, twice and applying the slip velocity boundary condition at the wall, $u\big|_{y=0} = \beta_v \lambda \left(\partial u/\partial y\right)_{y=0}$, and symmetry at the midplane, $\left(\partial u/\partial y\right)_{y=h/2} = 0$, and then normalizing by the resulting mean velocity, u_m.

$$\frac{u(y/h)}{u_m} = \frac{6\left(y/h - y^2/h^2 + 2\beta_v Kn\right)}{1 + 12\beta_v Kn} \tag{6.21}$$

Equation (6.21), as well as the Boltzmann equation solution presented by [32], for comparable conditions (hard sphere molecules, diffuse reflection, uniform pressure gradient, negligible inertial forces), are compared to the numerical data at steady-state (t = 0.05μs) in Figs. 6.2(b)-(c) for the parameters specified.

Grid convergence, order-of-accuracy, and conservation of momentum exchange data for this configuration, as well as the total number of timesteps required to reach t = 0.05μs, are reported in Table 6.1. The data in Table 6.1 for no-slip flow, Kn_m = 0, are produced using the original algorithm, while the data reported for Kn_m = 0.0564 and 0.1128 are obtained using the algorithm with the slip flow momentum exchange model. The L_2 norm error in Table 6.1 refers to the difference between the normalized numerical and analytical velocity profiles. The order-of-accuracy [30], p, computed with the L_2 norm errors, indicate that both the original and modified algorithm converge with increasing grid resolution with an order-of-accuracy of approximately one. It may also be noted in Figs. 6.2(b)-(c) that, although the error between the numerical and analytical data increase slightly near the wall, the numerical data agree well with the Boltzmann data, which are generally considered to be the more accurate representation of a rarified flow. Although not explicitly stated previously, the momentum exchange model must conserve momentum - meaning that, while, momentum is exchanged between materials, the net momentum of all the materials must be the same before and after the momentum exchange model is applied.

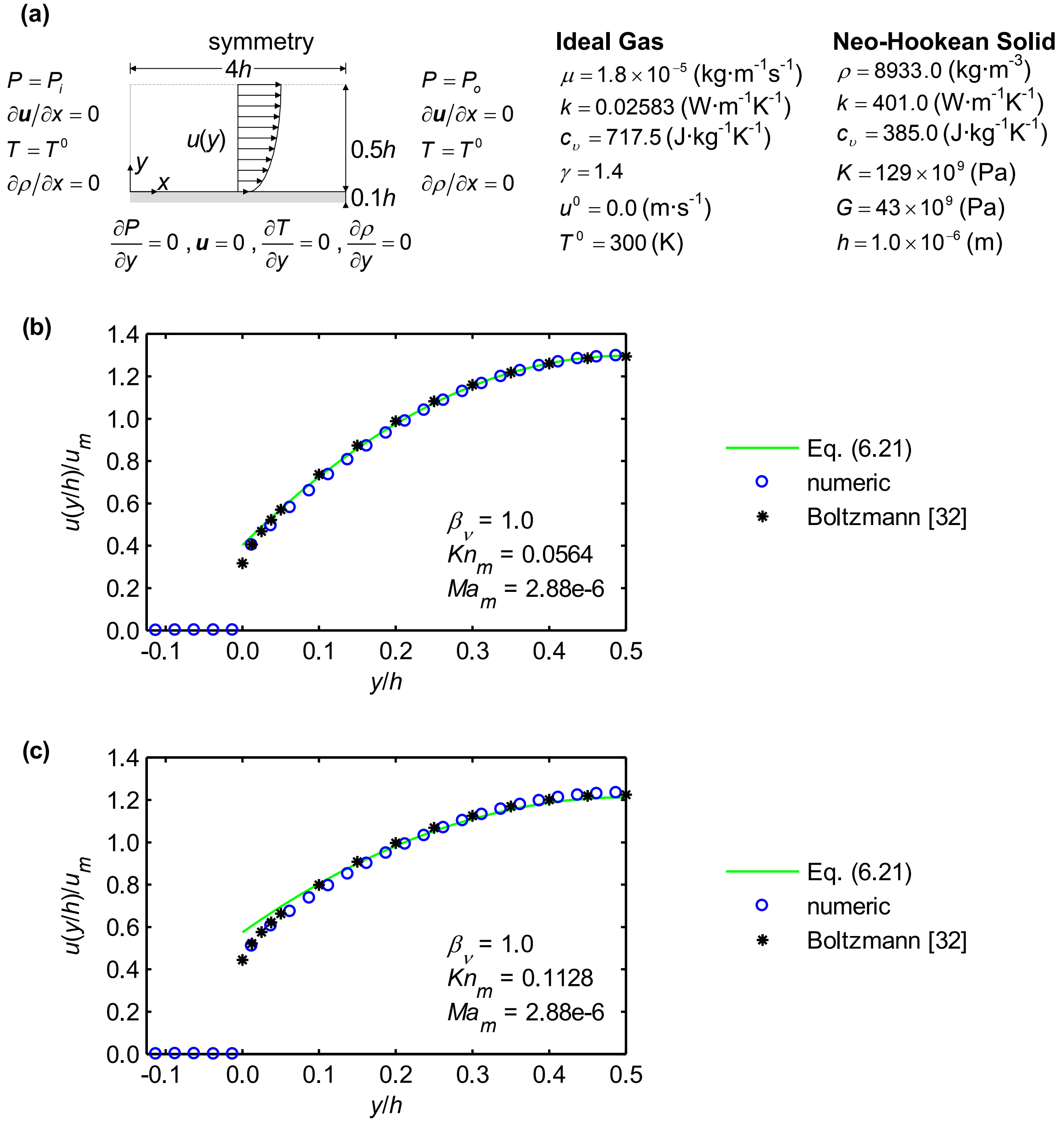

Fig. 6.2. Steady state (t = 0.05μs) pressure driven flow between parallel plates: (a) problem specification, (b) velocity profile, Kn_m = 0.0564, (c) velocity profile, Kn_m = 0.1128.

Table 6.1. Grid resolution, order-of-accuracy, and conservation of momentum exchange for steady state ($t = 0.05\mu s$) pressure driven flow between parallel plates.

Kn_m	Δy (=Δx)	$u(y/h)/u_m$	p	timesteps	RMS (exchange error/total)	
		L_2 error			x-momentum	y-momentum
0.0000	$h/10$	0.387		7,077	6.90×10^{-13}	2.81×10^{-5}
	$h/20$	0.217		28,305	5.60×10^{-14}	4.50×10^{-7}
	$h/40$	0.134	1.017	113,220	6.01×10^{-15}	1.69×10^{-7}
0.0564	$h/10$	0.154		7,077	4.86×10^{-12}	1.15×10^{-10}
	$h/20$	0.088		28,305	1.09×10^{-13}	1.81×10^{-9}
	$h/40$	0.054	0.955	113,220	5.13×10^{-15}	1.15×10^{-10}
0.1128	$h/10$	0.093		14,153	7.23×10^{-12}	7.61×10^{-11}
	$h/20$	0.052		56,611	4.16×10^{-14}	1.29×10^{-10}
	$h/40$	0.032	1.000	226,443	2.20×10^{-15}	8.64×10^{-11}

The root-mean-square (*RMS*) *x*- and *y*- momentum exchange error reported in Table 6.1 is the *RMS*, for all timesteps, of the ratio of the net momentum exchange error to the net momentum. The data in Fig. 6.2 and Table 6.1 indicate that the modified slip flow momentum exchange model accurately represents slip velocity boundary conditions compared to first-order boundary conditions, converges with the same order-of-accuracy as the original algorithm, and conserves the exchanged momentum.

6.3.2. Thermal conduction between parallel plates

The steady state thermal conduction of a stationary, constant property, rarified ideal gas between two parallel plates of different temperatures, as specified in Fig. 6.3(a), is modeled with the MPM-ICE algorithm to verify the accuracy and implementation of the slip flow thermal energy exchange modifications. The analytic temperature profile used to verify the numerical data, Eq. (6.22), is derived by integrating the energy equation, $\partial^2 T/\partial y^2 = 0$, twice and applying temperature jump boundary conditions at each wall, $T\big|_{y=0} = T_w - \Delta T + \beta_t \lambda (\partial T/\partial y)_{y=0}$ and $T\big|_{y=h} = T_w + \Delta T - \beta_t \lambda (\partial T/\partial y)_{y=h}$.

$$\frac{T(y/h)-T_w}{\Delta T}=\frac{-1+2(y/h)}{1+4\beta_t Kn} \tag{6.22}$$

Equation (6.22) is compared to the steady state ($t = 0.05\mu s$) numerical data in Fig. 6.3(b) for the parameters specified.

Grid convergence, order-of-accuracy, and conservation of energy exchange data for this configuration, as well as the total number of timesteps required to reach $t = 0.05\mu s$, are reported in Table 6.2. Once again, the data in Table 6.2 for continuum flow, $Kn = 0$, are produced using the original algorithm, while the data reported for $Kn_m = 0.0564$ and 0.1128 are obtained utilizing the slip flow energy exchange model.

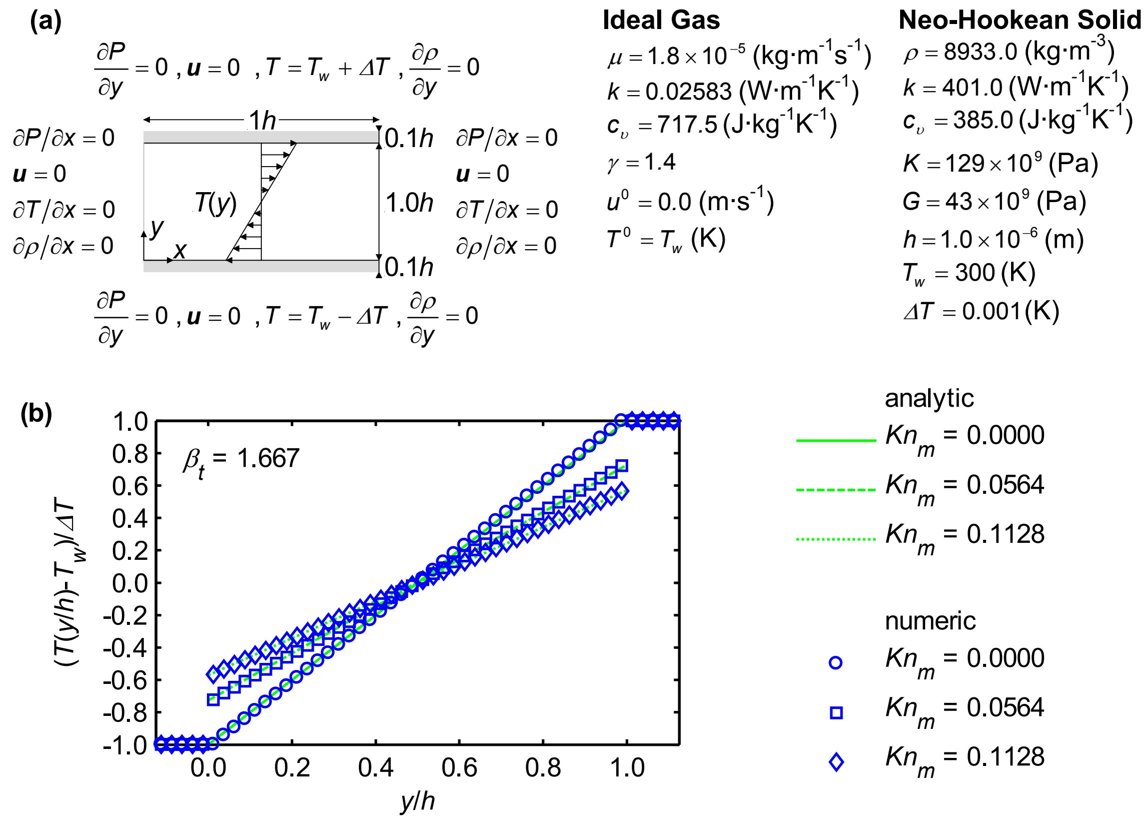

Fig. 6.3. Steady state ($t = 0.05\mu s$) thermal conduction between parallel plates: (a) problem specification, (b) temperature profiles, $Kn_m = 0.0000$, $Kn_m = 0.0564$, $Kn_m = 0.1128$.

Table 6.2. Grid resolution, order-of-accuracy, and conservation of energy exchange for steady state (t = 0.05μs) thermal conduction between parallel plates.

Kn	Δy (=Δx)	$(T(y/h)-T_w)/\Delta T$ L_2 error	p	timesteps	RMS (exchange error/total) thermal energy
0.0000	h/10	0.176		9,435	4.63x10^{-13}
	h/20	0.111		37,740	1.54x10^{-12}
	h/40	0.074	0.794	150,960	4.57x10^{-12}
0.0564	h/10	0.097		14,153	5.61x10^{-13}
	h/20	0.060		56,610	1.56x10^{-12}
	h/40	0.040	0.813	226,440	2.63x10^{-12}
0.1128	h/10	0.063		14,153	5.74x10^{-13}
	h/20	0.038		56,610	0.53x10^{-12}
	h/40	0.025	0.833	226,440	3.22x10^{-12}

The L_2 norm error in Table 6.2 refers to the difference between the normalized numerical and analytical temperature profiles. The order-of-accuracy, computed with the L_2 norm errors, indicate that both the original and modified algorithm converge with increasing grid resolution with an order-of-accuracy of approximately 0.81. To ensure that the modified energy exchange model conserves energy, the *RMS*, for all timesteps, of the ratio of the net energy exchange error to the net energy is reported in Table 6.2. The data in Fig. 6.3 and Table 6.2 indicate that the modified slip flow energy exchange model accurately represents temperature jump when compared to first-order temperature jump boundary conditions, converges with the same order-of-accuracy as the original algorithm, and conserves the exchanged energy.

6.3.3. Low Reynolds number, infinite cylinder C_D and Nu

To verify that the MPM-ICE algorithm, with the slip flow momentum and energy exchange modifications, accurately represents a rarified gas flow for a more complex geometry than those evaluated in sections *6.3.1* and *6.3.2,* flow around an infinite circular cylinder is evaluated. The flow behavior, drag coefficient, C_D, and Nusselt number, *Nu*, for flow around an infinite cylinder are well known for continuum conditions. At very low Reynolds numbers, $Re \approx 0 - 5$, viscous forces dominate and the flow is attached, steady, and symmetric. As Re increases, $Re \approx 5 - 47$, the boundary layer separates and forms a pair of steady, symmetric, counter-rotating vortices in the cylinder wake. As Re increases further, the vortices grow and are alternately shed from either side of the cylinder, resulting in asymmetries and unsteady flow [33]. C_D and Nu are evaluated at very low Re in this study for several reasons. Most significantly, typical microfluidic system Re are very small, due to the small length scales. Additionally, the symmetry present at low Re may be utilized to reduce the computational problem size. Also, without flow separation, effects due to rarefaction only should be more evident. And, furthermore, some slip flow C_D and Nu data are available for comparison to numerical results at low Re, while none exists at higher Re. These data include an analytic C_D solution for creeping slip flow around a sphere [34], for which the rarefaction effects are expected to be comparable in magnitude to creeping slip flow around a cylinder; and, experimentally determined Nu for low Re slip flow around a cylinder [35].

The numerical problem specification and flow parameters utilized to model flow around an infinite cylinder are presented in Fig. 6.4 and Table 6.3. The numerical C_D, per unit length, are obtained utilizing the standard definition, $C_D = F_D / (1/2) \rho_\infty u_\infty^2 D$, where $(1/2)F_D$ is first computed via an integral x-momentum analysis around the symmetric cylinder. Similarly, the numerical Nu are calculated with the usual definition, $Nu = \bar{q}_{cyl}^{''} D / k_r (T_s - T_\infty)$, where $\bar{q}_{cyl}^{''} (\pi D/2)$, one-half of the thermal energy exchange rate, per unit length, due to the cylinder, is first obtained via an integral thermal energy analysis around the symmetric cylinder.

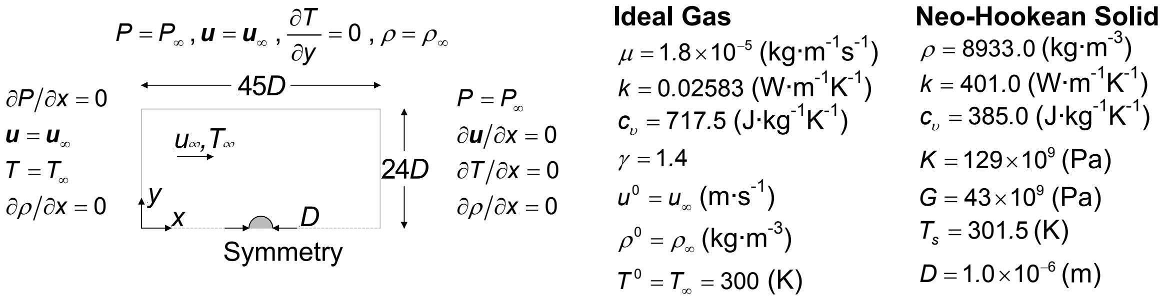

Fig. 6.4. Problem specification for low Reynolds number, infinite cylinder C_D and *Nu*.

Table 6.3. Grid resolution, order-of-accuracy, and comparison to reference values for steady state (t = 60μs) infinite cylinder C_D and *Nu*.

Kn	*Re*	Δx (=Δy)	C_D	*p*	C_D [37] (*Kn* = 0)	C_D [36] (*Kn* = 0)	*Nu*	*p*	*Nu* [39] (*Kn* = 0)	$\overline{Nu} \pm \sigma$ [35]
0.000	0.10	*D*/4	102.83				0.52			
		D/8	95.43				0.50			
		D/16	90.73				0.49			
		extrap.	82.59	0.66	54.42	58.39	0.45	0.44	0.45	-
0.042	0.10	*D*/4	99.39				0.51			
		D/8	93.19				0.49			
		D/16	89.07				0.48			
		extrap.	80.97	0.59	54.42	58.39	0.45	0.55	0.45	-
0.076	0.10	*D*/4	97.74				0.50			
		D/8	92.21				0.48			
		D/16	88.50				0.47			
		extrap.	80.85	0.57	54.42	58.39	0.45	0.58	0.45	-
0.000	1.37	*D*/4	11.45				1.03			
		D/8	10.50				0.99			
		D/16	9.91			-	0.95			
		extrap.	8.90	0.67	9.62		0.75	0.26	0.87	-
0.042	1.77	*D*/4	9.33				1.08			
		D/8	8.63				1.03			
		D/16	8.17			-	0.99			
		extrap.	7.36	0.64	8.41		0.90	0.47	0.94	0.81±0.04
0.076	0.98	*D*/4	13.72				0.88			
		D/8	12.84				0.84			
		D/16	12.25			-	0.82			
		extrap.	11.13	0.60	11.63		0.77	0.57	0.78	0.63±0.07

The resulting, steady state ($t = 60\mu s$) C_D and Nu for each of the three gird resolutions examined, are presented in Table 6.3, and the highest grid resolution C_D and Nu are also plotted and compared to reference values in Figs. 6.5 and 6.6, respectively. The grid resolution order-of-accuracy is approximately 0.6 for C_D and 0.5 for Nu. For each set of Kn and Re conditions Richardson extrapolation [30] is used to approximate the grid independent C_D and Nu, which are then compared to reference values in Table 6.3.

The numerically determined infinite cylinder C_D reported in Table 6.3 and Fig. 6.5, for continuum flow, $Kn = 0.0$, are within approximately 3.0% of the reference value [37] at Re ~1.0 ($\Delta x = \Delta y = D/16$), but are roughly 50% larger than the reference values [36, 37] at $Re = 0.1$. A likely cause of this discrepancy is that the reference C_D values are for an unconfined cylinder, which cannot be exactly numerically simulated. The effect of the computational boundaries, which is reduced by increasing the distance of the boundaries from the cylinder, is to increase C_D, particularly at low Re, by creating a blockage effect with the upper boundary condition, and by not allowing viscous effects to extend infinitely [38]. The effect of rarefaction, quantified by Kn, on the numerically determined cylinder C_D is comparable to, although less than, the analytically predicted effect of Kn on sphere C_D. The sphere C_D is reduced 6.71% for $Kn = 0.042$, and 10.44% for $Kn = 0.076$, for $\beta_v = 1$ and all Re [34]. The numerically determined cylinder C_D is roughly 1-2% less for $Kn = 0.042$, and 2-3% less for $Kn = 0.076$. It is likely that an increase in both the computational domain boundaries, and the grid resolution, will improve the comparison between the numerical and reference C_D data, particularly at $Re = 0.1$, however, this creates an inhibitively large computational problem.

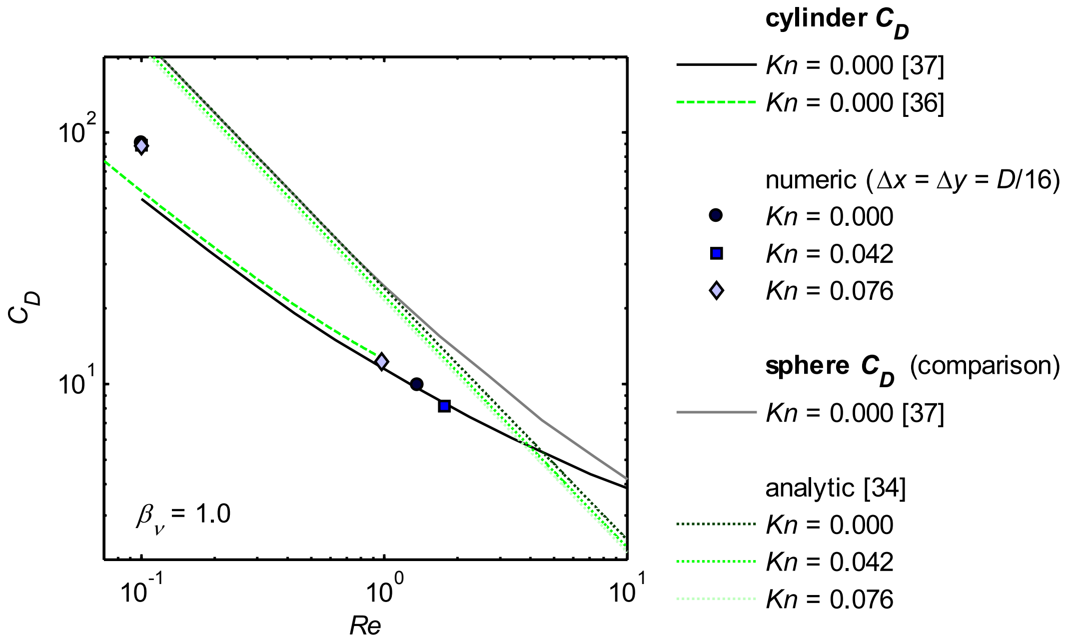

Fig. 6.5. Steady state (t = 60μs) low Reynolds number, infinite cylinder C_D.

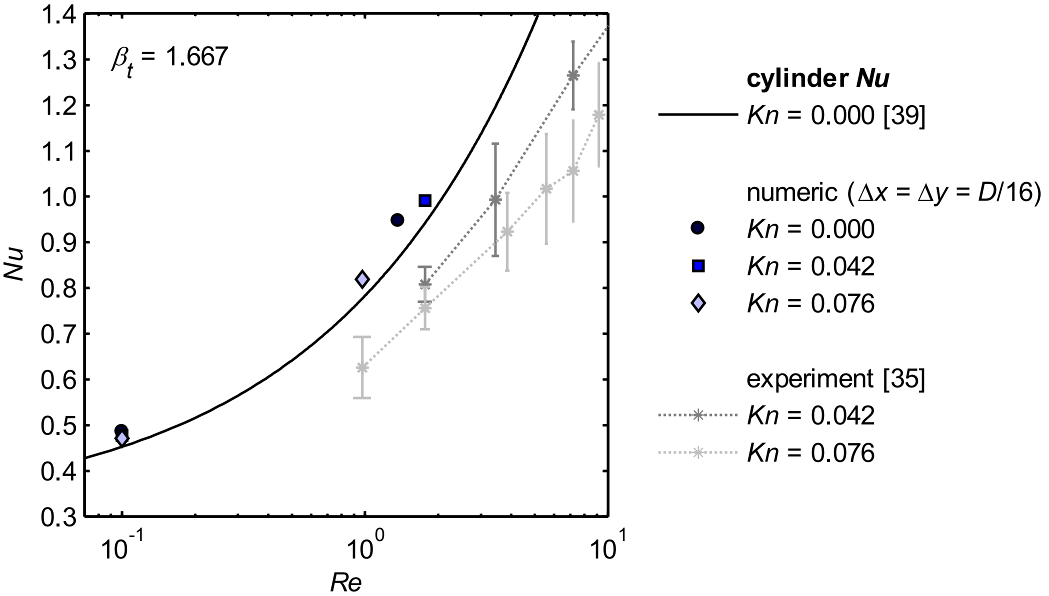

Fig. 6.6. Steady state (t = 60μs) low Reynolds number, infinite cylinder *Nu*.
(Error bars for [35] data are one-standard-deviation.)

Consequently, the agreement between the numerical C_D data and the reference values at *Re* ~1.0, and the agreement in tends due to rarefaction for the cylinder and sphere C_D, are considered sufficient verification of the algorithm's ability to model a rarified flow around an infinite circular cylinder.

The numerically determined infinite cylinder *Nu* data reported in Table 6.3 and Fig. 6.6 are in reasonable agreement with both the continuum correlation [39] and the experimental slip flow data [35]. For the highest grid resolution, the numerical *Nu* for continuum flow, $Kn = 0.0$, are within 8% of the correlation values. There are no comparable experimental data at $Re = 0.1$; however, the numerical data exhibit the same trend as the experimental data, that is, for decreasing *Re* there is a reduced effect of *Kn* on *Nu*. At Re ~ 1.0 the numerical slip flow *Nu* are somewhat higher than the experimental values. The numerical slip flow *Nu* at *Re* ~ 1 are likely higher than the experimental slip flow *Nu*, due to the approximation of the numerical thermal accommodation coefficient, $\sigma_t = 1$. Experimentally measured σ_t are often near unity, but may be any value between zero and one. A value of σ_t less than one will result in an increase in the temperature jump at the surface, which will then produce a decrease in *Nu*. Overall, the agreement between the numerical *Nu* data, the correlation data [39] and the experimental data [35], validate that the MPM-ICE algorithm, with the slip flow momentum and energy exchange modifications, adequately represents the thermal/hydrodynamic flow behavior of a rarified gas around an infinite circular cylinder.

6.3.4. Unsteady slip flow fluid-structure-interaction

The studies presented in sections *6.3.1 - 6.3.3* verify that, for the configurations evaluated, the MPM-ICE algorithm, with the slip flow momentum and energy exchange modifications, is able to model the steady state thermal and hydrodynamic interaction of a rarified gas with a stationary solid. To verify that the algorithm is capable of accurately predicting unsteady fluid-structure-interaction with a rarified flow, the thermal/structural response of a damped-oscillatory three-dimensional cylindrical fin, subject to an impulsively started uniform, rarified flow, as illustrated in Fig. 6.7, is evaluated. This particular configuration is evaluated because there are several similar microscale applications, including, atomic force microscope measurements [5, 7, 16], heat exchangers [4], and bio-sensors and actuators [11, 12, 15]. In this evaluation, the fin initially has zero displacement, $\delta(0,t)=0$, zero velocity, $\partial\delta(0,t)/\partial y=0$, and a uniform temperature equal to the constant fin base temperature, $T(y,0)=T(0,t)=T_b$. The rarified gas initially has a uniform velocity, u_∞, and a uniform temperature, T_∞, that is less than the fin base temperature. As the system is set in motion, the sudden fluid force on the fin results in its displacement and subsequent damped oscillation while it simultaneously transfers heat to the fluid.

To verify the numerical simulation of this system, comparisons to analytic solutions are necessary. The governing equation for beam vibration, the Euler-Bernoulli equation [40], may be solved with the force of the fluid modeled as a Stokes drag force,

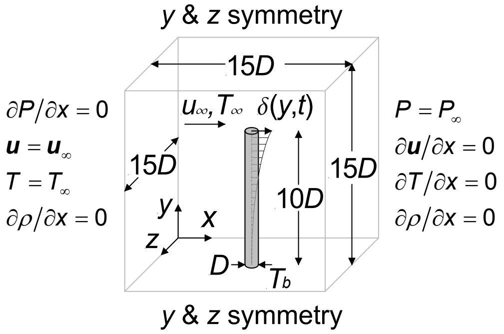

Ideal Gas	**Neo-Hookean Solid**
$\mu=1.8\times10^{-5}$ (kg·m^{-1}s^{-1})	$\rho=1000.0$ (kg·m^{-3})
$k=0.02583$ (W·m^{-1}K^{-1})	$k=0.16$ (W·m^{-1}K^{-1})
$c_\upsilon=717.5$ (J·kg^{-1}K^{-1})	$c_\upsilon=2010.0$ (J·kg^{-1}K^{-1})
$\gamma=1.4$	$K=5.56\times10^6$ or 5.56×10^9 (Pa)
$u^0=u_\infty=0.983$ (m·s^{-1})	$G=1.85\times10^6$ or 1.85×10^9 (Pa)
$\rho^0=\rho_\infty=1.831$ (kg·m^{-3})	$D=1.0\times10^{-6}$ (m)
$T^0=T_\infty=300.0$ (K)	$T^0=T_b=301.5$ (K)
	$u^0=0.0$ (m·s^{-1})

Fig. 6.7. Problem specification for unsteady flow around a flexible cylindrical fin.

$F_D(y,t)/L = C\mu(u_\infty - \partial\delta(y,t)/\partial t)$, which is accurate for very low *Re* flow. The Stokes drag coefficient, *C*, is related to the typical drag coefficient as $C_D = 2C/Re$. The Euler-Bernoulli equation, boundary conditions, initial conditions, and resulting analytic fin displacement solution, $\delta(y,t)$, as obtain by the standard solution methods of separation-of-variables and orthogonality, are summarized in Table 6.4.

The governing energy equation for the fin, boundary conditions (with a convective tip condition), initial conditions, and resulting analytic transient temperature distribution, obtained, again, by the standard solution methods of separation-of-variables and orthogonality, are summarized in Table 6.5. To derive the unsteady, normalized, analytic temperature distribution, $\Theta(y,t)$, it is assumed that the transient fin temperature varies only axially and that the convective heat transfer coefficient, *h*, is uniform and constant. In reality, however, *h* varies both spatially and temporally, and the fin cross sectional temperature will also vary slightly ($Bi_D \sim 0.1$). Consequently, the analytic $\Theta(y,t)$ solution presented in Table 6.5, may only be expected to provide an approximate comparison to the numerical data.

The problem specification and flow parameters utilized to model the transient fin displacement and temperature are given in Fig. 6.7 and Table 6.6. As specified in Table 6.6, both continuum flow, $Kn = 0$, and rarified flow, $Kn = 0.042$, are evaluated for both a flexible, $E = 5\text{x}10^6$ Pa, and a less flexible, $E = 5\text{x}10^9$ Pa, fin. The transient numerical solution is obtained for $t = 0$ - 80μs, with data recorded every 0.5μs. For each timestep recorded, the fin cross sectional average material particle displacement and temperature are obtained at 40 equally spaced axial intervals (for both grid resolutions evaluated).

Table 6.4. Analytic solution for transient fin displacement.

problem specification	boundary conditions	initial conditions
$\frac{\partial^2\delta(y,t)}{\partial t^2}+\frac{C\mu}{\rho_s A_c}\frac{\partial\delta(y,t)}{\partial t}+\frac{EI}{\rho_s A_c}\frac{\partial^4\delta(y,t)}{\partial y^4}=\frac{C\mu u_\infty}{\rho_s A_c}$	$\delta(0,t)=0$ $\partial\delta(0,t)/\partial y=0$ $\partial^2\delta(L,t)/\partial y^2=0$ $\partial^3\delta(L,t)/\partial y^3=0$	$\delta(y,0)=0$ $\partial\delta(y,0)/\partial t=0$

problem solution

$$\delta(y,t)=\delta_p(y)+\sum_{n=1}^{\infty}Y_n(y)A_n\,exp(-\varsigma_n\omega_n t)(cos\,\omega_{d,n}t+(\varsigma_n\omega_n/\omega_{d,n})sin\,\omega_{d,n}t)$$

$$\delta_p(y)=(C\mu u_\infty y^2/24EI)(6L^2-4Ly+y^2)$$

$$Y_n(y)=cosh(\beta_n y)-cos(\beta_n y)-\sigma_n\,sinh(\beta_n y)+\sigma_n\,sin(\beta_n y)$$

$$\sigma_n=sinh(\beta_n L)-sin(\beta_n L)/cosh(\beta_n L)+cos(\beta_n L)$$

$$cosh(\beta_n L)cos(\beta_n L)=-1$$

$$A_n=-\int_0^L\delta_p(y)Y_n(y)dy\Big/\int_0^L Y_n^2(y)dy$$

$$\omega_n=\beta_n^2\sqrt{EI/\rho_s A_c}$$

$$\varsigma_n=(C\mu/2\rho_s A_c\beta_n^2)\sqrt{\rho_s A_c/EI}$$

$$\omega_{d,n}=\omega_n\sqrt{1-\varsigma_n^2}$$

n	$\beta_n L$	$\frac{A_n}{C\mu u_\infty L^4/24EI}$
1	1.8751	$-1.5201\cdot10^{0}$
2	4.6941	$-2.1450\cdot10^{-2}$
3	7.8548	$-1.6041\cdot10^{-3}$
4	10.9955	$-2.9866\cdot10^{-4}$
5	14.1372	$-8.5002\cdot10^{-5}$
6	17.2788	$-3.1166\cdot10^{-5}$
7	20.4204	$-1.3518\cdot10^{-5}$
8	23.5619	$-6.6098\cdot10^{-6}$
9	26.7035	$-3.5351\cdot10^{-6}$

Table 6.5. Analytic solution for transient fin temperature distribution.

problem specification	boundary conditions	initial conditions
$\frac{\partial^2 T(y,t)}{\partial y^2}-m^2(T(y,t)-T_\infty)=\frac{\rho_s c_{\upsilon,s}}{k_s}\frac{\partial T(y,t)}{\partial t}$ $m^2=4h/Dk_s$	$T(0,t)=T_b$ $T(L,t)-T_\infty=-\frac{k}{h}\frac{\partial T(L,t)}{\partial y}\Big\vert_{y=L}$	$T(y,0)=T_b$

problem solution

$$\frac{T(y,t)-T_\infty}{T_b-T_\infty}=\Theta(y,t)=\Theta_p(y)+\sum\nolimits_{n=1}^{\infty}C_n\,exp\left(-\left(\frac{k_s t}{\rho_s c_{\upsilon,s}}\right)(m^2+\Lambda_n^2)sin(\Lambda_n y)\right)$$

$$\Theta_p(y)=\frac{cosh(m(L-y))+(h/mk_s)sinh(m(L-y))}{cosh(mL)+(h/mk_s)sinh(mL)}$$

$$tan(\Lambda_n L)=-(k_s/hL)(\Lambda_n L)$$

$$C_n=\left(\frac{4\Lambda_n}{2\Lambda_n L-sin(2\Lambda_n L)}\right)\left(\frac{1-cos(\Lambda_n L)}{\Lambda_n}-\left(\Lambda_n-\frac{\Lambda_n\,cos(\Lambda_n L)+(h/k_s)sin(\Lambda_n L)}{cosh(mL)+(h/mk_s)sinh(mL)}\right)\Big/(m^2+\Lambda_n^2)\right)$$

Table 6.6. Problem specification, error evaluation, and C_D and *Nu* results for the transient, flexible fin displacement and temperature response.

case	*Kn*	*Re*	*E* (Pa)	Δy (=Δx)	C_D	$\delta(y,t)/D$ L_2 error	*Nu*	$\Theta(y,t)$ L_2 error
1	0.000	0.10	$5.0\text{x}10^6$	*D*/4	183.256	0.823	0.566	2.861
				D/8	162.716	0.741	0.551	2.552
2	0.042	0.10	$5.0\text{x}10^6$	*D*/4	180.206	0.866	0.562	2.780
				D/8	160.406	0.763	0.546	2.478
3	0.000	0.10	$5.0\text{x}10^9$	*D*/4	-	0.035	0.577	2.735
				D/8	-	0.031	0.560	2.501
4	0.042	0.10	$5.0\text{x}10^9$	*D*/4	-	0.034	0.570	2.621
				D/8	-	0.031	0.554	2.417

The normalized numerical fin displacement, $\delta(y,t)/D$, for the higher grid resolution data ($\Delta x = \Delta y = D/8$), is presented and compared to the analytic solution in Fig. 6.8, for several axial locations, $y/L = 0.3, 0.6, 0.9$. All of the parameters required to calculate the analytic fin displacement (Table 6.4), are specified in Fig. 6.7, except the Stokes drag coefficient, $C = ReC_D/2$, which is unknown. Therefore, for *cases 1* and *2*, which are the more flexible fins, the C_D that results in the smallest L_2 norm error between the analytic and numeric $\delta(y,t)/D$ data is utilized to obtain the analytic solution.

The resulting C_D values and L_2 norm errors, for *cases 1* and *2*, are reported in Table 6.6, for each grid resolution evaluated. C*ases 3* and *4*, the more rigid fins, are intended to simulate the fin with zero displacement. Consequently, the L_2 norm error given in Table 6.6 for *cases 3* and *4* is the error of the numerical $\delta(y,t)/D$ data compared to $\delta(y,t)/D = 0$, and because C_D is calculated from the fin deflection, no C_D is reported for *cases 3* and *4.* The expected C_D for an unconfined, infinite cylinder, at $Re = 0.1$ is 58.39 [36]. The numerical finite, cylindrical fin C_D reported in Table 6.6 for *cases 1* and *2*, are much larger than 58.39, due to the effects of flow around the tip of the fin [33], the course grid resolution, and the proximity of the computational boundaries to the fin [38], as discussed

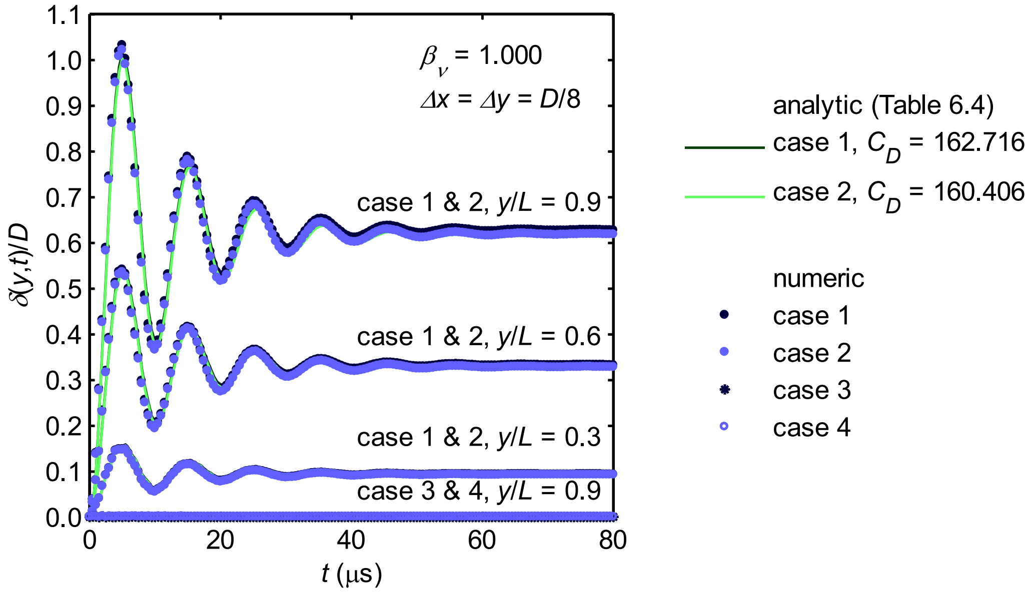

Fig. 6.8. Comparison of analytic and numeric transient fin displacement, $\delta(y,t)/D$.

previously in section *6.3.3*. C_D for $Kn = 0.042$ are approximately 1.5% less than C_D for $Kn = 0.0$. Correspondingly, the amplitude of the fin's displacement is slightly lower for $Kn = 0.042$, compared to $Kn = 0.0$, and the time required to reach steady state is slightly longer for $Kn = 0.042$ compared to $Kn = 0.0$. Although this reduction in C_D due to rarefaction is slight, it is consistent in magnitude with the reduction in C_D due to rarefaction for the infinite cylinder, as presented previously in Fig. 6.5.

All of the parameters required to calculate the analytic transient temperature distribution (Table 6.5), are specified in Fig. 6.7, except the heat transfer coefficient, $h = Nuk_r/D$, which is unknown. Consequently, the Nu that results in the minimum L_2 norm error between the analytic and numeric normalized temperature distribution, $\Theta(y,t)$, is utilized to obtain the analytic solution. The resulting Nu and L_2 norm errors for each case and grid resolution are reported in Table 6.6. The numeric and analytic $\Theta(y,t)$, for *case 2* are compared at several axial locations, $y/L = 0.15, 0.30, 0.90$, in Fig. 6.9, for the

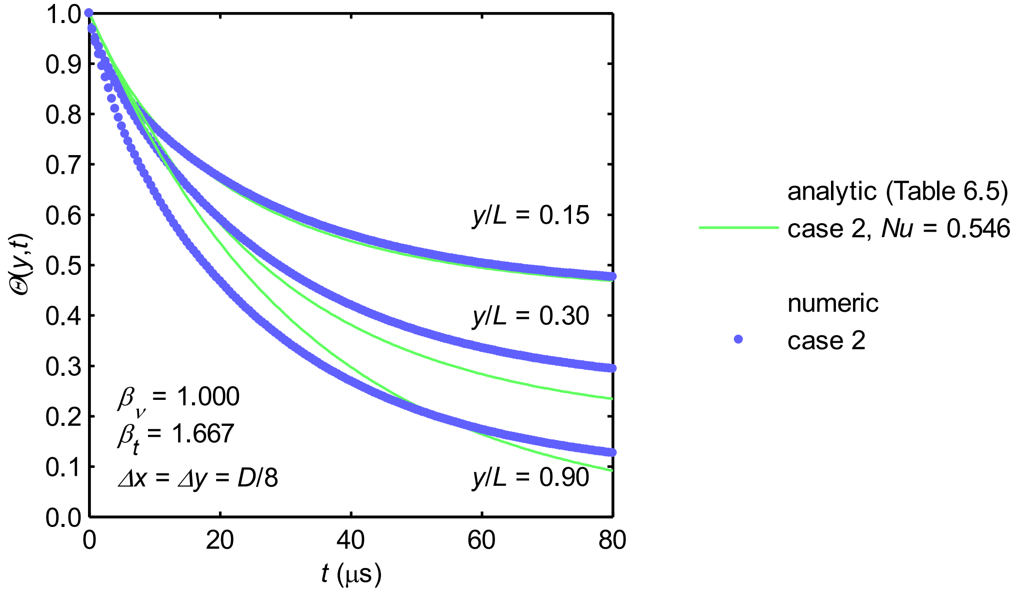

Fig. 6.9. Comparison of analytic and numeric transient fin temperature distribution, $\Theta(y,t)$.

higher grid resolution data ($\Delta x = \Delta y = D/8$). Only data for *case 2* are presented in Fig. 6.9, as the data for each of the other three cases evaluated are very similar. The numeric and analytic $\Theta(y,t)$ in Fig. 6.9 are comparable, but not identical, likely because the numerical h is not uniform or constant.

Differences between the transient thermal data for each of the numerically evaluated cases are more evident by comparing the transient average Nu_m. Using the fin cross sectional average material particle temperature at 40 axial locations, the transient local Nusselt number, $Nu(y,t)$, may be approximated with an energy balance. For each of the four cases evaluated, the transient average Nu_m (the average of the 40 local $Nu(y,t)$) are presented in Fig. 6.10. In all four cases, Nu_m is initially approximately 1.0, and as time progress, Nu decreases and approaches, although within the time period numerically evaluated, does not reach, a thermally steady state value.

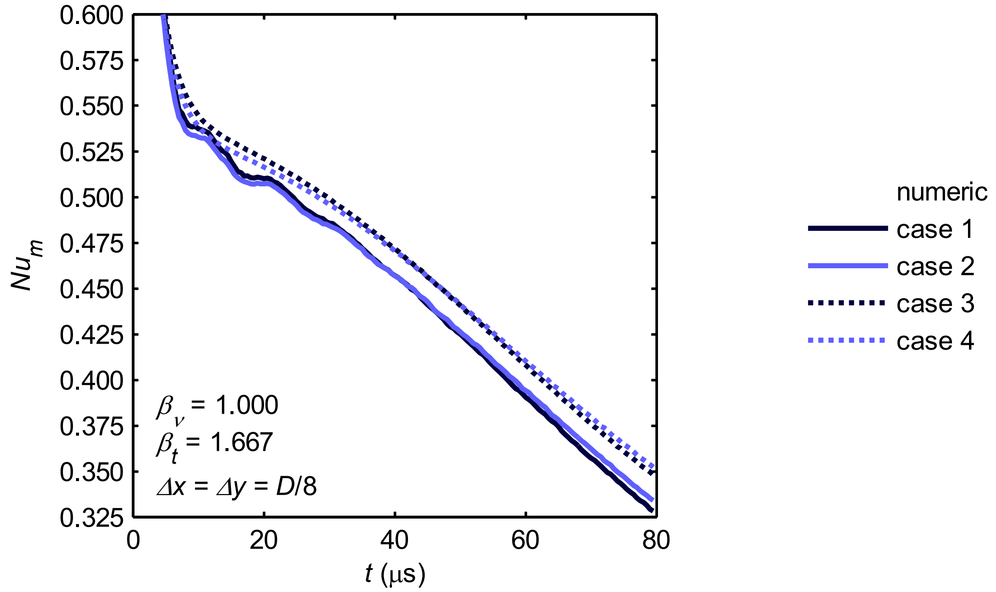

Fig. 6.10. Comparison of axial average transient numeric *Nu*.

For the more flexible fins, *cases 1* and *2*, Nu_m decreases when the fin's motion decreases the relative velocity between the fin and the fluid, and Nu_m increases when the fin's motion increases the relative velocity between the fin and the fluid. Nu_m for the rigid fins, *cases 3* and *4*, are generally larger than Nu_m for the flexible fins, *cases 1* and *2*, likely due to the flexible fin's deformed geometry. The expected steady state *Nu* for an unconfined, infinite cylinder, at $Re = 0.1$ is 0.45 [39]. Although, for each of the four cases evaluated, the numerical *Nu* data are not thermally steady state, the fin is finite in length, and confined by computational boundaries, the minimum L_2 norm error *Nu*, reported in Table 6.6, and the transient axial average *Nu*, present in Fig. 6.10, are still comparable to the reference value of 0.45.

The data presented in Fig. 6.8 – 6.10 indicate that the MPM-ICE algorithm, with the slip flow momentum and energy exchange modifications, is capable of accurately predicting the unsteady fluid-structure-interaction of a damped-oscillatory three-dimensional cylindrical fin, subject to an impulsively started uniform, rarified flow, as compared to the analytically predicted displacement and temperature solutions as well as steady state reference C_D and Nu data.

6.4. Summary

This study modifies the momentum and thermal energy exchange models of an existing, continuum based, multifield, compressible, unsteady, Eulerian-Lagrangian FSI algorithm, such that for a rarified gas in the slip flow regime the equivalent of first-order slip velocity and temperature jump boundary conditions are achieved at fluid-solid surfaces, which may move and deform with time. The momentum and thermal energy exchange models are modified by utilizing slip flow momentum and energy exchange coefficients that are derived as a function of the level of rarefaction from the original first-order slip velocity and temperature jump boundary conditions. The momentum and energy exchange models with the slip flow momentum and energy exchange coefficients are then applied at fluid-solid surfaces such that momentum is exchanged between the rarified gas and the solid material in the fluid-solid surface normal and tangential coordinate directions, rather than arbitrary global coordinates, and slip flow in the surface tangential direction, is realized.

Following the development and implementation of the slip flow momentum and energy exchange modifications, several basic configurations are considered to verify the resulting algorithm's capabilities. The configurations include the velocity profiles of a rarified gas between parallel plates; temperature profiles of a rarified gas between parallel plates; drag coefficients, C_D, and Nusselt numbers, Nu, for low Reynolds number rarified flow around an infinite cylinder; and, the transient, thermal/structural response of a damped-oscillatory three-dimensional finite cylinder subject to an impulsively started uniform, rarified flow. For each configuration, the numerical results are evaluated with grid convergence and order-of-accuracy studies, as well as comparison to analytical, experimental, or previously established reference data. Results of these evaluations indicate that the slip flow momentum and energy exchange models conserve exchanged momentum and energy, respectively, and that with these models, the algorithm is capable of modeling steady and unsteady fluid-structure-interaction with rarefaction effects, with accuracy approximately equivalent to the first-order slip velocity and temperature jump boundary conditions.

There are many microscale systems for which both rarefaction and fluid-structure-interaction effects are significant. Based on the modifications and verifications presented in this study it is expected that the MPM-ICE algorithm, with the slip flow momentum and energy exchange modifications, has the unique ability to accurately model and evaluate these systems, where other FSI algorithms can not. Even so, there are potential improvements and additional verifications of the algorithm that would be beneficial. If experimental, or DSMC data for a microsystem with both FSI and rarefaction effects becomes available, the numerical algorithm should be further validated/verified by comparison to these data. Also, the verifications present in this study are fairly basic, and consequently the slip flow momentum and energy exchange modifications have not yet been verified in conjunction with many of the algorithm's more advanced capabilities, such as, adaptive-mesh-refinement, implicit pressure calculation, variable fluid properties, viscous dissipation, and an increased number of materials. Additionally, refinement of the slip flow momentum and energy exchange models could potentially include a more accurate numerical approximation for the fluid-surface area in each surface cell (used to calculate the slip flow momentum and energy exchange coefficients), and possibly the inclusion of creep flow and/or higher order slip boundary conditions at the fluid solid surface.

6.5. Nomenclature

A	cell fluid-solid surface area
A_c	fin cross sectional area
Bi_D	Biot number, hD/k_s
C	Stokes drag coefficient, $C_D\, Re/2$
c	speed of sound
C_D	drag coefficient, $2F_D/\left(\rho_\infty u_\infty^2 DL\right)$
cfl	Courant–Friedrichs–Lewy number
c_p	specific heat at constant pressure
c_v	specific heat at constant volume
D	diameter or characteristic length
e	internal energy per unit mass
E	Young's modulus of elasticity, $9GK/\left(G+3K\right)$
$\boldsymbol{f}$	force per unit volume
F_D	drag force
Fo	Fourier number, $\alpha t/D^2$
G	shear modulus of elasticity
H_{rs}	thermal energy exchange coefficient

H_{rs}^{slip}	slip flow thermal energy exchange coefficient
h	heat transfer coefficient
h	channel height
I	moment of inertia
K	bulk modulus of elasticity
K_{rs}	momentum exchange coefficient
K_{rs}^{slip}	slip flow momentum exchange coefficient
k	thermal conductivity
Kn	Knudsen number, λ/D
Kn_m	Knudsen number based on mean ρ_m, P_m, T_m
L	fin length
L_2	norm, $\lVert x \rVert_2 = \sqrt{\sum_{i=1}^{n} x_i^2}$
Ma	Mach number, $Re\,Kn\sqrt{2/(\pi\gamma)}$
N	number of materials
Nu	Nusselt number, hD/k_r
P	pressure
p	order-of-accuracy
Pr	Prandtl number, $c_p\mu/k$
Q	rotation matrix
q	thermal energy exchange rate per unit volume
q''	heat flux
R	gas constant

Re	Reynolds number, $\rho_\infty u_\infty D/\mu$
RMS	root-mean-square, $x_{rms} = \sqrt{(1/n)\sum_{i=1}^{n} x_i^2}$
T	temperature
t	time
T_b	fin base temperature
$\boldsymbol{u}$	velocity vector
V	cell volume
$\boldsymbol{x}, \boldsymbol{y}, \boldsymbol{z}$	Cartesian coordinate directions
$\boldsymbol{x}', \boldsymbol{y}', \boldsymbol{z}'$	surface coordinate directions

6.5.1. Greek symbols

α	thermal diffusivity, $k/\rho c_p$
β_t	first-order temperature jump coefficient
β_v	first-order velocity slip coefficient
γ	ratio of specific heats, c_υ/c_p
δ	fin deflection
θ	volume fraction
Θ	nondimensional temperature, $(T - T_\infty)/(T_b - T_\infty)$
λ	mean free path, $\mu/\rho\sqrt{2RT/\pi}$
μ	dynamic viscosity
ν	kinematic viscosity, μ/ρ
ρ	density
$\boldsymbol{\sigma}$	stress

σ	standard deviation
σ_t	thermal accommodation coefficient
σ_v	momentum accommodation coefficient
$\boldsymbol{\tau}$	shear stress
υ	specific volume
φ	rotation angle about z-axis
ψ	rotation angle about y-axis

6.5.2. Subscripts

∞	free stream value
i	inlet value
m	mean value
o	outlet value
r	material index
s	material index
w	wall value
x, y, z	Cartesian coordinate directions

6.5.3. Superscripts

$-$	before exchange contribution
$+$	after exchange contribution
0	initial value

6.6. References

[1] J.C. Maxwell, On stresses in rarified gases arising from inequalities of temperature, Phil. Trans. R. Soc. Lond. 170 (1879) 231-256.

[2] M. Smoluchowski, Ueber wärmeleitung in verdünnten gasen, Annal. Phys. Chem. 64 (1898) 101-130.

[3] G.M. Whitesides, A.D. Stroock, Flexible methods for microfluidics, Phys. Today 54 (6) (2001) 42-48.

[4] J.S. Go, Design of a microfin array heat sink using flow-induced vibration to enhance the heat transfer in the laminar flow regime, Sensor. Actuator. Phys. 105 (2) (2003) 201-210.

[5] S. Basak, A. Raman, S.V. Garimella, Hydrodynamic loading of microcantilevers vibrating in viscous fluids, J. Appl. Phys. 99 (11) (2006) 114906-1.

[6] Y. Bozhi, L. Qiao, A planar compliance-based self-adaptive microfluid variable resistor, IEEE ASME J. Microelectromech. Syst. 16 (2) (2007) 411-419.

[7] D.G. Cole, R.L. Clark, Fluid-structure interaction in atomic force microscope cantilever dynamics and thermal response, J. Appl. Phys. 101 (3) (2007) 34303-1.

[8] S. Desai, M. Lovell, J. Cordle, Coupled field analysis of a piezoelectric bimorph disc in a direct write process, Compos. B Eng. 38 (7-8) (2007) 824-832.

[9] O. Ducloux, A. Talbi, L. Gimeno, R. Viard, P. Pernod, V. Preobrazhensky, A. Merlen, Self-oscillation mode due to fluid-structure interaction in a micromechanical valve, Appl. Phys. Lett. 91 (3) (2007) 034101.

[10] J. Jeong, C.N. Kim, A numerical simulation on diffuser-nozzle based piezoelectric micropumps with two different numerical models, Int. J. Numer. Meth. Fluid 53 (4) (2007) 561-571.

[11] P. Jungyul, R. Suk-Kyu, K. Jinseok, C. Junghun, B. Jeongeun, P. Sukho, K. Byungkyu, L. Sang Ho, A three-dimensional model of fluid-structural interactions for quantifying the contractile force for cardiomyocytes on hybrid biopolymer microcantilever, J. Biomech. 40 (13) (2007) 2823-2830.

[12] V.V. Khatavkar, P.D. Anderson, J.M.J. den Toonder, H.E.H. Meijer, Active micromixer based on artificial cilia, Phys. Fluid. 19 (8) (2007) 083605.

[13] G. Krishnan, J.W. Daily, J. Nabity, Simulation of an electrostatically driven microinjector, J. Propul. Power 23 (6) (2007) 1321-1326.

[14] K.L. Kudar, P.W. Carpenter, Numerical investigation and feasibility study of a PZT-driven micro-valve pulsed-jet actuator, Flow Turbul. Combust. 78 (3-4) (2007) 223-254.

[15] K.-M. Lim, H. Li, A coupled boundary element/finite difference method for fluid-structure interaction with application to dynamic analysis of outer hair cells, Comput. Struct. 85 (11-14) (2007) 911-922.

[16] V. Ostasevicius, R. Dauksevicius, R. Gaidys, A. Palevicius, Numerical analysis of fluid-structure interaction effects on vibrations of cantilever microstructure, J. Sound Vib. 308 (3-5) (2007) 660-673.

[17] G.-Y. Zhou, S.-T. Tu, Viscoelastic analysis of rectangular passage of microchanneled plates subjected to internal pressure, Int. J. Solid. Struct. 44 (21) (2007) 6791-6804.

[18] A.K. Pandey, R. Pratap, F.S. Chau, Effect of pressure on fluid damping in MEMS torsional resonators with flow ranging from continuum to molecular regime, Exp. Mech. 48 (1) (2008) 91-106.

[19] F. Harlow, A. Amsden, Numerical calculation of almost incompressible flow, J. Comput. Phys. 3 (1968) 80-93.

[20] B.A. Kashiwa, N.T. Padial, R.M. Rauenzahn, W.B. VanderHeyden, A Cell-Centered ICE Method for Multiphase Flow Simulations, Los Alamos National Laboratory Technical Report LA-UR-93-3922, 1993.

[21] J.U. Brackbill, D.B. Kothe, H.M. Ruppel, FLIP: A low-dissipation, particle-in-cell method for fluid flow, Comput. Phys. Comm. 48 (1) (1987) 25-38.

[22] D. Sulsky, Z. Shi-Jian, H.L. Schreyer, Application of a particle-in-cell method to solid mechanics, Comput. Phys. Comm. 87 (1-2) (1995) 236-252.

[23] B.A. Kashiwa, A Multifield Model and Method for Fluid-Structure Interaction Dynamics, Los Alamos National Laboratory Technical Report LA-UR-01-1136, 2001.

[24] J.E. Guilkey, T. Harman, A. Xia, B. Kashiwa, P. McMurtry, An Eulerian-Lagrangian approach for large deformation fluid structure interaction problems, part 1: Algorithm development, in: S.K. Chakrabarti (Ed.), Fluid Structure Interaction II: Proceedings of the Second International Conference on Fluid Structure Interaction, Cadiz, Spain, WIT Press, Boston, 2003, pp. 143-156.

[25] T. Harman, J.E. Guilkey, B. Kashiwa, J. Schmidt, P. McMurtry, An Eulerian-Lagrangian approach for large deformation fluid structure interaction problems, part 2: Multi-physics simulations within a modern computational framework, in: S.K. Chakrabarti (Ed.), Fluid Structure Interaction II: Proceedings of the Second International Conference on Fluid Structure Interaction, Cadiz, Spain, WIT Press, Boston, 2003, pp. 157-166.

[26] J.E. Guilkey, T.B. Harman, B. Banerjee, An Eulerian–Lagrangian approach for simulating explosions of energetic devices, Comput. Struct. 85 (2007) 660-674.

[27] J. van Rij, T. Harman, T. Ameel, The effect of creep flow on two-dimensional isoflux microchannels, Int. J. Thermal Sci. 46 (11) (2007) 1095-1103.

[28] J. van Rij, T. Ameel, T. Harman, The effect of viscous dissipation and rarefaction on rectangular microchannel convective heat transfer, Int. J. Thermal Sci. 48 (2) (2009) 271-281.

[29] J. van Rij, T. Ameel, T. Harman, An evaluation of secondary effects on microchannel frictional and convective heat transfer characteristics, Int. J. Heat Mass Transfer 52 (11-12) (2009) 2792-2801.

[30] J.H. Ferziger, M. Perić, Computational methods for fluid dynamics, second ed., Springer, New York, 1999.

[31] S.G. Parker, J. Guilkey, T. Harman, A component-based parallel infrastructure for the simulation of fluid-structure interaction, Eng. Comput. 22 (3-4) (2006) 277-292.

[32] T. Ohwada, Y. Sone, K. Aoki, Numerical analysis of the Poiseuille and thermal transpiration flows between two parallel plates on the basis of the Boltzmann equation for hard-sphere molecules, Phys. Fluids 1 (12) (1989) 2042-2049.

[33] G.J. Sheard, K. Hourigan, M.C. Thompson, Computations of the drag coefficients for low-Reynolds-number flow past rings, J. Fluid Mech. 526 (2005) 257-275.

[34] R.W. Barber, Y. Sun, X.J. Gu, D.R. Emerson, Isothermal slip flow over curved surfaces, Vacuum, 76 (1) (2004) 73-81.

[35] L.V. Baldwin, Slip-flow heat transfer from cylinders in subsonic airstreams, Lewis Flight Propulsion Laboratory, National Advisory Committee for Aeronautics Technical Note NACA-TN-4369, 1958.

[36] Sir. H. Lamb, Hydrodynamics, University Press, Cambridge, 1932.

[37] H. Schlichting, K. Gersten, Boundary-layer theory, eight ed., Springer, New York, 2000.

[38] J. Chakraborty, N. Verma, R.P. Chhabra, Wall effects in flow past a circular cylinder in a plane channel: a numerical study, Chem. Eng. Process. 43 (12) (2004) 1529-1537.

[39] S.W. Churchill, M. Bernstein, Correlating equation for forced convection from gases and liquid to a circular cylinder in crossflow, J. Heat Tran. 99 (2) (1977) 300-306.

[40] D.J. Inman, Engineering vibration, Prentice Hall, Englewood Cliffs, N.J., 1994.

CHAPTER 7

SUMMARY, CONCLUSIONS, AND RECOMMENDATIONS

The preceding chapters introduce various microscale effects, means of analyses, and results for flow and heat transfer in the slip flow regime. A summary of these results, conclusions, and recommendations for the continuation and advancement of this research are given in the present chapter.

7.1. Summary

There are many current and potential applications for microfluidic systems in electronics, instrumentation, bioengineering, medicine, communications, and advanced energy systems. Microfluidic systems, however, often exhibit noncontinuum flow behaviors, scaling effects, and manufacturing effects that cannot be predicted with the extrapolation of macroscale models to the microscale. As a result, microscale flow characteristics are often not well understood, reliable microfluidic design data are limited, and the parameters and computational methods used to model microfluidic systems are not well established. In response to these deficiencies, the research herein has contributed to the advancement of the numerical modeling capabilities and methodologies for microfluidic systems and numerically obtained design data for several common microfluidic configurations and effects.

MPM-ICE, a continuum based, three-dimensional, unsteady, compressible fluid-structure-interaction (FSI) algorithm, introduced in Chapter 2, was utilized to complete the studies presented in Chapters 2 - 6. To accurately model microfluidic systems, several modifications to this algorithm were implemented, including slip velocity, temperature jump, and creep flow boundary conditions, and viscous dissipation terms. Slip velocity and temperature jump boundary conditions were applied utilizing two separate approaches, the first for single fluid internal flow problems, and the second for FSI problems.

For single fluid internal flow problems (Chapters 3 - 5), various slip velocity and temperature jump boundary condition models [1-4] were applied at the fluid computational boundaries. Utilizing this approach, the frictional losses and convective heat transfer rates, presented in terms of the Poiseuille and Nusselt Number, Po and Nu, respectively, of rarified, steady state, laminar, constant wall temperature (T) and constant wall heat flux ($H2$) rectangular microchannel flows were investigated. The numerical results for Po, Nu_{H2}, and Nu_T are given in terms of the aspect ratio (AR), degree of rarefaction ($\beta_{v1}Kn$), the gas-wall interaction parameter (β), slip boundary condition model (β_{v2}, β_{t2}), creep flow (u_c/u_m), viscous dissipation (Br_{H2} or Br_T), axial conduction (Pe), and thermally/hydrodynamically developing flow (x/PeD_h). As a means of verifying the numerical Po, Nu_{H2}, and Nu_T results, analytic solutions for Po, Nu_{H2}, and Nu_T, Eqs. (3.13), (4.10), and (4.12), respectively, were derived for nearly incompressible, steady state, and thermally/hydrodynamically fully developed parallel plate flow and include effects of first- and second-order boundary conditions, creep flow and viscous dissipation with pressure and shear work.

For fluid-structure-interaction problems (Chapter 6) the momentum and thermal energy exchange models of the MPM-ICE FSI algorithm were modified, such that for a rarified gas in the slip flow regime the equivalent of first-order slip velocity and temperature jump boundary conditions were achieved at the fluid-solid surfaces, which may move and deform with time. The momentum and thermal energy exchange models were modified utilizing slip flow momentum and energy exchange coefficients, which were derived from the original first-order slip velocity and temperature jump boundary conditions as functions of the level of rarefaction. The momentum and energy exchange models, with the slip flow momentum and energy exchange coefficients, were then applied at fluid-solid surfaces such that momentum is exchanged between the rarified gas and the solid material in the fluid-solid surface normal and tangential coordinate directions, rather than arbitrary global coordinate directions, and slip flow in the surface tangential direction is realized. Following the development and implementation of the slip flow momentum and energy exchange modifications, several basic configurations were evaluated and compared to analytical, experimental, or previously established reference data. The configurations include velocity profiles of a rarified gas between parallel plates; temperature profiles of a rarified gas between parallel plates; drag coefficients, C_D, and Nusselt numbers, Nu, for low Reynolds number, rarified flow around an infinite cylinder; and, the transient, thermal/structural response of a damped-oscillatory three-dimensional finite cylinder subject to an impulsively started uniform, rarified flow. To verify the numerical results of the transient FSI study, analytic solutions for the finite, flexible cylinder displacement, $\delta(y,t)$, Table 6.4, and temperature distribution, $\Theta(y,t)$, Table 6.5, were derived.

7.2. Conclusions

General conclusions from the first set of studies, the evaluation of rarified, single fluid, rectangular microchannel Po, Nu_{H2} and Nu_T, are as follows.

- Based on the verifications and data presented in Chapters 2-5, ICE, with the single fluid microscale modifications discussed, was capable of accurately assessing the effects of rarefaction with first- or second-order slip boundary condition models, creep flow, viscous dissipation, and axial conduction.
- The data presented in Chapters 3-5 indicate that many of the microscale effects previously considered negligible, with respect to the resulting microchannel Po, Nu_{H2}, and Nu_T, such as, second-order slip boundary conditions, creep flow, viscous dissipation with pressure and shear work, axial conduction, and thermally/hydrodynamically developing flow, are in fact significant within the slip flow regime. Depending on the flow parameters (x/PeD_h, $\beta_{v1}Kn$, β, Pe, AR, Br, etc.), these effects may change the resulting Po, Nu_{H2}, and Nu_T as much as an order of magnitude.
- The assumption of thermally and hydrodynamically fully developed flow is generally well founded for low Pe, and microchannel lengths that are considerably larger that the hydraulic diameter, as shown in Chapters 3-4.
- Po decreases with $\beta_{v1}Kn$ for all AR investigated. For example, using first-order slip boundary conditions, Po for $AR = \infty$ and $\beta = 1.667$ decreases by 59% from $\beta_{v1}Kn = 0.00$ to $\beta_{v1}Kn = 0.12$.
- Nu_T and Nu_{H2} may either increase or decrease with $\beta_{v1}Kn$, depending on β. However, for $\beta = 1.667$, the β value typically assumed for air, Nu_T and Nu_{H2} decrease with $\beta_{v1}Kn$ for all AR investigated. For instance, with first-order slip boundary conditions, $\beta = 1.667$, and

$AR = \infty$, Nu_{H2} and Nu_T decrease by 59% and 58% from $\beta_{v1}Kn = 0.00$ to $\beta_{v1}Kn = 0.12$, respectively.

- Effects of second-order boundary conditions increase as rarefaction increases, with the two models studied [3, 4] having opposite effects on Po, Nu_{H2}, and Nu_T, when compared to first-order boundary conditions [1, 2]. For $AR = \infty$, $\beta_{v1}Kn = 0.12$, and $\beta = 1.667$ the second-order Deissler boundary conditions [3] predict a 24% decrease in Po and a 28% decrease in Nu_{H2}, compared to the first-order boundary conditions, while the Karniadakis and Beskok boundary conditions [4] predict a 17% increase in Po and a 8% increase in Nu_{H2}, compared to the first-order boundary conditions.
- The Po, Nu_{H2}, and Nu_T data obtained with the second-order boundary conditions models of [3] and [4], are expected to be useful as additional experimental and theoretical results become available such that the accuracy of the data may be assessed. Currently, however, there are many proposed second-order models and methodologies and none are widely accepted or validated. Consequently, until a particular second-order model or methodology is extensively substantiated, theoretically and experimentally, further production of data with a specific second-order model will not be particularly beneficial.
- In the slip flow regime, creep flow results in a decrease in Po and an increase in Nu_{H2} for heating, and an increase in Po and a decrease in Nu_{H2} for cooling, by an amount dependant on u_c/u_m, $\beta_{v1}Kn$, β, and AR. For instance, for $AR = 1$, $\beta = 1.667$, and $\beta_{v1}Kn = 0.01$ a $u_c/u_m = \pm 0.25$ will produce a 25% decrease in Po and a 14% increase in Nu_{H2} for heating, and a 25% increase in Po and a 13% decrease in Nu_{H2} for cooling, compared to Po and Nu_{H2} without creep flow effects ($u_c/u_m = 0.0$). The effects of creep flow, for a given u_c/u_m, decrease with increasing $\beta_{v1}Kn$. The significance of including

creep flow in the numerical analysis of *Po* and *Nu* depends on the magnitude of the heat flux and the degree of rarefaction.

- Viscous dissipation increases Nu_{H2} for cooling, and decreases Nu_{H2} for heating as a function of Br_{H2}, $\beta_{v1}Kn$, β, and *AR*. For example, with $AR = \infty$ and $\beta_v Kn = 0.00$ a $Br_{H2} = \pm 0.05$ will produce a 47% increase in Nu_{H2} for cooling, and a 24% decrease in Nu_{H2} for heating, The effects of viscous dissipation, for a given Br_{H2}, decrease with increasing $\beta_{v1}Kn$.
- The combined effects of viscous dissipation, flow work, and shear work within the slip flow regime cause Nu_T to increase, from zero for continuum flow, with increasing $\beta_{v1}Kn$ by an amount dependent on *AR* and β but not on the magnitude of Br_T or *Pe*.
- As discussed in Chapters 4-5, viscous dissipation in rarified flows should not be considered without the related effects of pressure work and shear work, since the contribution of these effects considerably alters the predicted Nu_T.
- Axial conduction effects are significant for flow with low *Pe*, and may increase Nu_T by up to 15%, for the *AR* studied, compared to Nu_T without axial conduction effects. Effects of axial conduction increase with decreasing *Pe*, and decrease with increasing $\beta_{v1}Kn$.
- For these evaluations, the ICE algorithm was run implicitly, such that the required computation time and accumulation of numerical error were reduced. Consequently, the use of ICE for these computational studies was very advantageous.
- One disadvantage of using ICE was that, the computational domain utilized by the algorithm was limited to rectangular geometries, and as a result, the variety of microscale systems that could be examined utilizing ICE only, was somewhat limited.

Several general conclusions based on the second set of studies, the evaluation of FSI in the slip flow regime, are as follows.

- With the modified slip flow momentum and energy exchange models, the MPM-ICE FSI algorithm is capable of modeling both steady and unsteady FSI with rarefaction effects, with accuracy approximately equivalent to the first-order slip velocity and temperature jump boundary conditions.
- The MPM-ICE algorithm, with the slip flow momentum and energy exchange modifications, is uniquely capable of evaluating FSI in the slip flow regime, where other FSI algorithms cannot. Because there are many microscale systems for which both rarefaction and FSI effects are important, and these systems may be impossible to isolate and study experimentally, and too complex to study analytically, this numerical capability presents significant possibilities for microsystem design and evaluation.
- MPM-ICE is explicit with time, and consequently requires considerable computational resources, which may be a deterrent to the use of the MPM-ICE algorithm for further microsystem evaluations. With this said, however, it should be noted that the verifications completed for this research were of a preliminary nature, and not optimized in any way. It is likely that optimization of the physical system (*Re*, *Pr*, E/ρ, etc.), optimization of the computational parameters (CPUs, patches, *cfl*, etc.), and, most significantly, use of the algorithm's more advance features, such as adaptive-mesh-refinement and implicit pressure calculation will considerably reduce the required computational resources.

7.3. Recommendations

Based on the data and advancement of microscale modeling capabilities obtained with the present research, as well as the current lack, or nonexistence, of design data for many microfluidic systems, several studies may logically continue and advance those presented in this work.

- ICE is a compressible flow algorithm, however, for the purpose of verification, the majority of the frictional and convective heat transfer data reported in these studies are for nearly incompressible flow. There are, however, many microfluidic systems for which the assumption of incompressible flow is not applicable, and therefore the combined effects of rarefaction and compressibility on microchannel *Po* and *Nu* should be evaluated.
- For the current research, many of the microscale effects, such as creep flow, axial conduction, and viscous dissipation, are considered individually with rarefaction effects, and the secondary effect of temperature dependent fluid properties is not considered. In an actual microsystem, however, each of these effects will act collectively and may interact to amplify or decrease one another, and consequently these possible interactions should be investigated.
- Microfluidic systems, just as their macroscale counterparts, are often comprised of channels that have bends, branches, expansions, contractions, etc. However, currently no systematic studies are available that report data and/or correlations for pressure loss coefficients through any microgeometry as a function of all of the relevant nondimensional parameters (*Kn*, *Re*, geometry ratios, etc.). Numerical prediction of these

data may be used to improve the function of many microfluidic systems, and due to current experimental and analytical limitations, such data may otherwise be unattainable.

- When experimental measurements for local microchannel velocities, pressures, and temperatures become available, the numerical and analytical results and methods utilized in the present research should be validated by comparison to these data. The usefulness and applicability of second-order boundary conditions models, in particular, should be assessed.
- The research presented in Chapter 6 indicates that the MPM-ICE algorithm with the slip flow momentum and thermal energy exchange modifications, accurately predicts the combined effects of fluid-structure-interaction and rarefaction within the slip flow regime. However, these models may potentially be improved with more precise fluid-surface identification and approximation of the fluid-surface area, and possibly the incorporation of creep flow at the fluid-solid surface.
- The slip flow momentum and energy exchange models and their implementation in the MPM-ICE algorithm should be further verified. These models have not yet been verified in conjunction with many of the algorithm's more advanced capabilities, such as, adaptive-mesh-refinement, implicit pressure calculation, variable fluid properties, viscous dissipation, chemical reaction, and an increased number of materials. Verification and subsequent utilization of these combined capabilities will significantly increase the applicability of the code for the many microscale FSI systems, such as micro valves, pumps, actuators, particulate flows, porous flows, two-phase flows, micro-air-vehicles, combustion, and heat exchangers.

- Currently, experimental measurements of local velocities, pressures, and temperatures within microsystems are generally unattainable. Consequently, there are many experimental microchannel friction and heat transfer rate studies that are based on measurements of the overall mass flow rate, pressure drop, and temperature difference. Within these studies, there are, however, many contradictory results, and without local measurements it is difficult to definitively attribute discrepancies to any one particular effect. Using the MPM-ICE algorithm (with viscous dissipation, variable fluid properties, axial and wall conduction, developing and unsteady flow, and microchannel wall deformations) to 'fill-in' data that are not obtainable experimentally, may considerably advance the general understanding of microfluidic behavior and the significance of the various physical effects on the overall flow characteristics.
- A principle application of microfluidics is to cool high heat flux electrical components. Although air-cooling is often advantageous for reasons of simplicity and economics, the heat removal requirements of many current electrical components are beyond the limits of conventional air-cooling technology. Consequently, the studies presented in Chapter 6 should be advanced, and a microscale array of flexible heat exchanger fins should be numerically designed and optimized, with the intent of increasing the effectiveness of air-cooling for high heat flux applications. With the implementation of this scheme, it is expected that flow induced vibrations of the flexible fins will increase the hydrodynamic mixing, and as a result increase the convective heat transfer rate beyond that of typical microscale laminar flow. The numerical investigation of this particular application, will first require verification/validation of the ability of the MPM-ICE algorithm to predict the vortex shedding frequency of flow around an object,

such as an infinite circular cylinder, as a function of *Re*. Utilizing the MPM-ICE algorithm, with the slip flow modifications presented in the current research, to evaluate the combined effects of rarefaction and FSI for this application will provide valuable data concerning the effectiveness of such a system with respect to the resulting increases in heat transfer and pressure losses, which would be difficult to obtain otherwise, i.e., analytically, experimentally, or by a commercial FSI code.

7.4. Nomenclature

AR	aspect ratio
Br	Brinkman number, $Br_{H2} = \mu u_m^2 / \left(q''_w D_h\right)$, $Br_T = \mu u_m^2 / \left(k\left(T_i - T_w\right)\right)$
C_D	drag coefficient, $2F_D / \left(\rho_\infty u_\infty^2 D_h L\right)$
cfl	Courant–Friedrichs–Lewy number
c_p	specific heat at constant pressure
c_v	specific heat at constant volume
D_h	hydraulic diameter or characteristic length
E	Young's modulus of elasticity
F	friction factor, $8\tau_{w,m} / \left(\rho u_m^2\right)$
F_D	drag force
H	heat transfer coefficient
K	thermal conductivity
Kn	Knudsen number, λ / D_h
L	length
Nu	Nusselt number, hD_h / k

Pe	Peclet number, $Pr\,Re$
Po	Poiseuille number, $f\,Re$
Pr	Prandtl number, $c_p\mu/k$
q''	heat flux
R	gas constant
Re	Reynolds number, $\rho u D_h/\mu$
T	temperature
T_b	fin base temperature
t	time
u	velocity in the x-direction
x, y, z	Cartesian coordinate directions

7.4.1. Greek symbols

β	gas-wall interaction parameter, β_{t1}/β_{v1}
β_{t1}	first-order temperature jump coefficient, $((2-\sigma_t)/\sigma_t)(2\gamma/(1+\gamma))(1/Pr)$
β_{t2}	second-order temperature jump coefficient
β_{v1}	first-order velocity slip coefficient, $(2-\sigma_v)/\sigma_v$
$\beta_{v1}Kn$	rarefaction parameter
β_{v2}	second-order velocity slip coefficient
γ	ratio of specific heats, c_υ/c_p
δ	fin deflection
Θ	nondimensional temperature, $(T-T_\infty)/(T_b-T_\infty)$
λ	mean free path, $\mu/\rho\sqrt{2RT/\pi}$

μ	viscosity
ρ	density
σ_t	thermal accommodation coefficient
σ_v	momentum accommodation coefficient
τ	shear stress

7.4.2. Subscripts

∞	free stream value
c	creep value
$H2$	constant wall heat flux boundary condition
i	inlet value
m	mean value
T	constant wall temperature boundary condition
w	wall value

7.5. References

[1] J.C. Maxwell, On stresses in rarified gases arising from inequalities of temperature, Phil. Trans. R. Soc. Lond. 170 (1879) 231-256.

[2] M. Smoluchowski, Ueber wärmeleitung in verdünnten gasen, Annal. Phys. Chem. 64 (1898) 101-130.

[3] R.G. Deissler, An analysis of second-order slip flow and temperature-jump boundary conditions for rarefied gases, Int. J. Heat Mass Transfer 7 (1964) 681-694.

[4] G.E. Karniadakis, A. Beskok, Micro Flows: Fundamentals and Simulation, Springer-Verlag, New York, 2002.